

DEVELOPMENT, TESTING AND APPLICATION OF LAMINAR MULTIELECTRODES AND BIOCOMPATIBLE COATINGS FOR INTRACORTICAL APPLICATIONS

Ph.D. dissertation

László Bálint Grand

Scientific advisors:

Prof. György Karmos, M.D., Ph.D.

István Ulbert, M.Sc., M.D., Ph.D.



Interdisciplinary Technical Sciences Doctoral School
Faculty of Information Technology
Pázmány Péter Catholic University

Budapest 2010

To my loving parents, family and friends.

DEVELOPMENT, TESTING AND APPLICATION OF LAMINAR MULTIELECTRODES AND BIOCOMPATIBLE COATINGS FOR INTRACORTICAL APPLICATIONS

by László Bálint Grand

Abstract

Simultaneous observation of the activity of a large number of cells might be the key factor for a better understanding of neuronal systems [1]. Modus operandi of different neuronal networks, communication between various neuronal populations and functional connectivity between different brain areas can be uncovered by using simultaneous multisite recording techniques [2-5]. Within the frame of my dissertation, I present the design process, manufacturing and testing of a novel multichannel extracellular silicon microprobe for research applications. Since the utility of an implanted neural interface depends crucially on its biocompatibility and long term viability I addressed this question by investigating the short and long-term effects of various coatings on foreign body reactions emerging around implanted silicon microprobes. Multielectrodes that can be implanted into the central nervous system for long-term are essential tools to study physiological processes at the population level and to elucidate complex brain mechanisms. To prove the advantages of using multichannel cutting edge neural interfaces in basic research I lead the reader by the hand through a case study in which I reveal how I investigated the bioelectric signals of acoustic information processing recorded from the cat auditory cortical layers in different states of the natural sleep-wake cycle and during anesthesia by using a chronically implantable multielectrode array.

The research projects presented in my dissertation unite an engineer's innovations with a neurobiologist's investigations. I have a strong belief that these two different directions not only complete each other but are mutually beneficial to facilitate the successful research on both scientific fields.

TABLE OF CONTENTS

Chapter One

Introduction	21
1. Preface	21

Chapter Two

A novel multisite silicon probe for high quality laminar neural recordings.....	23
1. Introduction	23
2. Design.....	25
2.1. Probe design	25
2.2. Fabrication process	27
2.3. Contact formation	30
2.4. Probe shaping	32
2.5. Packaging	34
3. Results	36
3.1. Impedance measurement	36
3.2. Neural recordings	39
4. Discussion and Conclusion	45

Chapter Three

Short and long term biocompatibility of silicon probes with various coatings	48
1. Introduction	48
2. Methods	50
2.1. Probe implantation and explantation	50
2.2. Coating procedure	52
2.3. Histology	52
2.4. Transmission Electron Microscopy (TEM).....	53
2.5. Scanning Electron Microscopy (SEM).....	53
2.6. Cell counting	53
2.7. Blood vessel analysis.....	54
2.8. Statistics.....	54
3. Results	54
3.1. Neuronal and glial cell distribution in the rat neocortex	54
3.2. Effect of bleeding during probe insertion.....	55
3.3. Effects of different coatings on neuron survival	58
3.4. Glial reaction around the probes.....	64
3.5. Transmission electron microscopy of the probe tracks	66
3.6. Neuronal cell bodies - tissue preservation.....	67
3.7. Synapses	69
3.8. Scanning electron microscopy of the explanted probes	70
4. Discussion	72
4.1. Probe implantation.....	73
4.2. Effects of bleeding.....	73
4.3. Effects of coatings on neuron numbers	74
4.4. Effects of coatings on glial response	75
4.5. Surface of the probes	76
4.6. Conclusions	76

*Chapter Four***Information processing in the cat auditory cortex during the natural sleep-wake cycle and anesthesia..... 78**

1. Introduction.....	78
1.1. The auditory thalamocortical system.....	79
1.2. The auditory thalamocortical loop.....	80
1.3. The auditory thalamocortical pathway.....	81
1.4. The auditory corticofugal pathway.....	82
1.5. The auditory corticocortical pathways.....	82
1.6. The cat auditory cortex (AC).....	83
1.7. The Auditory Evoked Potential (AEP).....	84
1.8. Sleep states and related oscillations.....	86
1.9. The slow oscillation (SO).....	88
2. Methods.....	92
2.1. Surgical procedure and electrodes.....	92
2.2. Acoustic stimulation.....	95
2.3. Data acquisition.....	95
2.4. Data analysis.....	96
2.5. Current Source Density (CSD) analysis.....	96
2.6. Time-frequency analysis.....	97
2.7. Up- and down-state detection.....	97
2.8. Peri or Post-Stimulus Time Histograms (PSTH).....	98
2.9. Statistical methods.....	99
3. Results.....	99
3.1. Distinguishing the different states of the natural sleep-wake cycle.....	100
3.2. AEPs in different states of the natural sleep-wake cycle and anesthesia.....	100
3.3. Comparing evoked and spontaneous down-states of SWS.....	105
3.4. Cortical oscillatory dynamics in SWS and anesthesia.....	106
3.5. Double click stimuli evoked responses in the cat AC in SWS and wakefulness.....	108
4. Discussion.....	110

Chapter Five

Summary.....	116
1. Novel scientific results.....	116
2. Application of the results.....	118
The author's publications.....	120
Bibliography.....	122

ACKNOWLEDGMENT

First, I would like to thank Professor György Karmos that he piqued my interest in electrophysiology by giving us interesting and outstanding lectures and choosing me to be his participant for the Scientific Student Conference. During the six years we have been working together, I had the chance to learn from him professionally but more importantly, his humaneness taught me every day.

I would like to thank István Ulbert that he always found time for teaching me even though he had lots of work. He gave me the opportunity not only to join his researches, but also supported my new ideas as well. I am thankful for sponsoring my participation on conferences that allowed me to get acquainted with several novelties.

I am much obliged to Lucia Wittner for the possibility of working together at the Institute of Experimental Medicine of the Hungarian Academy of Sciences and for teaching me immunohistochemical methods. I got to know her as a learned and excellent teacher and a kind person.

I also owe these persons for the help to win the Professional Internship Program of the Hungarian American Enterprise Scholarship Fund (HAESF), thanks to their letters of recommendation, and for giving me the possibility to carry-on after my return. I am also grateful to the HAESF for awarding me with their prestigious scholarship. I thank my colleagues, Balázs Dombóvári and Richárd Csércsa for the good mood and inspiring collaboration during our Ph.D. studies. I could always rely on them no matter what problems we had to solve.

I would like to thank the Faculty of Information Technology of the Pázmány Péter Catholic University and especially professor Tamás Roska for giving me the possibility to achieve my research goals. Both the Faculty of Information Technology and the Laboratory for Electrophysiology opened the door for me to pursue interdisciplinary research.

I thank to Dr. László Acsády, the head of the Thalamus research group of the Institute of Experimental Medicine of the Hungarian Academy of Sciences, for providing me his laboratory for the immunohistochemical studies of my research. I thank to Dr. István Czigler, the director of the Institute of Psychology of the Hungarian Academy of Sciences and to Dr. István Bársony, the director of the Research Institute for Technical

Physics and Materials Science of the Hungarian Academy of Sciences for providing me facilities for the work at the institutes led by them.

The Hungarian multisite silicon probe could not come into existence without the Institute for Technical Physics and Materials Science of the Hungarian Academy of Sciences. Their knowledge, patience and enthusiasm motivated me to work to the best of my ability. My special thanks go to Dr. Gábor Battistig who made it possible to begin the research without external financial resources and to Anita Pongrácz who helped me a lot in organizing the research project. I also thank the other members of the silicon probe developing group, Éva Vázsonyi, Gergely Márton, Dorottya Gubán, Károlyné Payer and István Réti for their ideas and help. I thank to Gergely Márton for the wonderful 3D pictures.

Last but not least, I would like to thank to my parents, my sister and my fiancée, to the whole family and my friends. Without their unconditional love, encouragement and support I would not have succeeded. I am thankful for everything and apologize for all inconveniences I caused them in these years.

LIST OF FIGURES

Figure 2.1. Simplified and non-proportional 3D model of the silicon probe with one site (close to its tip), the corresponding lead and a contact pad. Note that thin film layers deposited on the bulk silicon are magnified to make them visible.

Figure 2.2. (A) Back side mask for the first anisotropic etching. (B) Frontside mask for making holes above the sites and contact pads. (C) Back side mask for the second anisotropic etching. (D) Frontside mask for defining Pt pattern.

Figure 2.3. The plan view of the probe pattern.

Figure 2.4. Schematic representation of the probe fabrication process flow given in a cross-section through an electrode site (not to scale). A, B, C and D indicate the end of the 4 major processing steps with (A) thin film depositions and contact formation on the frontside, (B) defining the probe thickness by the first anisotropic etch, (C) Probe shaping with the combination of an anisotropic and isotropic wet etch from the back side and (D) removal of protecting layers and frame structure.

Figure 2.5. Optical micrograph of a probe shaft with thickness and width of 80 μm and 280 μm , respectively. The square shaped Pt contacts have a side length of 30 μm and are contacted to 4 μm wide leads.

Figure 2.6. The schematic illustration of a chip with the probe and the supporting frame from frontside (a) and backside (b). The four sites and corresponding leads are only the illustrations of the 24 recording sites that can be found on the fabricated probes.

Figure 2.7. Scanning Electron Microscopic (SEM) pictures of the silicon probe. Upper part of the figure shows the probe tip and 3 out of 24 Pt recording sites. The enlarged yacht bow like tip is seen on the bottom figure. Note the rounded shape and smooth surface of the back side of the probe. The imaging was carried out in a LEO 1540 XB SEM equipped with field emission gun, Gemini lens system and in-lens detector.

Figure 2.8. Light microscopic picture of a wafer with 25 probes in holder frames. Note that wet etching is not always immaculately accomplished resulting in residuals around the probe shaft (third row in the first column from left). Based on visual inspection for defects (short and open circuits, etching and insulator defects) the fabrication yield was about 40%.

Figure 2.9. Packaging of the acute silicon probe. Inset on the right side of the upper picture shows micro grids before bonding.

Figure 2.10. Impedance was measured before the acute experiments at 1 kHz with sine wave current less than 500 nA. The figure shows impedance values of 24 sites of 3 probes. Their average impedance was 1067.36 ± 99.91 k Ω .

Figure 2.11. Result of a soak test of a probe with 2 bad sites (Nr. 2 and Nr. 5). Impedance measurement was carried out at 3 (blue), 6 (yellow), 9 (cyan), 12 (purple) and 24 (orange) hours after the first measurement while the probe was kept in Ringer solution. The initial average impedance increased by 6.21% in 24 hours.

Figure 2.12. Activation resulted in decreased impedance on each site. The average impedance of this probe dropped from 1195.12 ± 113.1 to 659.04 ± 59.47 , which is 55.14% of the initial value. Before activation (green), after activation (purple).

Figure 2.13. LFP recorded from the MC and CPu of rat nr. 1. The 24th channel is allocated for indicating the time of stimuli if it is given. LFP gain: EEG (1k).

Figure 2.14. Outstanding MUA was recorded from the MC and CPu of rat Nr. 1. Unit activities could be isolated from 8 channels.

Figure 2.15. Magnified view of LFPs and MUAs belong to channels with good quality SUAs. The vertical scale bar represents 2 values, one belongs to MUA (+32 μ V) and the other to LFP (+300 μ V). Gain: EEG (1 k), MUA (50 k).

Figure 2.16. (A) 10 lowest and 10 highest amplitude spikes that belong to different neurons recorded on site Nr. 6 (A), Nr. 9 (B) and Nr. 19 (C) is depicted. Their averages (blue) and SDs (dotted orange lines) are presented. Auto-correlograms in the right column indicate refractory period of neuron recorded on site Nr. 6 (D), Nr. 9 (E) and Nr. 19 (F).

Figure 2.17. Good quality LFP and MUA characterized the recorded signal. Remarkable unit activity is seen in the signal that was acquired with the site located closest to tip (Nr.1). The vertical scale bar represents 2 values, one belongs to MUA (+32 μ V) and the other to LFP (+300 μ V) respectively. Gain: EEG (1k), MUA (50k).

Figure 2.18. A. 10 smallest and 10 highest amplitude firing activities of the same unit, the average of total 1249 spikes (orange) and their SD (dotted black line) are represented. The recording site was located in the CPu. B. Histogram of the first channel unit shows no activity in the -1.6 ms and 1.6 ms range that means clearly distinguishable SUA was recorded on site Nr. 1. 60 bins with 0.5 ms resolution shows count numbers related to auto-correlogram.

Figure 3.1. Schematic drawing of implanted probe types (see details in [85]. Probes E100P had shanks with a cross section of 100 μ m x 100 μ m at the tip, 5 Pt electrode contacts on each shank, and a thin probe base for platform-based assembly (A). Probes D100C had shanks of 100 μ m x 100 μ m, no electrode contacts on the shafts, and a wider, 300 μ m thick probe base for cable assembly (B). Probes D150C had shanks of 150 μ m x 100 μ m, no electrode contacts, and the wide probe base for cable assembly (C). A scanning electron micrograph shows a D100C probe in the silicon wafer (D). Sizes of the probes are indicated. Tracks of D100C and D150C probes are compared on light micrographs from the neuronal marker NeuN-stained sections (E).

Figure 3.2. Rat neocortex stained with the neuron marker NeuN (A) and the astroglial marker GFAP (B). The layers are indicated by dashed lines.

Figure 3.3. Effects of bleeding during implantation. Signs of serious bleeding during implantation were evident at both 1 week (A, B, arrows) and 12 weeks (C). The tissue was damaged around the probe tracks: a dark unspecific staining masked neuronal (A) and glial (B) immunostaining (DexM coated probe). In some cases, patches with severe neuron loss (asterisk) were observed near damaged tissue (C, Si probe) or next to the probe track without the signs of tissue damage (D, Dex coated probe).

Figure 3.4. Blood vessel distribution in rat neocortex. Photos (A, B) and drawings (C, D) show the cross section area of blood vessels in supragranular (A, C) and infragranular (B, D) layers of the cortex. Both small and large size blood vessels are more abundant in the supragranular layers (E); the average size (F) and the total area covered by the vessels (G) are also larger.

Figure 3.5. Effect of coating on neuronal densities. Light micrographs show similar neuron numbers around tracks made by probes with different coatings (A). The most serious neuron loss was observed at 1 week survival, in the vicinity of the track (<100 μm), neuron numbers ranging from 50% to 76% compared to control (B). The neuronal density increases with distance from the track, and with survival time, reaching 80% to 102% at 8 weeks (C). Different coatings affect neuronal survival at 1 week survival, but effects become less significant at longer intervals. The efficacy of the different coatings Hya<Dex<Si<Hya/DexM<DexM is similar for short or long term survival (D). Neuronal loss observed at short term decreases with survival time (E). Error bars represent mean \pm S.E.M. * $p<0.001$

Figure 3.6. Glial reaction around the probe tracks. In general, only moderate gliosis occurred at short (A, middle) and long (B, middle) term survival. Compared to control, larger and darkly stained reactive astroglial cells were visible around the tracks at 1 week survival (A, middle, right). At longer delays (12 weeks, B) glial cell numbers and shape returned to control levels (B, middle). In some cases, lower and higher glial reaction occurred around different shanks of the same probe (A, B), sometimes related to a serious bleeding (A, right).

Figure 3.7. Light micrographs show good preservation of neurons (A) and a slight gliosis (B) around native silicon probes after 1, 2, 4 and 12 weeks of survival.

Figure 3.8. Transmission electron micrographs of the probe tracks shown in Figure 3.6. at 1 week (A, B) and 12 weeks (C, D) survival. Large caverns (asterisks) and damaged membranes were found next to the tracks at 1 week survival (A, B), whereas the tissue was not damaged at 12 weeks (C, D). In all cases, neuronal cell bodies (N on A, C, D) were found within 100 μm from the border of the probe tracks. Numerous neurons were observed at less than 20 μm from the track.

Figure 3.9. Transmission electron micrographs show the ultrastructure of the neural tissue 1 week after probe implantation. In case of no bleeding (A) signs of tissue damage were observed up to 30 μm from the track (arrows). When bleeding occurred (B) the tissue was damaged in a considerably higher radius (up to 130 μm in this case, arrows).

Figure 3.10. Transmission electron micrographs show synapses found close to the probe tracks at 1 week (A, B) and 12 weeks (C-F) survival. Membranes of the pre- and postsynaptic elements were discontinuous when the tissue was damaged around the probes (A, B), but the synaptic cleft seemed to be preserved (arrows). Numerous synapses were found in the close vicinity of the track, at both with low (C, D) and high (E, F) glial reaction. Squares on C and E are enlarged on D and F, respectively. Asterisk indicates part of the track.

Figure 3.11. Scanning electron micrographs of explanted probes. Low magnification photo shows the tissue residue partly covering the probe surface (A). Usually activated microglia-like, small round cells formed a densely packed layer on the explanted probes (B). Astroglia-like large (C), and small fusiform cells (D) were also observed. In some cases, electrode contacts were free of tissue residue (E), but totally covered contacts were also observed (F).

Figure 4.1. Auditory cortical fields on the temporal cortex of the cat [131]. (A) Lateral view. (B) Lateral view that is unfolded to show the part of the field that are normally hidden within the sulci (orange shading), as well as the high- and low-frequency limits of the tonotopic fields.

Figure 4.2. The thalamocortical loop. The CT cell sends excitatory synapses to TC and nRT cells. The CT cells excite CT and nRT cells. nRT neurons inhibit TC cells. TC: thalamocortical, CT: corticothalamic; nRT: thalamic reticular cell [119].

Figure 4.3. Areas of the cat auditory cortex [164]

Figure 4.4. Shape and latencies of the main components of the auditory evoked potential (AEP) recorded from the median ectosylvian gyrus of an alert cat. The click stimulus was presented at 0 ms.

Figure 4.5. Cortical intracellular correlates of natural SWS, REM and waking states. Parts indicated by arrows are expanded below (arrows). Note cyclic hyperpolarizations in SWS and diminished firing rate during ocular saccade in REM sleep [185].

Figure 4.6. Chronically implantable stainless steel laminar multielectrode with 24 Pt-Ir recording contacts.

Figure 4.7. A 5x5 guide tube matrix for chronic implantation.

Figure 4.8. Up- and down-state detection method based on linear filtering (B) and Hilbert transformation (C) of the recorded field potential (A).

Figure 4.9. LFP and unit responses to click stimuli in wakefulness and SWS. **a**, Continuous LFP traces in the wake state from representative depths of the AC covering superficial - top traces - and deep layers - bottom traces - respectively. **b**, Simultaneously recorded unit activity. Click stimulation is indicated by the trigger line below the unit traces. **c**, LFP traces in SWS. **d**, Unit traces in SWS. Translucent red marker strips indicate the time of AEPs in wake, while blue strips indicate the time evoked down-states. Note the large deep positive wave evoked by click stimulus only in SWS.

Figure 4.10. Click stimuli evoked LFP averages. The data was recorded from layer IV of the AC during SWS (blue), REM (red) and wakefulness (green). Click stimuli was given at 0 ms.

Figure 4.11. Averaged CSD, MUA and spectral responses time locked to click stimuli in wakefulness and SWS. **a**, CSD map of stimulus locked activity in wakefulness. Time: x-axis, stimulus is presented at 0 ms, cortical depth: y-axis. Sinks are depicted in red, sources in blue, arbitrary units. Laminarization is indicated by Roman numerals. **b**, Simultaneously recorded MUA map. Red indicates firing rate increase, blue decrease compared to baseline activity, arbitrary units. **c**, CSD map in SWS. **d**, Simultaneous MUA map in SWS. Note the large source and neuronal firing silence in SWS. **e**, LFP spectrogram (1-200Hz) from representative depths of the cortex in response to click stimuli in wakefulness. Each elongated rectangle represents different channel. Red indicates increased, blue decreased activity in arbitrary units compared to baseline. **f**, LFP spectrogram in response to the click in SWS. Grey rectangle shows the time frame of the down-state.

Figure 4.12. Time-frequency analyses (Morlet wavelet) of evoked activities (3/sec click) in SWS, REM and wakefulness. The timing of each stimulus is indicated with short black lines on time-axis. Intensive power increase is seen in every frequency band after the click stimuli in SWS, especially in the low frequency ranges. Note the long-lasting power decrease in SWS that is absent in REM or waking states. The wavelet maps were calculated using recordings derived from the same contact.

Figure 4.13. CSD and MUA maps of evoked and spontaneous down-states in SWS. **a**, Click evoked down-state (only if a down-state was detected within 15-35 ms interval post stimulus) onset locked CSD map. **b**, Stimulus evoked down-state onset locked MUA map. **c**, Spontaneously occurring down-state onset locked CSD map (the stimulus was switched off). **d**, Spontaneously occurring down-state onset locked MUA map. **e**, Difference CSD map of evoked and spontaneous down-states. Green indicates no significant differences (t-test, Bonferroni corrected to multiple comparison, $p > 0.2$). **f**, Difference MUA map of evoked minus spontaneous down-states. Green indicates no significant differences (t-test, Bonferroni corrected to multiple comparison, $p > 0.2$). During the approximate time of the down-state (grey box) there are no significant differences between evoked and spontaneous activity.

Figure 4.14. MUA and CSD maps related to averages of down-states evoked with click stimuli in SWS and spontaneously occurring in KX anesthesia. Cortical layers are represented with roman numbers. Sinks on CSD maps are depicted with red, sources with blue, arbitrary unit. Red on MUA maps indicates increased, blue decreased activity in arbitrary units compared to baseline. Laminarization is indicated by Roman numerals.

Figure 4.15. CSD and MUA averages related to down-states evoked with click stimuli in SWS and spontaneously occurring in KX anesthesia.

Figure 4.16. CSD and MUA responses to double click stimuli in wakefulness and SWS. **a**, CSD map in response to a short delay (40 ms) double click stimuli in wakefulness. **b**, CSD map in response to the short delay stimuli in SWS. **c**, CSD map in response to a long delay (80 ms) double click stimuli in wakefulness. **d**, CSD map in response to the long delay stimuli in SWS. Note that the CSD response to the second click on **b**, is highly suppressed and even the 80 ms delayed second stimulus on **d** can evoke a clear down-state. **e**, MUA (arbitrary units) from layer III of another cat time locked to the stimulus in wakefulness. Single click response in green, short (20 ms) delay double click response in red, long (100 ms) delay response in blue. **f**, MUA responses in SWS. Note the large difference at short delays (red trace) between wakefulness and SWS. Note also that the evoked down-state is present even in response to the 100 ms delayed second click in SWS.

LIST OF TABLES

Table 2.I. Main steps of the probe fabrication process flow.

Table 2.II. Comparison of different properties of various probes

Table 3.I. Implanted probe types and survival times.

Table 3.II. Percentage of neurons at certain distances from the probe track, compared to control, at short term (1 week) survivals. Data are presented in mean±S.E.M.

Table 3.III. Neuron numbers at certain distances from the probe track at 1 and 8 weeks survival. Data are given in mean±S.E.M.

Table 3.IV. Statistical significances for the different locations around the different probes, at 1 week survival. * $p < 0.05$, ns= not significant

Table 3.V. Percentage of neurons at certain distances from the probe track, compared to control, at long term survivals (DexM>Hya/DexM>Si>Dex>Hya). Data are presented in mean±S.E.M.

Table 3.VI. Percentage of neurons at certain distances from the probe track, compared to control, at different time points, around E100P uncoated Si probes. Data are presented in mean±S.E.M.

LIST OF ABBREVIATIONS

μ -WEMS: Micro-wire electrical discharge machining

A: Anisotropy

AAF: Anterior auditory field

ABC: Avidin-biotinylated horseradish peroxidase complex

AC: Auditory cortex

Ach: Acetylcholine

AEP: Auditory evoked potential

AES: Anterior ectosylvian field

AI: Primary auditory cortex

AII: Secondary auditory cortex

Al: Aluminum

AP: Anteroposterior

BHF: Buffered HF

BP filter: Band-pass filter

CH₃COOH: Acetic acid

CSD: Current source density

CT: Corticothalamic cells

CVD: Chemical vapor deposition

D100C: Dummy probe, 100 μ m, Cable assembly

D150C: Dummy probe, 150 μ m, Cable assembly

DAB: 3,3'-diaminobenzidine tetrahydrochloride

dB: Decibel

Dex: Dextran

DexM: Dexamethasone

DRIE: Deep reactive ion etching

DV: Dorsoventral

DWL: Direct write laser

DZ: Dorsal auditory zone

E100P: Probe with electrodes, 100 μ m, Platform assembly

ED: Posterior ectosylvian gyrus

EEG: Electroencephalograph

EI: Intermediate part of the posterior ectosylvian gyrus

EMG: Electromyography

EOG: Electrooculogram

EPSP: Excitatory postsynaptic potential

ERP: Event related potential

EV: Ventral part of the ectosylvian gyrus

FFT: Fast Fourier transformation

fMRI: Functional magnetic resonance imaging

FP: Field potential

GABA: γ -aminobutyric acid

GFAP: Glial fibrillary acidic protein

H₂O₂: Hydrogen peroxide

H₂SO₄: Sulfuric acid

H₃PO₄: Phosphoric acid

Hc: Hippocampus

HF: Hydrogen-fluoride

HNO₃: Nitric acid

Hya/DexM: Hyaluronic acid and Dexamethasone

Hya: Hyaluronic acid

IC: Inferior colliculus

In: Insular cortex

IPSP: Inhibitory postsynaptic potential

IrO_x: Iridium oxide

K⁺: Potassium

KOH: Potassium hydroxide

KX: Ketamine-xylazine

LFP: Local field potential

LPCVD: Low-pressure chemical vapor deposition

MC: Motor cortex

MCFA: Multiple channel frequency analyzer

ME: Multielectrode

MEMS: Micro-electro-mechanical systems

MGB: Medial geniculate body

ML: Mediolateral

MMN: Mismatch negativity
MUA: Multiple unit activity
N1: Surface negative late component of the AEP
NaOCl: Sodium hypochlorite
NaOH: Sodium hydroxide
NeuN: Neuronal marker
nRT: Thalamic reticular nucleus
OsO₄: Osmium tetroxide
P: Posterior auditory cortex
P1: The first surface positive depth negative component of AEP
P2: The second surface positive component of AEP
PAF: Posterior auditory field
PB: Phosphate buffer
PCB: Printed circuit board
PS: Paradoxical sleep
PSTH: Peri/Post-stimulus time histogram
Pt: Platinum
REM: Rapid eye movement
RF: Receptive field
RIE: Reactive ion etching
S.E.M.: Standard error of the mean
SD: Standard deviation
SEM: Scanning electron microscopy
Si: Silicon
SiN_x, Si_xN_y:: Silicon nitride
SiO₂: Silicon dioxide
SiO_x: Silicon oxide
SO: Slow oscillation
SOI: Silicon-on-insulator
SPL: Sound pressure level
SPW-R: Sharp wave ripple
SUA: Single unit activity
SWS: Slow wave sleep
TB: Tris buffer

TC: Thalamocortical cell

Te: Temporal cortex

TEM: Transmission electron microscopy

Ti: Titanium

TiO_x: Titanium oxide

TMAH: Tetramethylammonium hydroxide

Ve: Ventral auditory area

VP: Ventral posterior auditory area

Chapter One

INTRODUCTION

1. Preface

When I started working in the Comparative Psychophysiology group at the Institute for Psychology of the Hungarian Academy of Sciences (IP-HAS) as an undergraduate student I always felt that air was full with mysticism because electrophysiology is a kind of science which medical aspects are barely understandable for an engineer. It was obvious for me from the very first moment that the first project I joined to and which related to development of various signal processing methods for neural signal analysis is only the entrance ticket to the wonderful and manifold world of electrophysiology. Various cutting edge neural probes implantation and recording techniques and emerging biocompatibility issues thus material science and pharmacology related questions, as well as trying to find the answer to the question how a specific neural loop works with abstract thinking after measuring the local neural activities, were and still are compelling to me.

During the one-year lasting fellowship of the Hungarian American Enterprise Scholarship Fund (HAESF) at the middle of oldest beating heart of silicon based neural interface technology, the Neural Engineering Laboratory of the University of Michigan and the NeuroNexus Technologies Inc., I understood the limits of at that time the cutting-edge neural interfaces and emerging issues of their application. After my returning to Hungary I started to work on a novel extracellular multisite silicon probe at the Research Institute for Technical Physics and Materials Science of the Hungarian Academy of Sciences, with keeping in view the limits of Michigan probes. After reviewing the cutting edge neural interface technologies in the second chapter of my dissertation, I present the fabrication technology, packaging process and *in vivo* characterization of a novel multisite silicon probe. At the end of chapter two, discussion of difficulties and my future plans in connection with probe development are presented.

Emerging short and long-term biocompatibility issues draw the line for long-term applications of neural prosthesis. Within the frame of the NeuroProbes project I had the possibility to investigate what kinds of coating can reduce inflammatory responses around implanted inactive multishank silicon probes on short and long-terms. After a

brief introduction to different pharmacological agents currently used in neural interface technology to suppress immunological response in chapter three, my research methods and results on this project are presented with discussion and conclusion.

Multichannel neural probes are vital tools to advance understanding of cellular and system level functions in the central nervous system. To prove it, in chapter four I present the results of an experiment in which a chronically implantable multisite probe played a key role. Since the electrodes spanned the whole depth of the cortex and neural activities of cortical layers could be recorded from freely moving cats, I revealed how information processing changes in different states of the natural sleep-wake cycle as well as in ketamine-xylazine (KX) anesthesia. These results are put into the context of others' findings in the discussion section.

In chapter five my main findings and novel scientific results are summarized. The author's publication list and bibliography is presented at the end of this dissertation.

Chapter Two

A NOVEL MULTISITE SILICON PROBE FOR HIGH QUALITY LAMINAR NEURAL RECORDINGS

1. Introduction

Different approaches have been reported about various multisite probes or arrays. Stereotrodes [6], tetrodes [7, 8] and micro-wire bundles [9, 10] were used first to record neural signals with many sites in acute and in chronic experiments. These technologies are still in use for ensemble recording. Their limitations, such as imprecise implantation, low recording resolution and low reproducibility are also well known [11]. Another big step towards the high spatial resolution recording was made by the introduction of wire based laminar microelectrode arrays. The micro-wire based thumbtack probe [12, 13] is a good example for that because it contains up to 24 contacts on one polyimide shank and its site spacing is precisely reproducible. A similar laminar array with a stainless steel shank is also known and used in experimental neuroscience [14, 15] as it is presented in chapter three. Another microwire based array approach was published by Nicolelis et al. in 2003 [16]. Their fine wires are placed and fixed close to each other that yield high resolution data in long-term recordings. These measurements however, are limited to a cortical layer only since each wire, which cut end gives a recording contact, has the same length.

In contrast to the previously mentioned recording techniques, the silicon based multisite structures are not only precise and suitable for batch fabrication and have reproducible, small dimensions, but numerous contacts can be placed at different points along each probe. Moreover, they offer the potential of integrated signal processing circuits on them and the applied silicon dioxide and silicon nitride thin films have good biocompatible properties [17].

The first photoengraved brain microelectrode fabrication process based on wet etching was published early by Wise et al. [18]. This technology was further developed in order to fabricate fork-like shapes by using a combination of high temperature boron diffusion and wet etching [19]. However, the slow boron diffusion limits the maximum probe thickness to about 15 μ m that results in a fragile but less invasive probe with maximum

length of around 10 mm. Its modified version with on-chip integrated circuit [20] and 3D array configuration have also been developed [21-23].

Since the 1970s a wide variety of probes have been constructed by using different silicon fabrication methods. Besides the Michigan probes [18-24] the Utah array [25] also became well known. It consists of 10×10 isolated silicon needles with tips exposed for potential recording. Since only a single tip-electrode is available per shaft, laminar recording from the cortex with this array is not feasible. An interesting micro-wire electrical discharge machining (μ -WEMS) based MEMS method for producing arrays has been developed recently by Rakwal et al. [26].

Plasma etching was also applied to define desired probe outlines rather than anisotropic wet etching [27-29]. Double-sided Deep Reactive Ion Etching (DRIE) processes were developed by different groups in order to produce probes with silicon-on-insulator (SOI) technology [30, 31]. A Direct Write Laser (DWL) based method was introduced by Kindlundh et al. [32] to realize fast custom design probe fabrication. The combination of Reactive Ion Etching (RIE) and DRIE methods was applied by the NeuroProbes consortium [33, 34] to form the desired probe thickness and shape. Within the frame of that project, various single shank, four shank [35], drug delivery [36], chemical sensor probes [37] and 3D arrays [38, 39] have been fabricated for acute and chronic use. Alternatives to silicon such as polyimide [11, 40, 41], parylene [42], glass [43] or thin film ceramic [44, 45] as possible probe substrates have also been investigated.

I present a novel wet chemical etching based process [46] that yields a highly reproducible silicon multi-electrode device that was fabricated at the Institute for Technical Physics and Materials Science of the Hungarian Academy of Sciences. This sensor contains 24 platinum recording contacts. The rounded probe with sharp and yacht-bow like tip provides high resolution, good quality recording. The maximum length and thickness of such a probe can be varied in a large scale. The body of the probe can easily be cleaned and reused because of its mechanical properties. The multichannel probe presented here could easily penetrate the dura and pia mater without bending, breaking or causing serious bleeding.

2. Design

2.1. Probe design

Each probe contains a single shaft, which can be inserted into the brain tissue, supported by a more robust connector part. Both the shaft and the connector part were made of the same single crystal silicon wafer, with bulk micromachining. On the surface of the connector part bonding pads have been placed, while on the 7 mm long, 280 μm wide and 80 μm thick shaft 24 square-shaped (30 $\mu\text{m} \times 30 \mu\text{m}$) sites have been located for extracellular potential recording. The center-to-center distances of the neighbouring sites were chosen to be 100 μm , and the distance between the tip and the middle of the first contact window is 660 μm . The length of the tip is basically defined by the fabrication process, since yacht bow like and sharp tip was an elementary requirement from the very first stage of the design. The tip angle is approximately 26 degrees. Each site has been electronically connected to a bonding pad with 4 μm wide and 4 μm spaced wiring. The sites, the wires and the pads have been made of the same, 300 nm thick TiO_x and Pt layers. Figure 2.1. shows a simplified and non-proportional 3D model of the probe with one site, the corresponding lead and a contact pad.

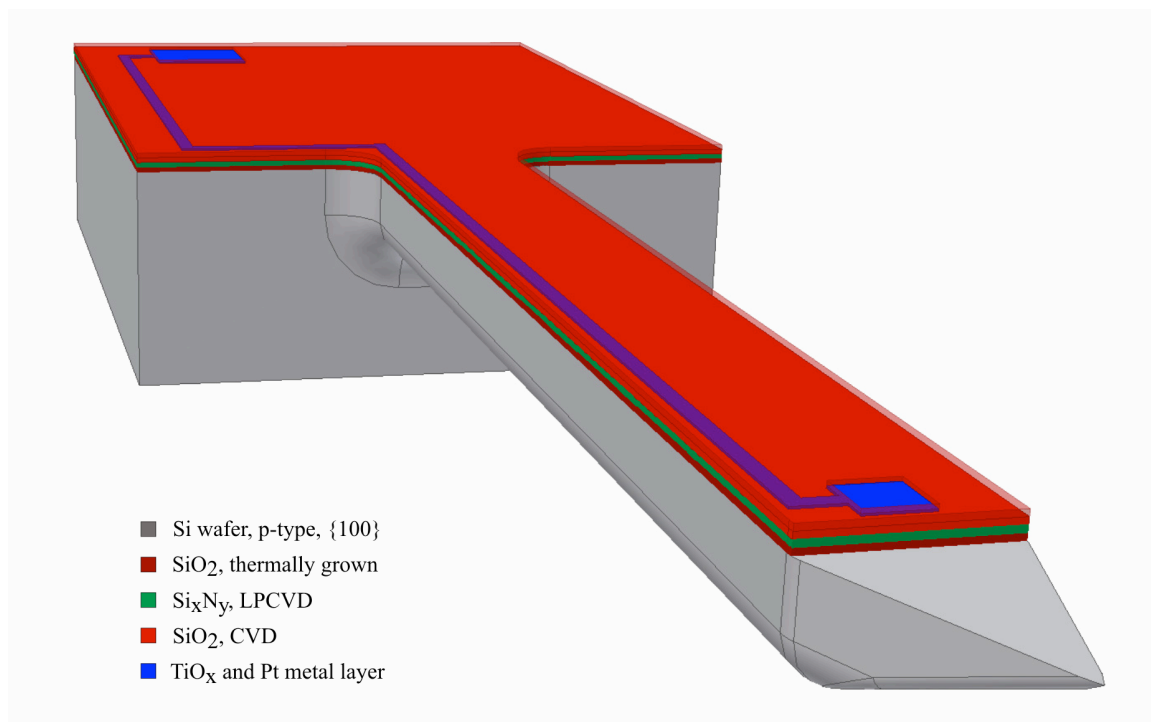


Figure 2.1. Simplified and non-proportional 3D model of the silicon probe with one site (close to its tip), the corresponding lead and a contact pad. Note that thin film layers deposited on the bulk silicon are magnified to make them visible.

A series of masks have been designed on the basis of the calculation considering the size effect of the silicon bulk etching processes. 4 masks (Figure 2.2.) are needed to form the 3 dimensional geometry as well as the electrodes, corresponding leads and contact pads on the microprobes. I designed these 4 masks with the Mask Edit software in 5x magnification compared to the real dimensions of the desired neural microprobes. The master masks corresponding to different photolithographic steps included the magnified version of a chip. The mask pattern was made out of 0.1 μm thin chrome layer on glass. The pattern is then covered with 0.5 μm thin positive photoresist. The pattern is selectively developed by exposing the mask with light at 354 nm wavelength. I had to take into consideration that the maximum size of the diaphragm, which is used to flash the photoresist, is 3000 x 3000 μm in open position. The mask resolution is limited by the precise positioning abilities of the desk underneath the diaphragm. This is 1 μm in x and y dimensions. The masks were manufactured at the MTA MFA.

The masks, which have been used in the fabrication process can be sorted into two categories: back side and frontside masks (Figure 2.2.). The two back side masks define the 3D structure of the probes. They have been designed on the basis of the calculation considering the size effect of the silicon bulk etching processes. The two frontside masks specify the patterns of the platinum and insulator layers.

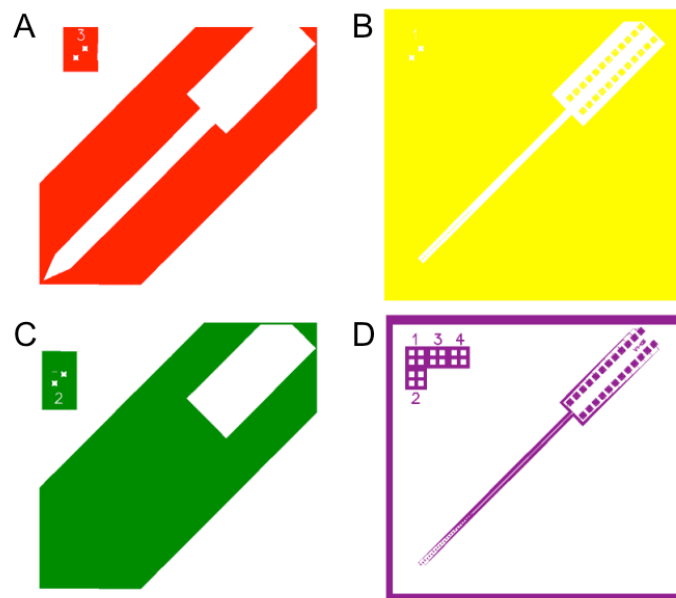


Figure 2.2. (A) Back side mask for the first anisotropic etching. (B) Frontside mask for making holes above the sites and contact pads. (C) Back side mask for the second anisotropic etching. (D) Frontside mask for defining Pt pattern.

Key features in the fabrication process include a sequence of wet etching processes to shape the probes from the back side. CVD silicon dioxide films and low stress LPCVD silicon nitride films are applied for insulating and protecting layers and one metal layer is deposited for the formation of electrodes, output leads and bonding pads. The plan view of the probe pattern is shown on Figure 2.3. A patent application that describes our method in details was submitted [46].

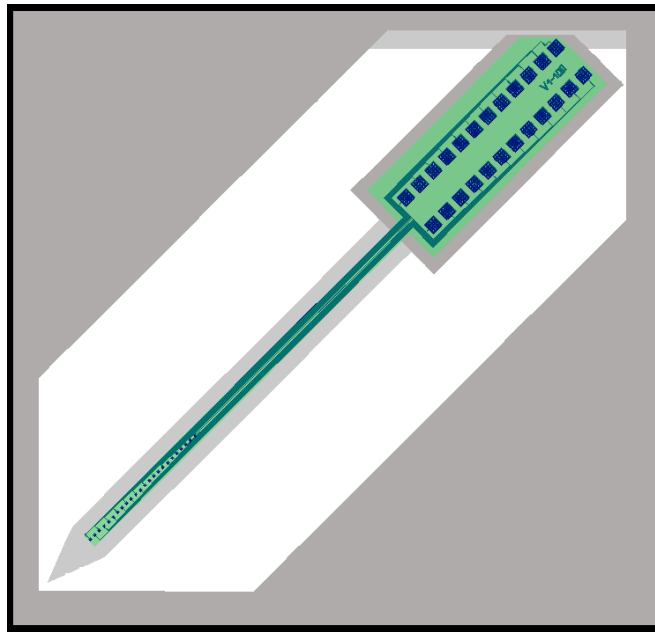


Figure 2.3. The plan view of the probe pattern.

2.2. Fabrication process

Standard $\langle 100 \rangle$ oriented, p-type silicon wafer with a diameter of 3 inches and thickness of 200 μm polished on both sides were used for the probe fabrication (denoted by **1** on Figure 2.4.), that proceeded in 4 steps (Figure 2.4.). In initial thin-film deposition steps the bottom insulating layers (**2,3,4**), the electrodes and output leads (**5**), the passivation layer (**6**) are formed and the contact holes and bonding pads are opened (Figure 2.4.A.). The subsequent 2 steps consisted of different types of wet chemical etching processes for the probe shaping in order to obtain sharp tip with rounded edges (Figure 2.4.B-C.). The final phase of the probe fabrication process consisted of the removal of the protecting and masking layers and packaging of the probe (Figure 2.4.D.). Residual stress in the passivation layers (i.e. bending) or other mechanical stress had no visible signs on the probe. The process flow is presented on Figure 2.4. and its summary is shown on Table 2.I.

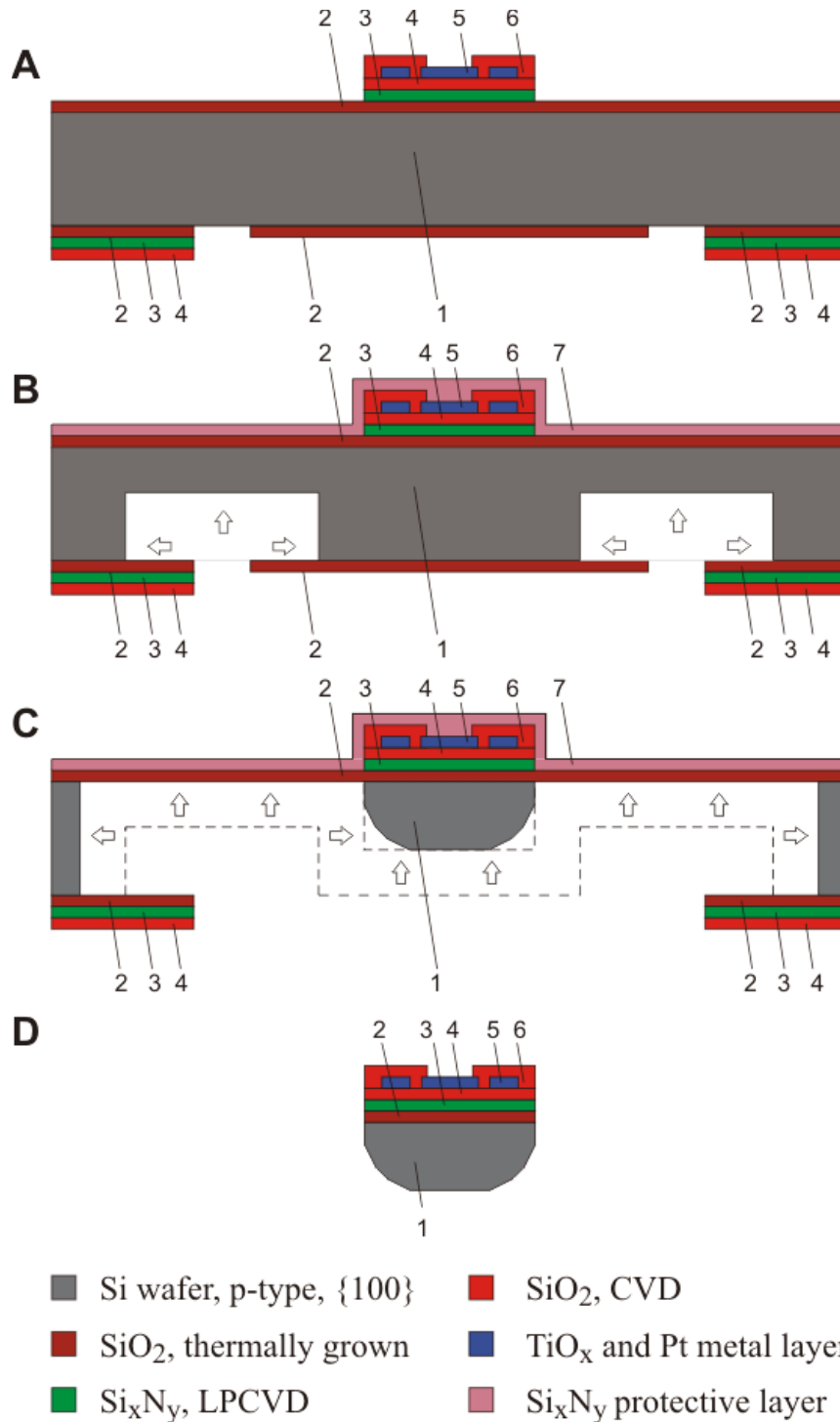


















Figure 2.4. Schematic representation of the probe fabrication process flow given in a cross-section through an electrode site (not to scale). A, B, C and D indicate the end of the 4 major processing steps with (A) thin film depositions and contact formation on the frontside, (B) defining the probe thickness by the first anisotropic etch, (C) Probe shaping with the combination of an anisotropic and isotropic wet etch from the back side and (D) removal of protecting layers and frame structure.

TABLE 2.I. MAIN STEPS OF THE PROBE FABRICATION PROCESS FLOW.

	<i>Step Nr.</i>	<i>Process step</i>	<i>Front</i>	<i>Back</i>
	1. Oxidation	Wet oxidation, 900 nm	+	+
	3. Nitride deposition	LPCVD SiN _x 500 nm	+	+
	4. Oxide deposition	CVD SiO _x 500 nm	+	+
	5. Al deposition	500 nm Al deposition	+	
	6. Photolithography I.	<i>Pt wires</i>	+	
	7. Al etching	Wet Al etcher	+	
	8. TiO _x /Pt sputtering	15nm TiO _x and 300 nm Pt	+	
	9. Lift off	Acetone and wet Al etcher	+	
	10. Oxide deposition	CVD SiO _x 1000 nm	+	
	11. Photolithography II.	<i>Contacts</i>	+	
	12. Oxide etch	Oxide wet etch in BHF	+	
	13. Photolithography III.	<i>Frame</i>		+
	14. Oxide etch	Oxide wet etch in BHF		+
	15. Nitride etch	Wet etch in H ₃ PO ₄	+	+
	16. Photolithography IV.	<i>Frame & probe</i>		+
	17. Oxide etch	Oxide wet etch in BHF		+
	18. Nitride deposition	LPCVD SiN _x 500 nm	+	

	19. Anisotropic wet etch	Alkaline solution		+
	20. Oxide etch	Oxide wet etch in BHF		+
	21. Anisotropic wet etch	Maskless etch in alkaline solution		+
	22. Isotropic wet etch	Rounding etch		+
	23. Oxide etch	Oxide wet etch in BHF		+
	24. Nitride etch	Wet etch in H ₃ PO ₄	+	
	25. Flip out the probe			

 Si wafer, p-type, {100}	 SiO ₂ , CVD
 SiO ₂ , thermally grown	 TiO _x and Pt metal layer
 SiN _x , LPCVD	

2.3. Contact formation

Silicon wafers were oxidized in steam atmosphere at 1150°C for 140 minutes in order to grow 900 nm thick SiO₂ layers on both sides of the substrate. The thick oxide layer was removed from the frontside in buffered HF (BHF) while the back side was protected by photoresist (Microposit 1818). After that 100 nm thick SiO₂ layer was grown using dry thermal oxidation at 1100°C for 40 minutes. Thermally grown SiO₂ layers are denoted by **2** on Figure 2.4.A-D. 500 nm thick low stress (190 MPa) silicon nitride film was deposited by LPCVD at 830°C followed by a 200 nm thick CVD oxide deposition at 430°C, denoted by **3** and **4**, respectively.

The metal layer (denoted by **5**) was then deposited and patterned by lift-off process. In the photolithographic steps the axis of the mask pattern of the probe were aligned along the <100> and <010> crystallographic directions on both sides of the wafer. The lift-off structure composed of 1.8 μm thick photoresist (Microposit 1818) layer over patterned Al thin film of 500 nm. Al etching was performed in a 4 component etching solution, consisted of H₂O, CH₃COOH, H₂SO₄, H₃PO₄, and HNO₃ in a ratio of 70:20:30:32:20, respectively. The metal layer consisted of a 15 nm thick adhesion layer of TiO_x and Pt. TiO_x was formed by reactive sputtering of Ti in oxygen (Ar/O₂ ratio was 80:20) atmosphere. In the same vacuum cycle 270 nm thick Pt was sputtered on top of TiO_x.

The lift-off process was optimized by using water-cooled substrate holder which diminished the resist distortion during TiO_x/Pt sputtering. It was followed by dissolving the photoresist pattern in acetone.

Subsequently, the removal of Al patterns in 4 component etching solution and chemical vapor deposition of SiO₂ insulating layer (denoted by **6**) of 1 μm thickness occurred. Contact holes through the CVD SiO₂ were created by selective wet etching process. By these processing steps, Pt lines insulated by SiO₂ layer and formation of Pt contacts have been carried out (Figure 2.5.).

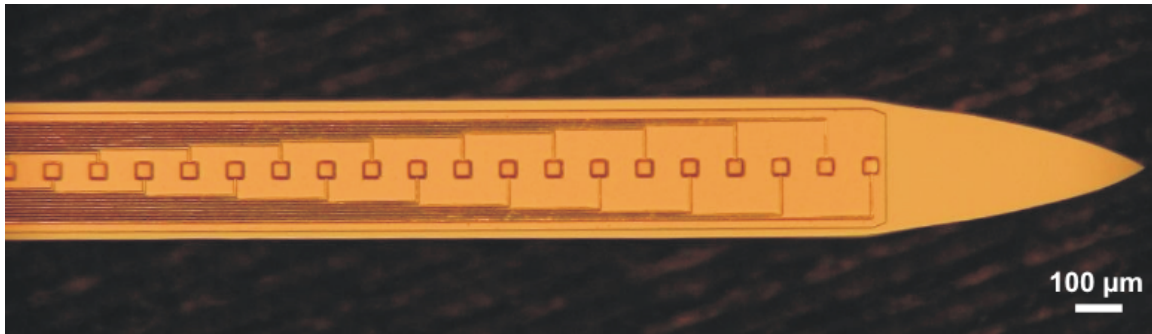


Figure 2.5. Optical micrograph of a probe shaft with thickness and width of 80 μm and 280 μm , respectively. The square shaped Pt contacts have a side length of 30 μm and are contacted to 4 μm wide leads.

In the next steps back side masking patterns were formed by photolithography and wet etching. The first back side lithography defines the supporting frame structure, followed by oxide wet etch in BHF from all the unmasked area. The second back side lithographic step defines the initial shape of the probe and protects the supporting frame, too. Figure 2.6. shows the schematic illustration of a chip with the probe and the supporting frame from frontside (a) and backside (b).

In the following process step SiN_x is selectively etched from the front and back sides of the wafer in hot phosphoric acid.

A 500 nm thick low stress LPCVD (190MPa) SiN_x layer was deposited on the frontside (denoted by 7) in order to use it as a protective coating during the following wet etching on the back side. Insulating and protecting SiN_x and CVD SiO_2 layers were deposited in 2 steps to avoid soaking via pin holes.

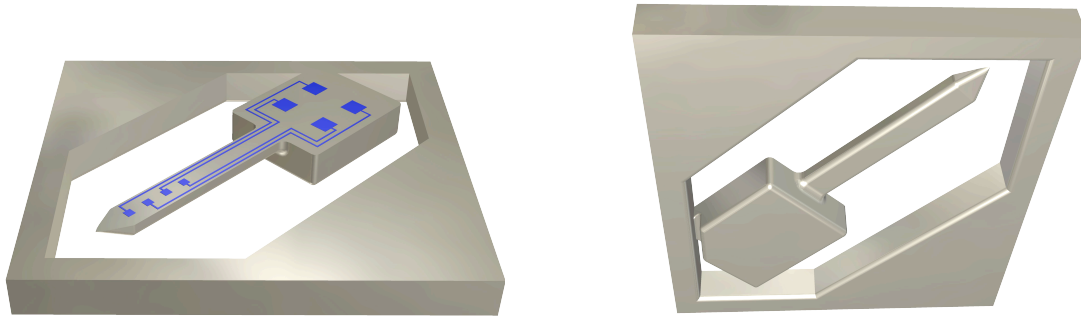


Figure 2.6. The schematic illustration of a chip with the probe and the supporting frame from frontside (a) and backside (b). The four sites and corresponding leads are only the illustrations of the 24 recording sites that can be found on the fabricated probes.

2.4. Probe shaping

Steps #19-22 in Table 2.I., give an overview about the probe shaping as well as Figure 2.4.B-C. On the schematic cross section of Figure 2.4.B. the body of the probe was formed by using back side wet chemical etching in 3 steps. Each probe was connected to a larger Si frame, which made the handling of the probes easier. The frame was protected against corrosion during the etching processes.

On Figure 2.4. and Figure 2.6. the frame is shown on the left- and right-hand sides. 900 nm SiO_2 , 500 nm Si_xN_y and 500 nm CVD SiO_x multilayer stacks were used as a masking structure to protect the probe-holding frame (layer 2, 3, 4 on the back side) and the thicker area below the bonding pads, while a 900 nm SiO_2 layer was used in the formation of the body and tip of the probe (layer 2 on the back side).

The anisotropic etching process was performed in 2 steps. The thickness of the probe was determined by the first step, where the side walls with $\langle 100 \rangle$ and $\langle 010 \rangle$ orientation had been developed, except on the probe tip where the side walls had different orientations. In the next step the SiO_2 masking layer was removed from the back side of the probe, consequently, the top plane of the etched relief silicon pattern was exposed to the etching solution. The etching front propagated parallel to the etched planes having orientation of $\langle 100 \rangle$, $\langle 010 \rangle$ and $\langle 001 \rangle$ until the whole thickness of silicon was removed between the probe bodies. The applied anisotropic etching solution contained a mixture of saturated sodium hypochlorite (NaOCl) and sodium hydroxide (NaOH) in aqueous

solution. This composition differed from the common alkaline etching baths (NaOH, KOH, TMAH) by the addition of a strong oxidizing agent. This etching solution provided a mirror-like, defect-free silicon surface, even after long etching periods. Additionally, a reduction of the anisotropy (A) occurred, i.e. the ratio of the etch-rates ($R_{\langle 001 \rangle} / R_{\langle 111 \rangle}$) decreased. Anisotropy strongly depended on the NaOCl content of the solution. During the long anisotropic etching process, a reflux column was used in order to maintain the concentration level at 78°C. The applied novel type of anisotropic etching formed vertical walls, when the pattern alignment followed the $\langle 100 \rangle$ directions on the $\langle 100 \rangle$ oriented wafer [47]. In summary, in the first step, around 100 μm of Si was removed, followed by the SiO_2 mask dissolution by BHF. In the second step, the final formation i.e. the maskless etching of the needle was carried out, while the chip frame was protected by SiN_x .

The sharp edges of the probe were removed by the next etching step that is isotropic polishing etching. A solution containing concentrated acids have been applied namely, HF and HNO_3 for Si dissolution and H_3PO_4 for the reduction of the etching rate to 7-8 $\mu\text{m}/\text{min}$. An additive (non-ionic wetting agent) was also mixed with the etching solution. The volume ratio of HF and HNO_3 has been chosen to 1:4 in order to have a forced etching rate at the edges of the samples. By using this etching step around 15 μm was removed from each side walls of the probe body. The combination of these different etching methods resulted in a probe shaft having rounded edges and yacht-bow-like sharp tip (Figure 2.7.).

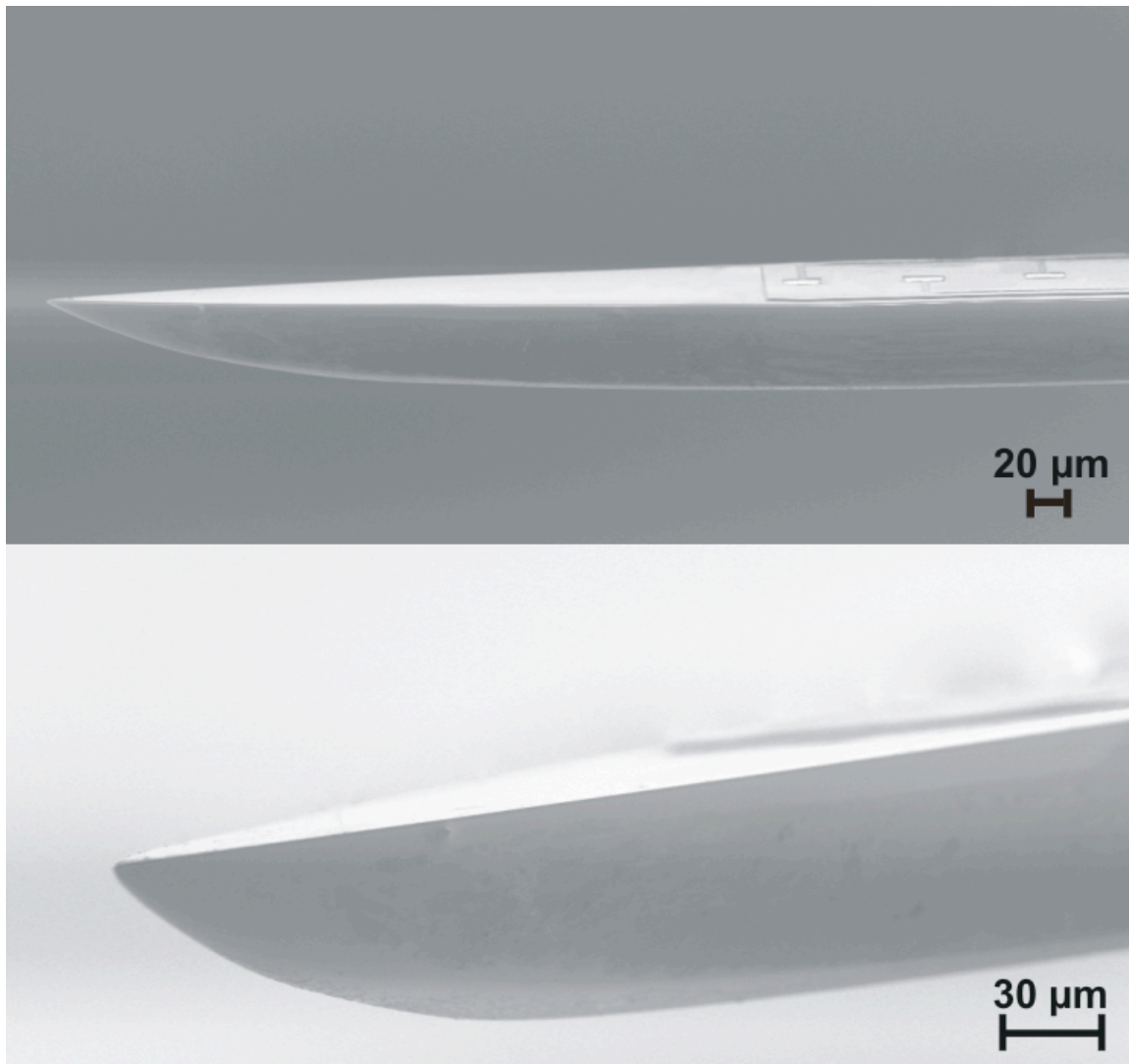


Figure 2.7. Scanning Electron Microscopic (SEM) pictures of the silicon probe. Upper part of the figure shows the probe tip and 3 out of 24 Pt recording sites. The enlarged yacht bow like tip is seen on the bottom figure. Note the rounded shape and smooth surface of the back side of the probe. The imaging was carried out in a LEO 1540 XB SEM equipped with field emission gun, Gemini lens system and in-lens detector.

The residual stress of the passivation layers is so low that it could not bend the probes significantly. To measure the angle of the bending, shafts have been analyzed with optical microscope. The angle difference on the total length of the shaft (7200 μm) was less than 1 degree.

2.5. Packaging

After the removal of the SiO₂ and Si_xN_y protective layers, Pt contacts became uncovered and the probes could be flipped out of the holder frame (Figure 2.8.) one-by-

one. A special thinner connection was developed on the back side of the wafer in order to make the flipping out of the probe easier.

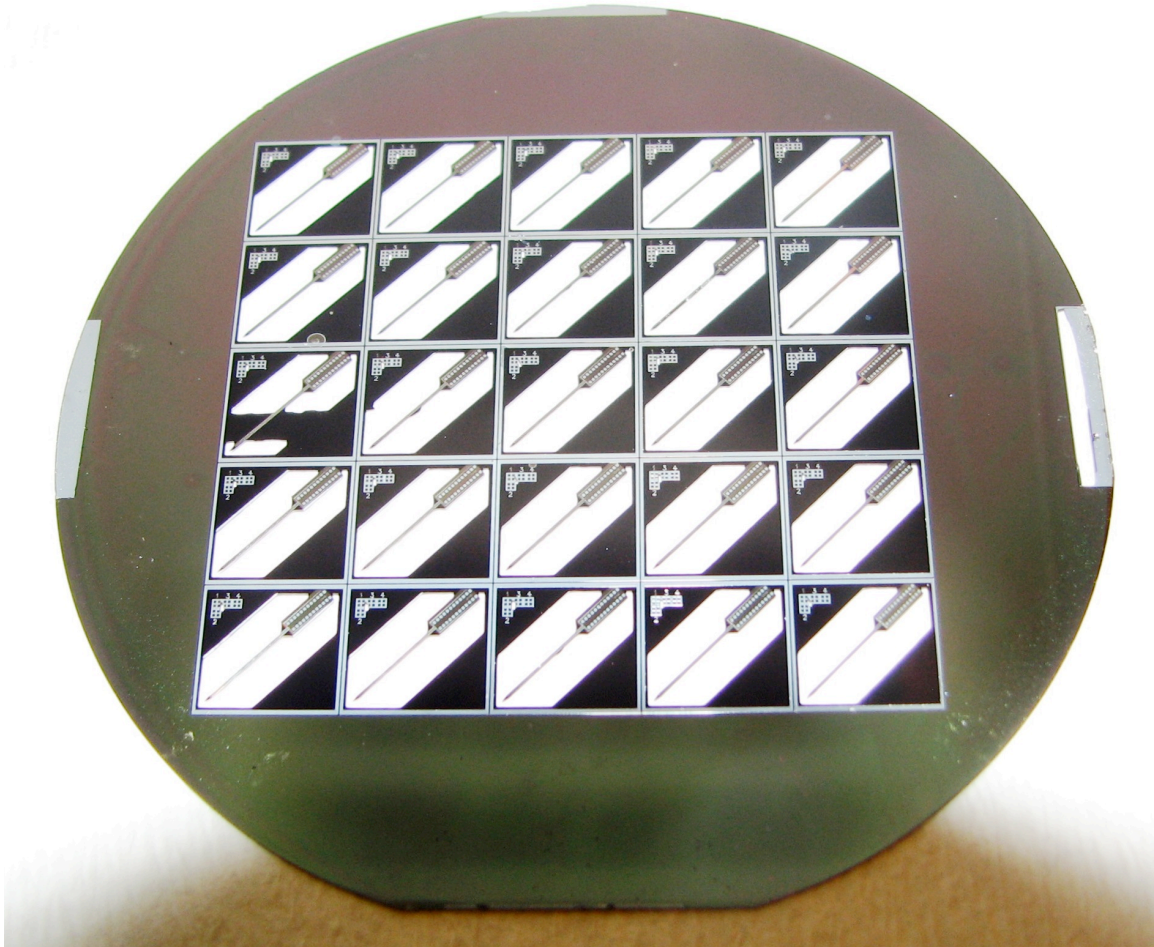


Figure 2.8. Light microscopic picture of a wafer with 25 probes in holder frames. Note that wet etching is not always immaculately accomplished resulting in residuals around the probe shaft (third row in the first column from left). Based on visual inspection for defects (short and open circuits, etching and insulator defects) the fabrication yield was about 40%.

A Printed Circuit Board (PCB) specifically designed for this purpose was used for packaging (Figure 2.9.). The PCB I designed has a length and width of 6.8 cm and 1.2 cm, respectively. On one end of the PCB a 3x5 mm square is found that is not covered with lacquer. 24 gold contact pads are formed on longer sides of that square. The back of the silicon probe base had been glued to that square part of the PCB first with a 2 component epoxy resin (Araldit AY103/HY956). Connection between the silicon probe and the PCB was established via ultrasonic wire bonding (Kulicke-Soffa) using 50 μm thick Al wires. Since Al formed better bonding on SiO_2 than on Pt, SiO_2 -Pt micro grids (200 μm x 200 μm) were designed to form the bonding pads (Figure 2.9. inset). After bonding, the vicinity of bonding area was covered by a drop of epoxy resin to protect it

from damaging. A 26 pole Preci-dip connector was soldered to the opposite end of the PCB but only 24 slots were functional.

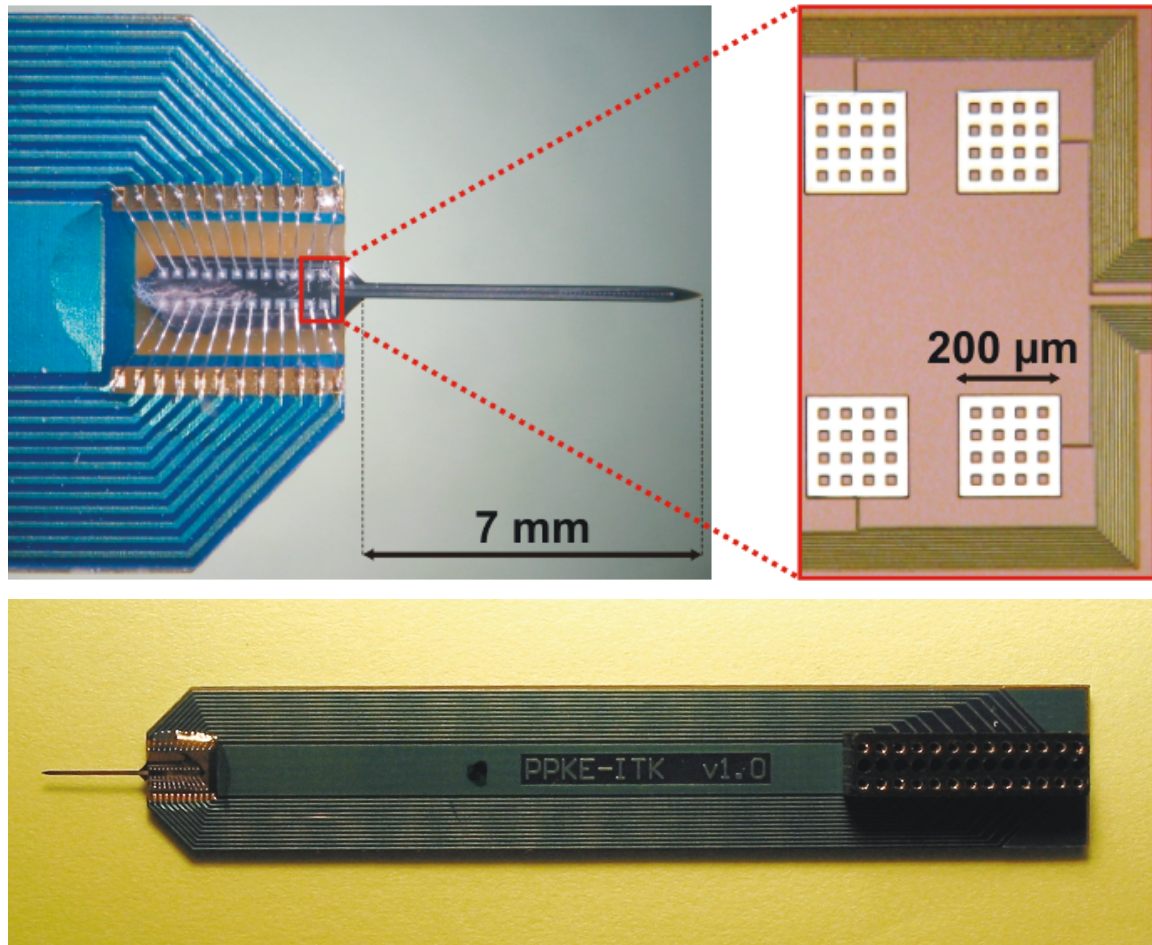


Figure 2.9. Packaging of the acute silicon probe. Inset on the right side of the upper picture shows micro grids before bonding.

3. Results

3.1. Impedance measurement

Before the acute animal experiments were conducted, impedance between each probe site and a counter platinum electrode had been measured in Ringer's lactate solution (Teva Inc., Hungary). Every probe had been cleaned with absolute ethanol first then immersed into Ringer solution. An electroanalytical activation and sensing instrument (BAK model EASI-1, BAK Electronics) was used which measured the impedance at 1 kHz, with sine wave and current less than 500 nA. Average site impedance and standard deviation were calculated using data derived from 3 probes (Figure 2.10.). The average site impedance, calculated by taking into account of $3 \times 24 = 72$ sites, was 1067.36 ± 99.91 k Ω that is consistent with previous results [39].

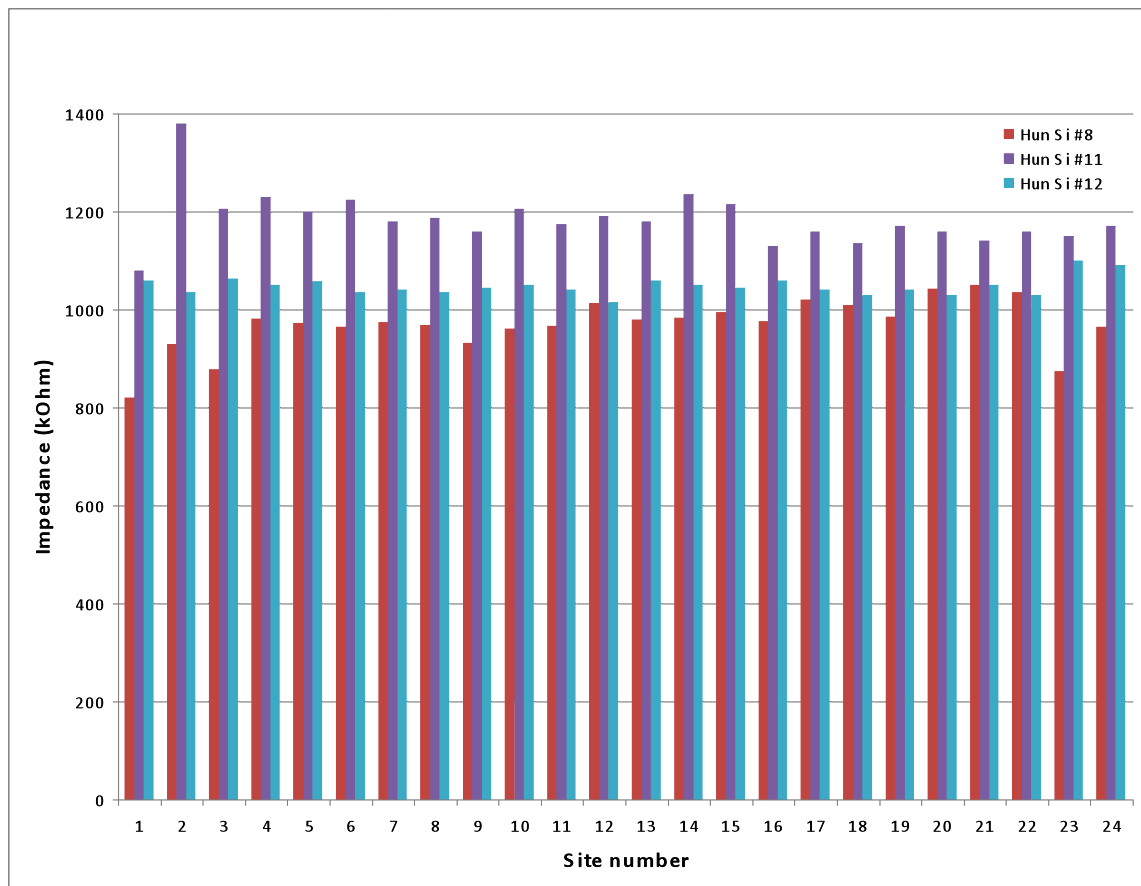


Figure 2.10. Impedance was measured before the acute experiments at 1 kHz with sine wave current less than 500 nA. The figure shows impedance values of 24 sites of 3 probes. Their average impedance was $1067.36 \pm 99.91 \text{ k}\Omega$.

The upper SiO_2 layer must perfectly insulate the extracellular space from leads otherwise the cross-talk between adjacent and even distant channels might increase, moreover shorts can develop. In case of shorts the impedance of participant sites and corresponding leads became similar and decrease significantly.

To investigate whether or not the upper passivation layer leaks I carried out a soak test. I immersed a probe with 2 bad sites into Ringer solution and left it in there for 24 hours. I measured the site impedances in every 3 of the first 12 hours, then 24 hours after the beginning of the experiment. No significant change was observed during the 24 hours timeframe (Figure 2.11.). Average at the beginning continuously increased from $1118.18 \pm 41.91 \text{ k}\Omega$ to $1204.27 \pm 65.66 \text{ k}\Omega$ (at 3 hours), $1248.68 \pm 33.91 \text{ k}\Omega$ (at 6 hours), $1231.86 \pm 32.88 \text{ k}\Omega$ (at 9 hours), $1206.046 \pm 44.94 \text{ k}\Omega$ (at 12 hours) to $1262 \pm 63.28 \text{ k}\Omega$ (at 24 hours). The initial average impedance increased by 6.21% in 24 hours. Given this fact using this probe for acute recording, that rarely takes longer than 12 hours, is safe.

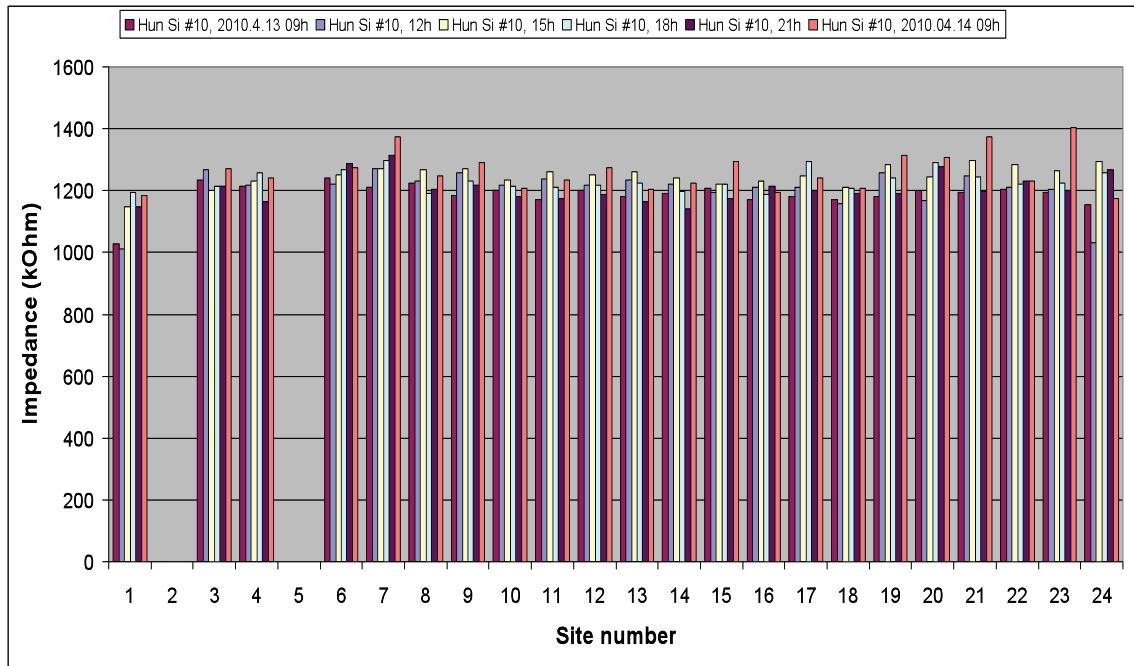


Figure 2.11. Result of a soak test of a probe with 2 bad sites (Nr. 2 and Nr. 5). Impedance measurement was carried out at 3 (blue), 6 (yellow), 9 (cyan), 12 (purple) and 24 (orange) hours after the first measurement while the probe was kept in Ringer solution. The initial average impedance increased by 6.21% in 24 hours.

Decreasing the impedance of Pt is possible by a simple electrochemical etching method. This process makes the smooth surface of Pt sites coarse and therefore extending their overall surfaces. During this electrochemical etching Pt ions leave the metal layer subsequent upon an applied electric field [48]. I applied positive voltage (+ 2V) with the BAK EASI device through an electrode immersed into Saline and negative voltage (-2V) through the probe for 10 seconds. The passing current did not exceed 30 μA . The average impedance of this probe dropped from $1195.12 \pm 113.1 \text{ k}\Omega$ to $659.04 \pm 59.47 \text{ k}\Omega$, which is 55.14% of the initial value (Figure 2.12.). By repeating this process impedance could be reduced to the 300k Ω -400k Ω range. Impedances remained stable, i.e. no significant change was observed in 2-3 consecutive surgeries.

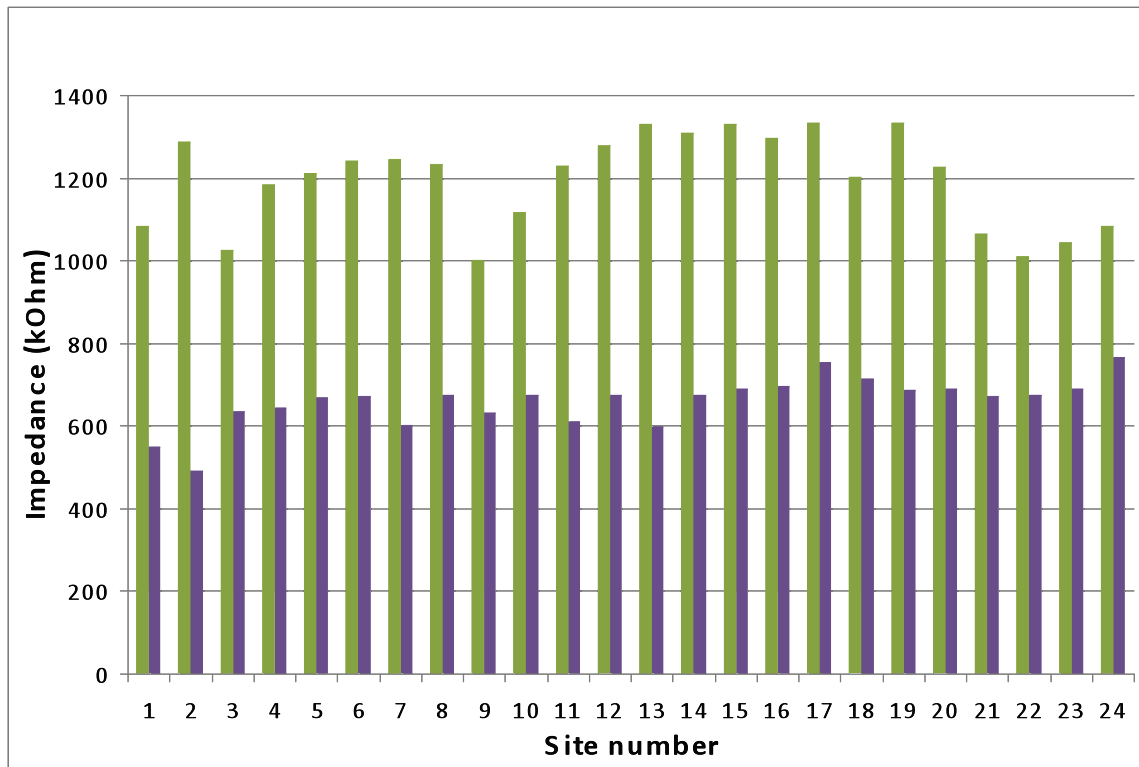


Figure 2.12. Activation resulted in decreased impedance on each site. The average impedance of this probe dropped from 1195.12 ± 113.1 to 659.04 ± 59.47 , which is 55.14% of the initial value. Before activation (green), after activation (purple).

3.2. Neural recordings

Wistar rats (200-300g) were used for the experiments. For initial anesthesia I administered a mixture of 37.5 mg/ml ketamine and 5 mg/ml xylazine at an injection volume of 0.2 ml/100 g body weight via intraperitoneal injections. Sleep-like state was maintained with consecutive updates of the same mixture (0.2 ml/hour). Animals (n=2) were mounted in a stereotaxic frame (David Kopf) and craniotomy was performed over the motor cortex (MC) (AP: [0.0 +3.0], ML: [1.0 +4.0], Reference point: Bregma). The PCB part of the probe was attached to a micromanipulator first, then the probe was inserted into the MC and down to the caudate-putamen (CPu, AP: +1.5 ML: +3.0) in 100 μm steps. Probes could easily penetrate the dura and pia mater without bending or breaking or causing serious bleeding. After recording from MC and CPu for 4 hours, the probe had been explanted, and the rat was sacrificed. All procedures were done according to Animal Care Regulations of IP HAS.

Wide bandwidth data (0.1 Hz - 7 kHz) with gain of 1000 was recorded with 20 kHz/channel sampling rate at 16bit precision (LabView, National Instruments) and stored

on hard drive. The low noise pre- and main-amplifiers, necessary for good quality signal recording, were custom designed and built in house [13].

Multichannel Local Field Potential (LFP, BP filter: 0.1Hz-500Hz, 24 dB/decade, zero phase shift) and Multiple Unit Activities (MUA, BP filter: 500Hz-5000Hz, 24dB/oct, zero phase shift) were separated offline from the recorded raw data via band-pass filtering. LFP and MUA data were analyzed with NeuroScan 4.3 software (Compumedics, El Paso, TX). Off-line analyses included zero phase shift filtering, thresholding, epoching, baselining and averaging of the signals.

Good quality LFP (Figure 2.13) and MUA (Figure 2.14) was apparent on each channel recorded from rat Nr. 1. LFP was characterized by slow-wave components, a phenomenon typical for ketamine-xylazine (KX) anesthesia [49]. 8 sites located in MC and CPu recorded remarkable unit activities, high amplitude spikes well exceeded the background activity (Figure 2.14;Figure 2.15).

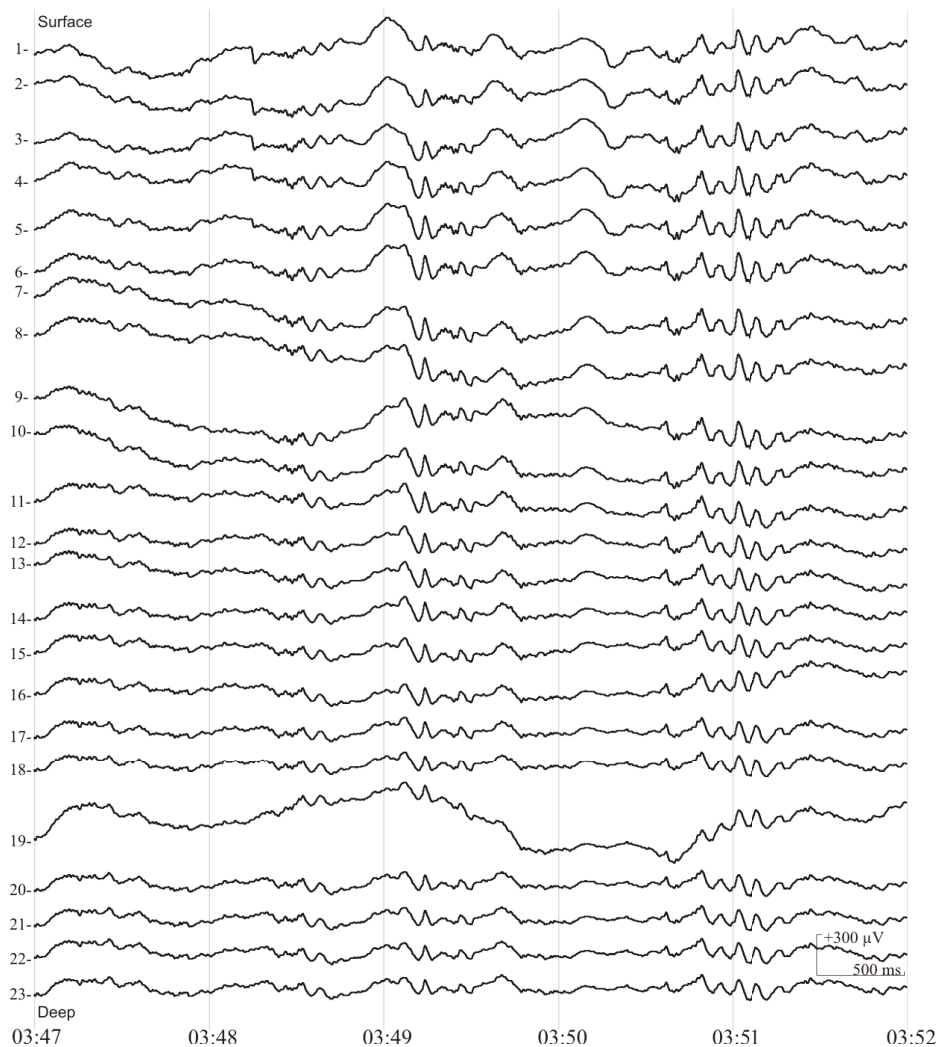


Figure 2.13. LFP recorded from the MC and CPu of rat nr. 1. The 24th channel is allocated for indicating the time of stimuli if it is given. LFP gain: EEG (1k).

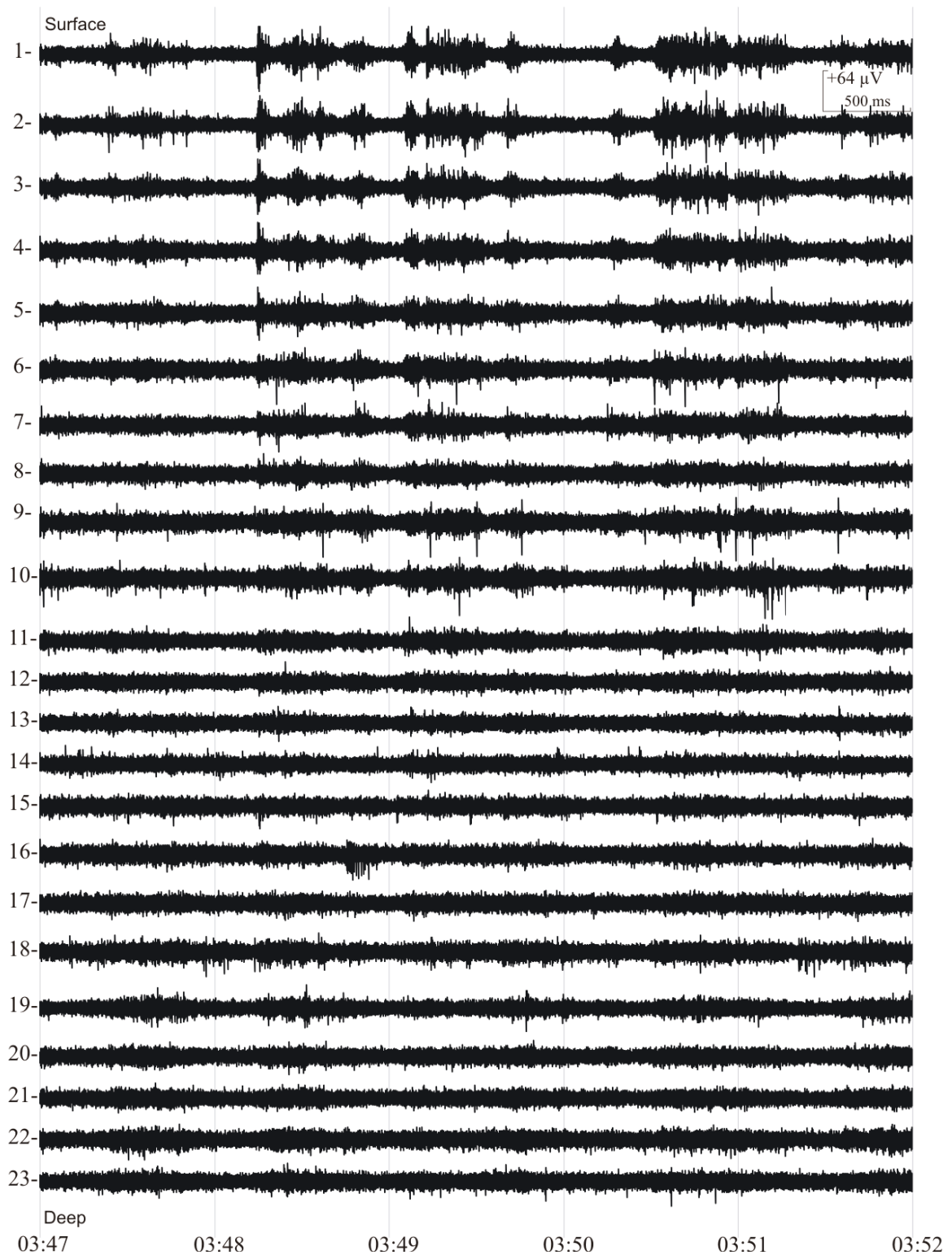


Figure 2.14. Outstanding MUA was recorded from the MC and CPu of rat Nr. 1. Unit activities could be isolated from 8 channels.

Spikes with maximum amplitude higher than $3.5 \times \text{SD}$ had been detected first with the Spike 2 software [Cambridge Electronic Design, <http://www.ced.co.uk/pru.shtml>] then

sorted using the built in CEM sorter of DataView 4.7 demo and Klustawin [<http://www.st-andrews.ac.uk/~wjh/klustawin/>]. Single Unit Activity (SUA) on at least 6 channels had adequately high amplitude activity to be reliably separated from MUAs. Sorted spikes on channel 6, 9 and 12 (n=500 on channel 6; n=438 on channel 9; n=215 on channel 19) are presented on Figure 2.16.A-C.

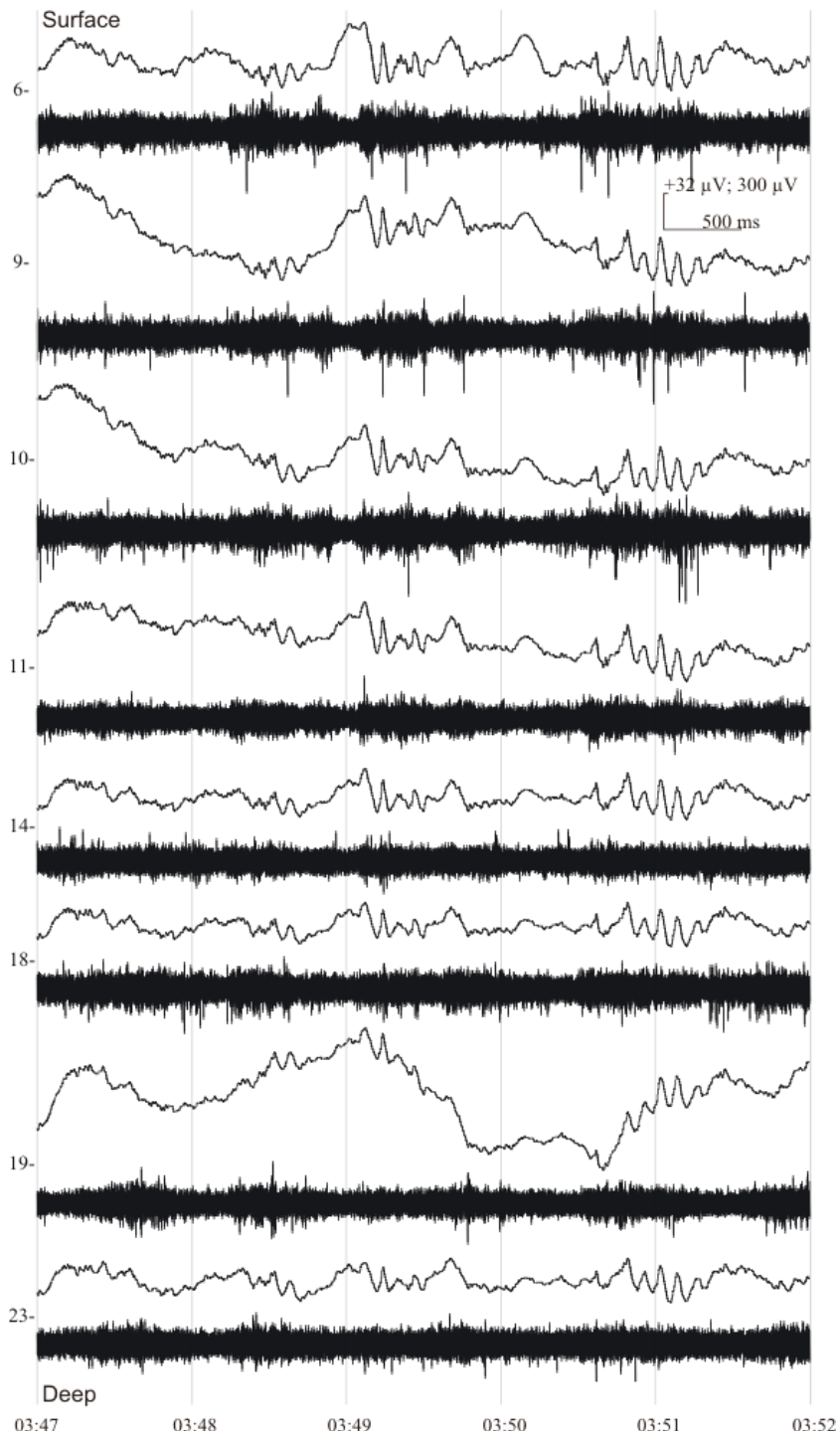


Figure 2.15. Magnified view of LFPs and MUAs belong to channels with good quality SUAs. The vertical scale bar represents 2 values, one belongs to MUA (+32 μ V) and the other to LFP (+300 μ V). Gain: EEG (1 k), MUA (50 k).

On Figure 2.16.A-C. the 10 lowest and 10 highest amplitude spikes, that belong to 3 different neurons recorded on 3 sites (6, 9 and 19), are indicated. The average action potentials (blue) and standard deviations (SD, dotted orange lines) are also shown. The average amplitude of the spike peak is $-37.60 \pm 4.95 \mu\text{V}$ (Nr. 6), $-43.75 \pm 5.26 \mu\text{V}$ (Nr. 9) and $-32.78 \pm 4.13 \mu\text{V}$ (Nr. 19). Auto-correlations (40 bins with 1.5 ms resolution) show refractory periods (-10.25 to 11.00 ms (Nr. 6); -9.25 to 9.5 ms (Nr. 9); -11.5 to 10.75 ms (Nr. 19)) of rarely spiking cortical and a CPU neuron (Figure 2.16.D-F.).

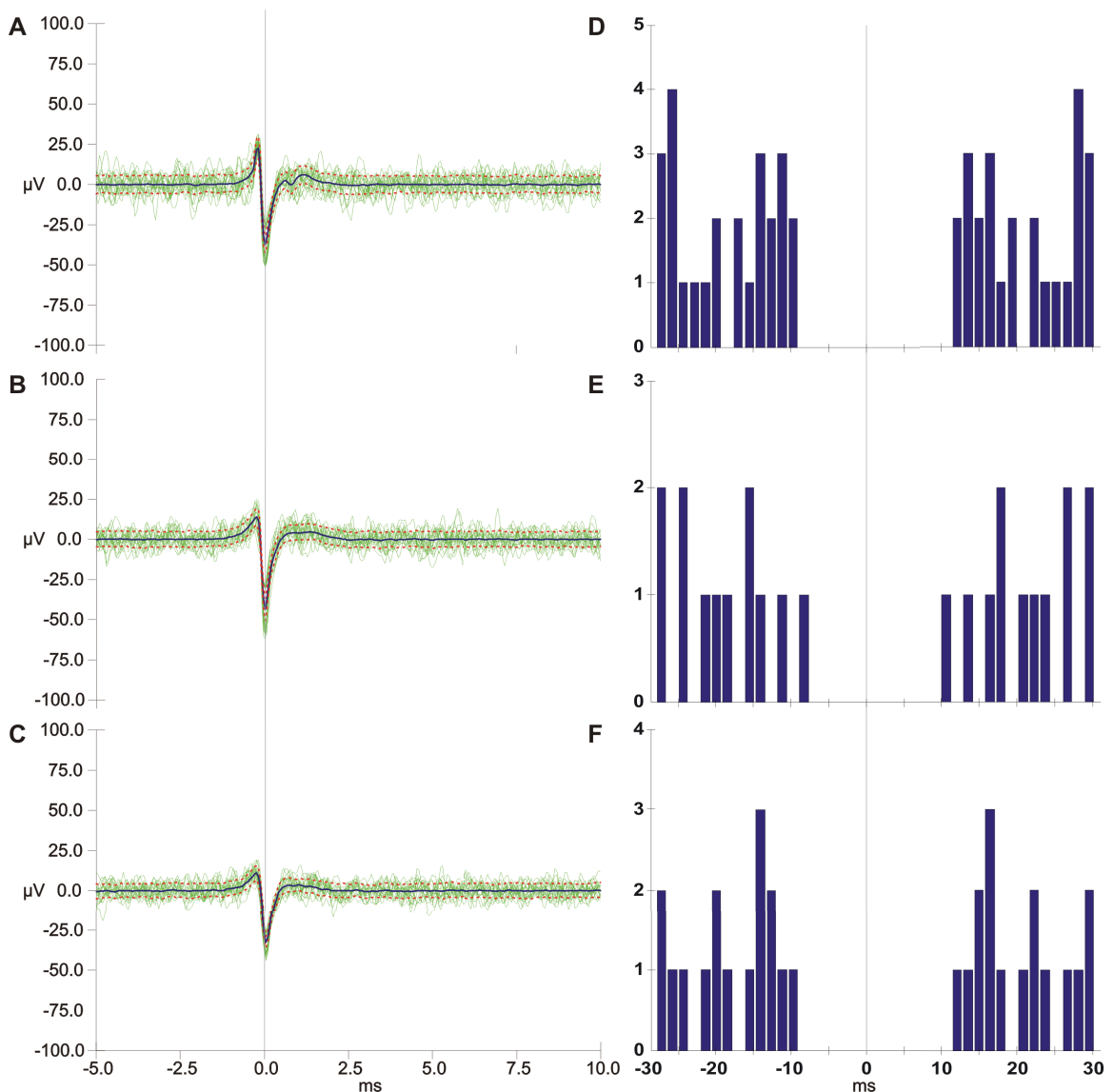


Figure 2.16. (A) 10 lowest and 10 highest amplitude spikes that belong to different neurons recorded on site Nr. 6 (A), Nr. 9 (B) and Nr. 19 (C) is depicted. Their averages (blue) and SDs (dotted orange lines) are presented. Auto-correlograms in the right column indicate refractory period of neuron recorded on site Nr. 6 (D), Nr. 9 (E) and Nr. 19 (F).

In the experiment with rat Nr. 2 another probe was used. In that case every contact recorded good quality LFPs and MUAs from the CPu. Recording site, located closest to the tip (Nr. 1), showed remarkable unit activity (Figure 2.17.) but SUAs on at least 2 channels had adequately high amplitude activity to separate. Other sites located more dorsal but still in CPu could also record clearly distinguishable population cellular firing (MUA) activity. LFP and MUA recorded from tip, middle and distal sites are shown on Figure 2.17.

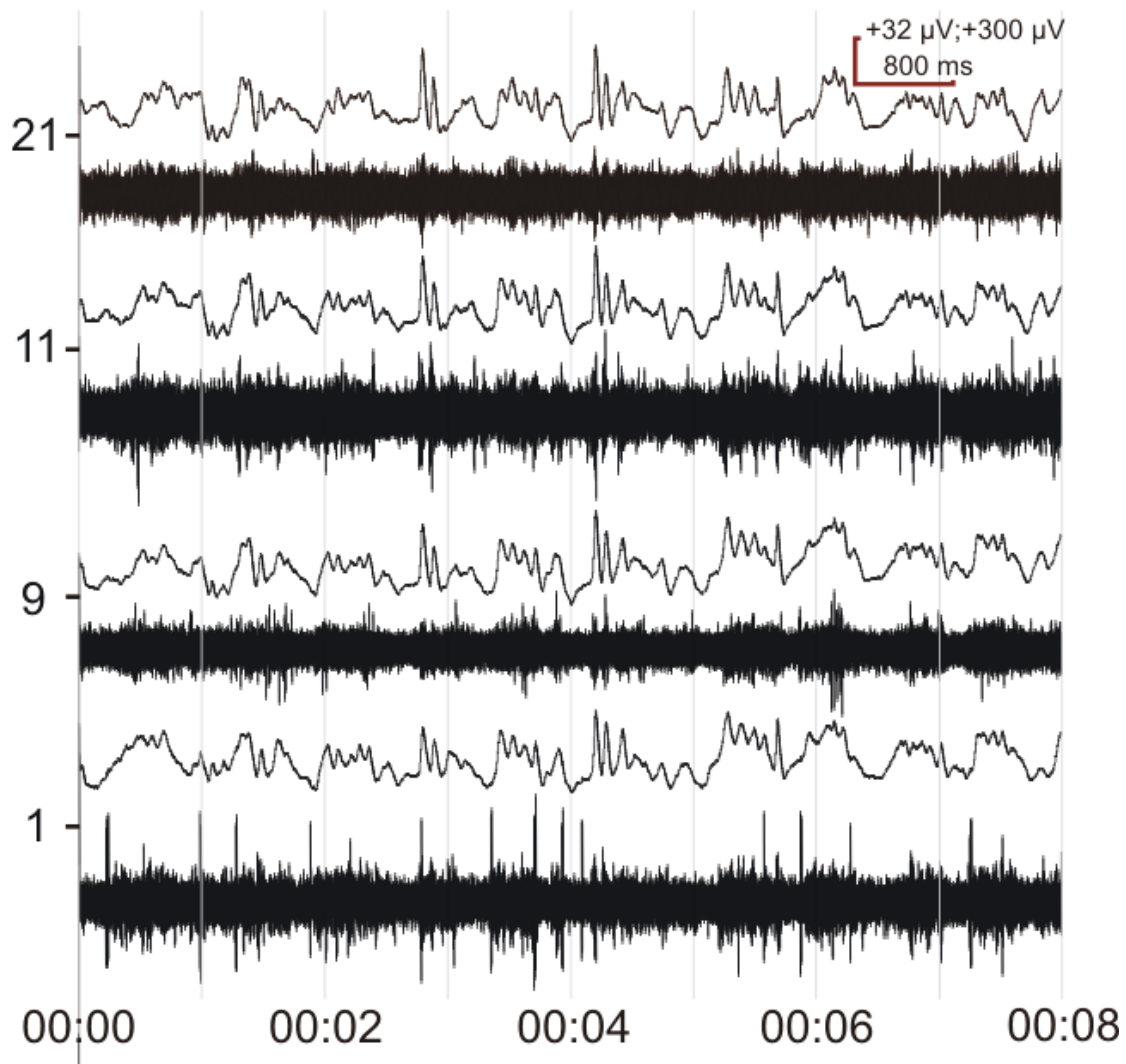


Figure 2.17. Good quality LFP and MUA characterized the recorded signal. Remarkable unit activity is seen in the signal that was acquired with the site located closest to tip (Nr.1). The vertical scale bar represents 2 values, one belongs to MUA (+32 μV) and the other to LFP (+300 μV) respectively. Gain: EEG (1k), MUA (50k).

Spikes ($n=1249$) with maximum amplitude higher than $3 \times \text{SD} = 25.5 \mu\text{V}$ had been detected. The average amplitude of the spike peak is $-41.7 \pm 8.2 \mu\text{V}$ at $50 \mu\text{s}$. Figure

2.18.A. represents the 10 lowest and 10 highest amplitude spikes with green, the average action potential with orange and its SD with dotted black lines. Auto-correlation (60 bins with 0.5 ms resolution) shows preserved refractory period (-1.6 to +1.6ms) and recurrent activity suggestive of a bursting neuron (Fig. 6.B).

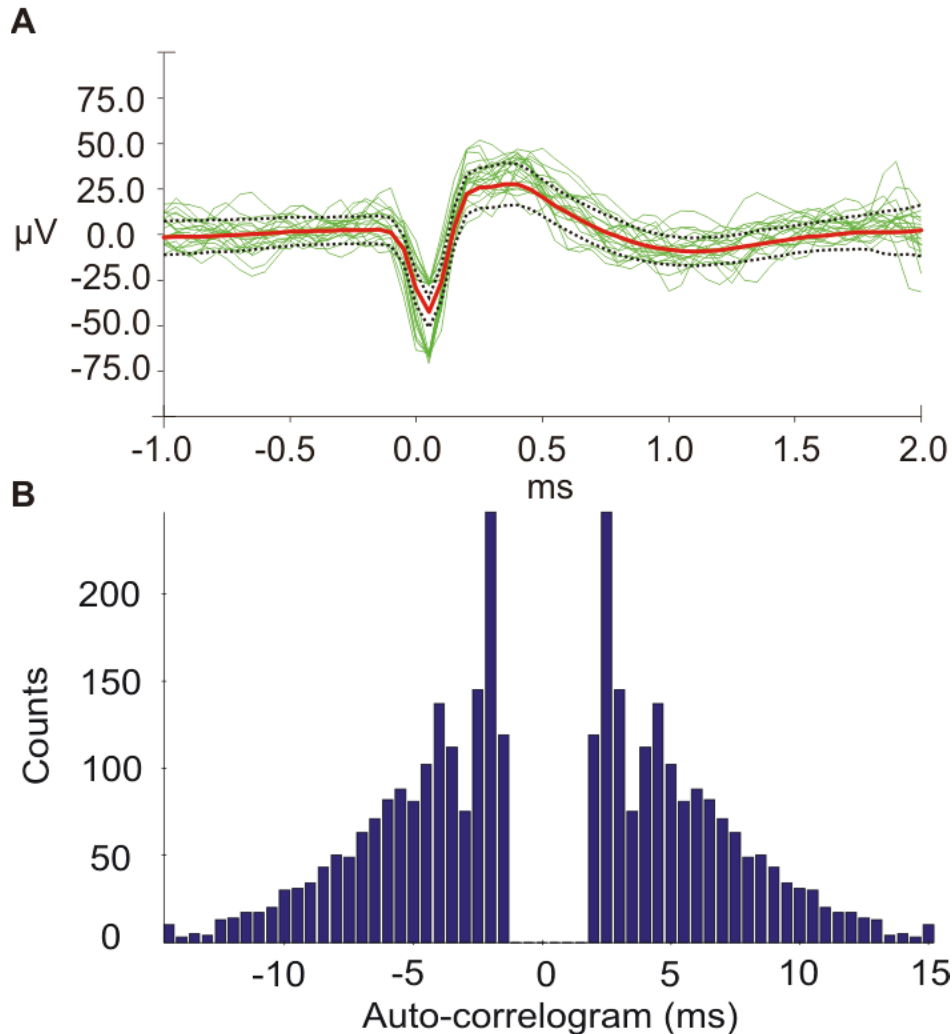


Figure 2.18. A. 10 smallest and 10 highest amplitude firing activities of the same unit, the average of total 1249 spikes (orange) and their SD (dotted black line) are represented. The recording site was located in the CPu. B. Histogram of the first channel unit shows no activity in the -1.6 ms and 1.6 ms range that means clearly distinguishable SUA was recorded on site Nr. 1. 60 bins with 0.5 ms resolution shows count numbers related to auto-correlogram.

4. Discussion and Conclusion

The efficient application of a novel wet-etching process for micromachining multichannel neural probes has been demonstrated here, that is suitable for good quality LFP, MUA and SUA recordings in vivo. Three dimensional probe shaping was carried out by back side wet etching, with frontside protection. Special wet etching was used to

form rounded edges while keeping the tip of the probe sharp, which makes the probe less invasive. One advantage of this probe, in contrast with NeuroNexus probes, that its thickness is variable in the 20-200 μm range by varying the anisotropic etching parameters. The position and the number of the contacts and the length dimension of the probe can be chosen virtually arbitrarily. The average site impedance can be further decreased by using IrO_x or carbon nanotube deposition which procedures increase the overall surface of the sites [24, 50].

This technology offers the same advantages as existing silicon micromachining processes: highly reproducible batch fabrication with uniform small dimensions, multisite structure formation and compatibility with other CMOS circuit integration technologies [11, 18-21, 25, 27, 31, 32, 34, 35, 51-53]. Moreover, highly scalable dimensions and less tissue damaging tip and shaft shape characterize the probes that have been fabricated with our technology.

TABLE 2.II. COMPARISON OF DIFFERENT PROPERTIES OF VARIOUS PROBES

	Hungarian Si probe	NeuroProbes Si probe	NeuroNexus Si probe	Thumbtack polyimide / Stainless steel laminar array
Technology	Wet etching based	DRIE/RIE based	Deep boron diffusion based	Hand manufactured
Shaft thickness (min/max.)	20/200* μm	40*/100* μm	8/20 μm	236-640* μm
Shaft width (min/max.)	80/280* μm	100*/160* μm	20/240* μm	236-640* μm
Shaft length (max.)	7* mm	8* mm	10 mm	10/120 mm
Site number (min/max.)	24	512 (8 work simultaneously)	64	32
Site diameter (min/max.)	2.5/30* μm	20* μm	11*/40* μm	15/40 μm
Site spacing (min/max.)	6.5/100* μm	30*/625* μm	50*/500* μm	50/500
Tip shape	yacht bow like, long	chisel/wedge like	yacht bow like, short	syringe like
Macroscopic mechanical properties	Easily penetrate the dura and pia mater	They can penetrate the dura and pia mater (breaking force: 35-55 mN)	Very fragile (not able to penetrate the dura and pia mater)	Easily penetrate the dura and pia mater (very robust)

* not limited by the technology

On a wafer, 25 chips have been placed. The reproducibility of the probe fabrication is relatively high for an experimental process. However, the wiring turned out to be a critical element. On the average 40% of the chips can be produced with completely flawless wiring, the rest of them have minor mistakes (1-5 point defects).

The dimensions of our current design slightly differ from those that have been published by other groups. Our probes have stable mechanical properties and therefore not fragile, reusable and can be cleaned simply by whipping their surface with a cotton swab. This might be advantageous for some users who require no dura opening during the implantation. The probe can easily penetrate both the dura and the pia mater and the brain surface is less exposed to the environment in addition to negligible superficial bleeding. For comparison of different properties of various silicon probes see Table 2.II.

Considering the advantageous properties of our technological process in dimensional scaling and shaping of the silicon probes, as well as the good mechanical properties of these probes, we expect to be able to produce silicon based devices for deep brain recording/stimulation in the future. Finding the trade-off between small dimensions and stable mechanical properties is not obvious but rather a long term challenge that we can accomplish by fabricating and testing single and multi shank probes with different width, thickness and length.

Chapter Three

SHORT AND LONG TERM BIOCOMPATIBILITY OF SILICON PROBES WITH VARIOUS COATINGS

1. Introduction

Recent neocortical prostheses begin to offer exceptional possibilities for restoring cerebral function [54]. While significant success has been achieved with these approaches, the interface between brain tissue and implanted prostheses or probes can still be greatly improved. Important aspects of this interface include: 1) reaching neurons at the desired location in the brain; 2) ensuring consistent electrical recording and stimulation conditions in the long-term; and 3) rendering the devices as inert as possible in terms of biocompatibility, biostability and biofouling.

The European Project NeuroProbes (<http://www.neuroprobes.eu>) aims to achieve an optimal neural tissue-probe interface. Single and multiple shank silicon based NeuroProbes microprobes are developed and combined with chemical sensors and microfluidic systems [33, 34, 36, 54]. The specific microsystem integration of NeuroProbes is designed so that these features can be integrated into a common platform in a modular fashion [55]. This will permit a consistent and combined use of biosensors, drug delivery paths, electrical recording and stimulation to understand brain function.

Long-term viability and biocompatibility is a key attribute of implanted microprobes. Even materials considered to be biocompatible can induce adverse brain reactions. Two major factors determine the degree of tissue response. First, when a probe is inserted, it causes mechanical damage, damaging brain cells, disrupting blood vessels and thus compromising the blood-brain barrier. Second, an inflammatory neural tissue reaction is induced by both the implant and the injury it causes [11]. This usually results in the development of a glial scar around the probe, which tends to reduce the efficacy of neuronal recording and stimulation [54, 56-61].

Chronic probes are usually implanted for long-term recordings lasting weeks or months. Therefore they should not be susceptible to attack by biological fluids, proteases, macrophages, brain metabolic factors. Silicon seems to be a good candidate as resistant material for long-term recording probes. Surface damage is usually reported if stimulation has been performed through the electrodes of the probe [62]. At the same

time, scanning electron microscopy shows adherent cells and tissue residue on the surface of the explanted probes [57, 63, 64].

Within the NeuroProbes project, we emphasize long term chronic use of the silicon microprobes and seek actively to diminish inflammatory and glial responses to implantation. The silicon surface of the probes was coated by different molecules, in order to produce more biocompatible surfaces for use in brain implants. We followed three main directions. First, we attempted to create a surface resembling the habitual environment of the neural tissue using hyaluronic acid (Hya) coating. Hya is a naturally occurring polysaccharide, which forms an important component of the extracellular matrix [65]. In addition, Hya has an important role in biological processes such as cell motility, cell differentiation and wound healing [66, 67]. Injecting hyaluronic acid into an injured area was shown to reduce glial scar formation in the rat neocortex [68]. Second, we aimed to decrease bleeding due to mechanical damage by coating probes with dextran (Dex). Dex is a complex polysaccharide, used medicinally as an antithrombotic agent to reduce blood viscosity and vascular thrombosis [69]. It binds erythrocytes, platelets, and vascular endothelium, so reducing erythrocyte aggregation and platelet adhesiveness (for reviews see [70, 71]). Clots formed in the presence of Dex are more easily lysed due to an enhanced fibrinolysis [72]. Furthermore, surface immobilized Dex limits cell adhesion and spreading [73]. Thirdly we attempted to reduce tissue reaction by coating probes with the anti-inflammatory drug dexamethasone (DexM). DexM is a synthetic and potent steroid hormone of the glucocorticoid class. Systemic DexM administration attenuates glial responses in rat neocortex [58, 74], but may also have serious side effects [75-77]. Previous work suggests that implanted silicon probes coated with DexM reduces the tissue reaction and lowers neuronal loss [78, 79].

Here we used several microscopical methods to quantify short and long term neuron loss and glial reaction in response to the implantation into rat neocortex of NeuroProbes silicon probes. Light and transmission electron microscopy, as well as stereological methods were used to examine cellular responses and scanning electron microscopy was used to reveal the modifications of the probe surface caused by the brain tissue. The effect on the tissue reaction of different coatings, including Hya, Dex, DexM and Hya/DexM, was investigated.

2. Methods

2.1. Probe implantation and explantation

The biocompatibility of NeuroProbes silicon probes was tested *in vivo*, in the neocortex of Wistar rats ($n=13$). All implanted multiple microprobe had four, 2 mm long shanks, and were non-functional, i.e. were not equipped with output cables. Three different types of probes were implanted (Figure 3.1). 1) E100P probes had shanks with a cross section of $140\ \mu\text{m} \times 100\ \mu\text{m}$ at the connector part gradually decreasing to $100\ \mu\text{m} \times 100\ \mu\text{m}$ close to the tip, with an opening angle of 17° , 5 Pt electrode contacts ($20\ \mu\text{m}$ diameter, and $400\ \mu\text{m}$ distance between contacts) on each shank, and a thin probe base for platform-based assembly (thickness is $300\ \mu\text{m}$, with 4 segments of $400\ \mu\text{m} \times 300\ \mu\text{m}$, E100P = Electrode, $100\ \mu\text{m}$, Platform assembly; details on platform assembly given in [55]). 2) D100C probes had the same shank size as E100P probes but no Pt contacts on the shafts, and a wider probe base for cable assembly (thickness $300\ \mu\text{m}$, dimensions $2440\ \mu\text{m} \times 640\ \mu\text{m}$, D100C = Dummy, $100\ \mu\text{m}$, Cable assembly; [39]). 3) D150C probes had shanks of $150\ \mu\text{m} \times 100\ \mu\text{m}$ at the tip, no Pt contacts, and the wide probe base for cable assembly (D150C = Dummy, $150\ \mu\text{m}$, Cable assembly; Table 3.1., Figure 3.1.). The fabrication process of these silicon-based probes is detailed in [39].

The effect of 4 different coatings was tested. 5 probes – of the same type – were implanted in each rat, one without coating (Si), and 4 with coatings of hyaluronic acid (Hya), dextrane (Dex), dexamethasone (DexM) or a mixture of hyaluronic acid and dexamethasone (Hya/DexM). Two probes (Si, Hya) were implanted in one cortical hemisphere, and 3 (Dex, DexM, Hya/DexM) into the other. All implantations were made in dorsal neocortical areas between bregma and lambda [80]. Surgery was performed under ketamine-xylazine (KX) anesthesia (ketamine: $75\ \text{mg/kg}$, xylazine: $5\ \text{mg/kg}$) and consisted of making independent craniotomies for the 5 probes in each rat. The probes were implanted by hand with a fine forceps, through the intact dura. The extradural superstructure was then embedded into dental acrylic, which was in turn anchored to the bone, thus the probe was tethered to the skull. After implantation, the skin was sutured back.

After fixation of the brain (see below), explantation of the probes was performed manually by grinding away the cranium at the edge of the dental acrylic implant and carefully pulling out the fixed brain by hand. For an experienced histologist, post-fixation

damage is clearly distinguishable from damage originated from the living tissue, thus we were able to exclude any post-fixation artifacts from our analysis.

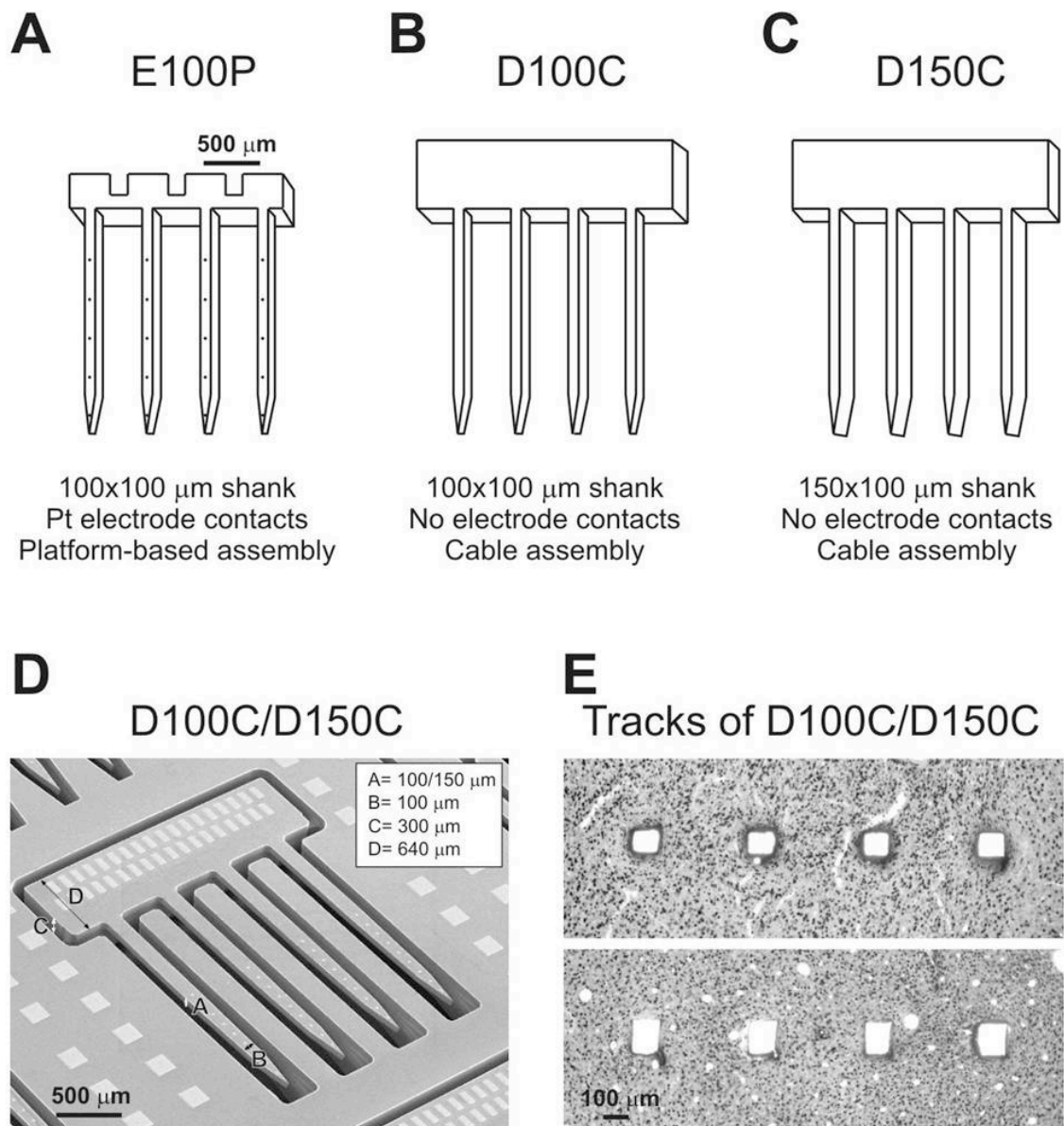


Figure 3.1. Schematic drawing of implanted probe types (see details in [39]). Probes E100P had shanks with a cross section of 100 μm x 100 μm at the tip, 5 Pt electrode contacts on each shank, and a thin probe base for platform-based assembly (A). Probes D100C had shanks of 100 μm x 100 μm , no electrode contacts on the shafts, and a wider, 300 μm thick probe base for cable assembly (B). Probes D150C had shanks of 150 μm x 100 μm , no electrode contacts, and the wide probe base for cable assembly (C). A scanning electron micrograph shows a D100C probe in the silicon wafer (D). Sizes of the probes are indicated. Tracks of D100C and D150C probes are compared on light micrographs from the neuronal marker NeuN-stained sections (E).

TABLE 3.I. IMPLANTED PROBE TYPES AND SURVIVAL TIMES.

Rat	Survival time (week)	Probe label	Electrode contacts	Shank size ($\mu\text{m} \times \mu\text{m}$)	Probe base (assembly type)
NPR-01	1	D150C	-	150 x 100	cable
NPR-02	1	D100C	-	100 x 100	cable
NPR-03	1	E100P	+	100 x 100	platform
NPR-04	2	D150C	-	150 x 100	cable
NPR-05	2	D100C	-	100 x 100	cable
NPR-06	2	E100P	+	100 x 100	platform
NPR-07	4	D150C	-	150 x 100	cable
NPR-08	4	D100C	-	100 x 100	cable
NPR-09	4	E100P	+	100 x 100	platform
NPR-10	12	D150C	-	150 x 100	cable
NPR-11	12	D100C	-	100 x 100	cable
NPR-12	12	E100P	+	100 x 100	platform
NPR-13	8	D100C	-	100 x 100	cable

2.2. Coating procedure

The coatings were performed after fictionalization of both the molecules and the probes in order to allow the covalent bonding of the former onto the later. Thiol groups were introduced onto the probes surfaces through silanisation [81]. The thus functionalized probes were then immersed in pyridine-disulfide substituted Hya and Dex, which then reacted with the thiol groups introduced on the surface. The procedure was slightly different for dexamethasone, where the thiopyridine groups were introduced already on the silanized probe surface [81], and could then react with the thiol substituted anti-inflammatory molecule. The coating procedure was carried out at the Uppsala University Department of Physics and Astronomy within the frame of the NeuroProbes consortium.

2.3. Histology

Animals were sacrificed at 1 week (n=3 animals), 2 weeks (n=3), 4 weeks (n=3), 8 weeks (n=1) and 12 weeks (n=3) after probe implantation (Table 3.I.). They were perfused through the heart with physiological saline followed by a fixative containing 4% paraformaldehyde with 15% picric acid in 0.1 M phosphate buffer (PB). Probes were explanted and stored in the same fixative for processing. The brain was removed from the skull, and postfixed in the same solution at 4 °C, overnight. Horizontal sections (60 μm thick) were cut with a Vibratome, washed with PB, and freeze-thawed above liquid

N₂ in 0.1 M PB containing 30% sucrose. Endogenous peroxidase activity was blocked with 1% H₂O₂. Non-specific staining was suppressed with 5% skim milk powder and 2% bovine serum albumin in 0.1 M PB. Monoclonal mouse antibodies were used against the neuronal marker NeuN (1:3000, Chemicon, Temecula, CA, USA) and the glial fibrillary acidic protein GFAP (1:5000, Novocastra, Newcastle upon Tyne, UK) for 24 hours at 4 °C. The specificity of the antibody was tested by the manufacturer. Immunopositive elements were visualized using biotinylated anti-mouse immunoglobulin G (1:300, Vector, Burlingame, CA, USA) as a secondary antiserum followed by avidin-biotinylated horseradish peroxidase complex (ABC; 1:300, Vector, Burlingame, CA, USA). The immunoperoxidase reaction was developed using 3,3'-diaminobenzidine tetrahydrochloride (DAB; Sigma, St Louis, MO, USA) dissolved in Tris buffer (TB, pH 7.6) as a chromogen. Sections were osmicated (20 min, 0.5% OsO₄), dehydrated in ethanol, and mounted in Durcupan (ACM; Fluka, Buchs, Switzerland).

2.4. Transmission Electron Microscopy (TEM)

After light microscopic examination, areas of interest were re-embedded and sectioned for electron microscopy. Ultra thin serial sections were collected on Formvar-coated single slot grids, stained with lead citrate, and examined with a Hitachi 7100 transmission electron microscope.

2.5. Scanning Electron Microscopy (SEM)

Explanted probes were removed from the fixative solution, thoroughly washed with distilled water, and dried at 40°C for 24 hours. They were covered with a thin gold layer by sputter deposition Emitech K550, and examined in a Jeol JSM-5800 scanning electron microscope.

2.6. Cell counting

In each animal, every 6th section, stained with the neuronal marker NeuN, was used to estimate cell loss around the probe tracks, within the entire depth of the neocortex. Sections containing probe tracks were examined by light microscope, and digitized with high resolution at 10x magnification. For manual analysis of NeuN positive cells, a grid of 100 µm x 100 µm squares was placed over the probe tracks, and neurons were counted in squares at a distance of 100, 200, 300 and 400 µm from the side of the probe tracks. For each distance and coating, cells were counted in 40 to 66 squares. Since neuronal

density can vary in different neocortical layers, control areas were determined in each animal, for each coating. In all cases, 2 times 34 neighbouring squares ($n=68$), covering the entire thickness of the cortex were chosen as control, located at least 600 μm from the probe tracks. Following standard stereological methods, cell bodies touching the top and left side of the grid were counted, while somata touching the bottom and right sides were excluded. Cell loss at a given distance for a given coating was determined as percentage of its control.

2.7. Blood vessel analysis

Two photos of the same size and magnification were used to determine the cross section area of blood vessels in superficial (layers II-III), and deep layers (V-VI) of the cortex. Both photos were taken from the same animal, around the same probe (NPR-10, Hya-DexM). Blood vessels were drawn and measured using the ImageJ program (Wayne Rasband, National Institutes of Health, USA).

2.8. Statistics

When data was normally distributed, one-way ANOVA on Ranks was used. Non-parametric Kruskal-Wallis ANOVA was used if a data set did not pass the normality test.

3. Results

The biocompatibility and the effect of different coatings on NeuroProbes silicon probes were investigated in the rat neocortex in vivo, at short and long terms. Three different types of probes were implanted into the dorsal neocortical areas of rats (see Methods section, Table 3.1., Figure 3.1.; [39]). Glial reaction was described with qualitative analysis around the probe track, whereas neuronal numbers were quantified with manual stereological methods. Qualitative light microscopic analysis did not show notable differences among the cortices of rats implanted with different probe types.

3.1. Neuronal and glial cell distribution in the rat neocortex

The number and distribution of neuronal [82, 83] and astroglial cells [84, 85] in control cortical areas at distances greater than 600 μm from probe tracks were comparable to previous descriptions.

NeuN-stained neural cell bodies were distributed throughout the rat neocortex. In layer I round, multipolar cells were present at low densities. Pyramidal shaped and

multipolar neurons were observed in layers II-III and V-VI. Large pyramidal cells were especially evident in layer V, while in layer IV there were many small, round neuronal cell bodies but no large pyramidal cells (Figure 3.2.A.). Glial fibrillary acidic protein (GFAP) -positive star-shaped astroglial cells with long processes were distributed homogeneously in the neocortex. The superficial layer I contained more positive elements, than other layers. Blood vessels were surrounded by strongly stained astroglial processes, throughout the neocortex (Figure 3.2.B.).

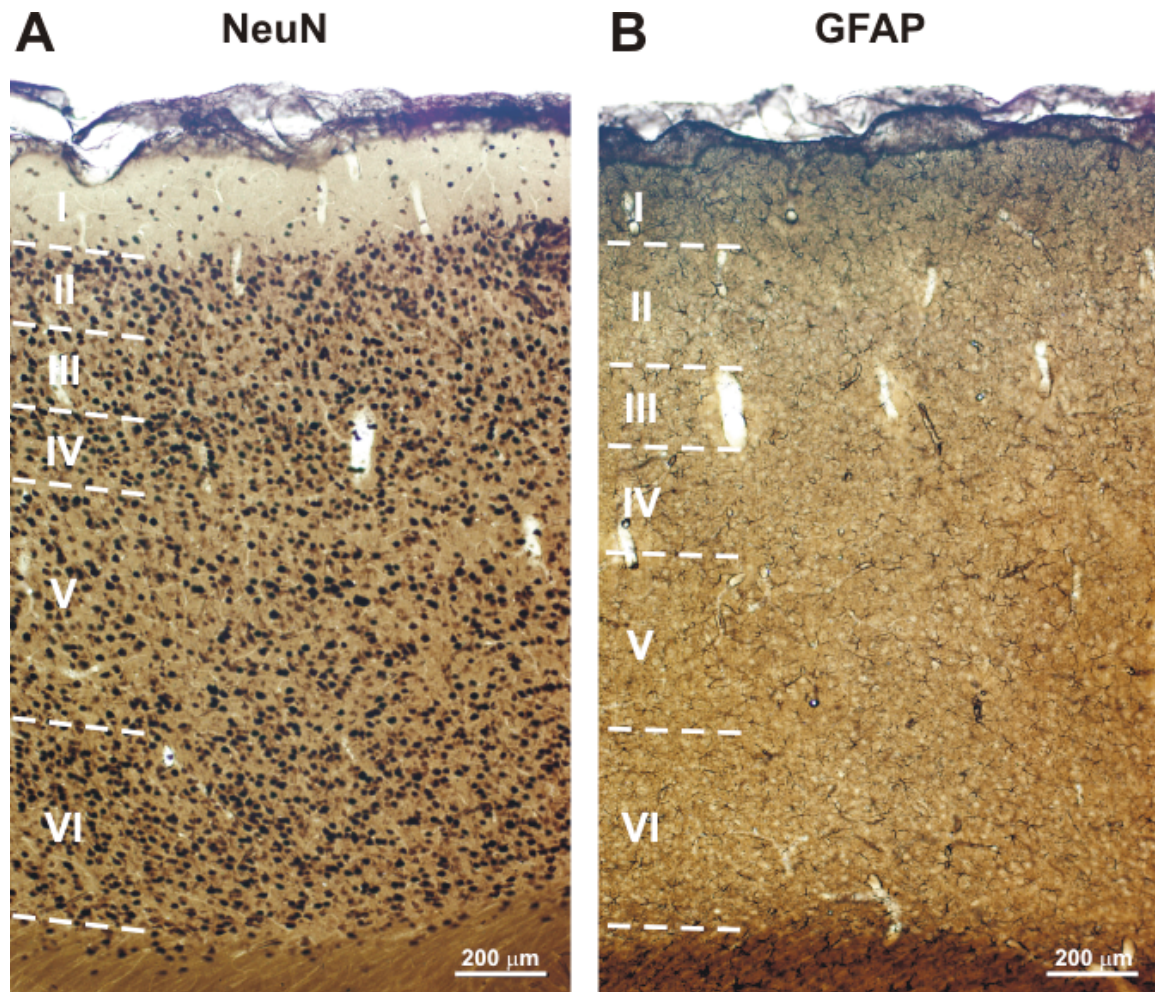


Figure 3.2. Rat neocortex stained with the neuron marker NeuN (A) and the astroglial marker GFAP (B).
The layers are indicated by dashed lines.

3.2. Effect of bleeding during probe insertion

Inserted probes may puncture larger or smaller superficial blood vessels and so cause serious or minor bleeding. Altogether, we inserted $13 \times 5 = 65$ probes. 4 of them hit large blood vessels resulting in severe bleeding that spread to all 4 shanks of the probe. In 8 cases, smaller blood vessels were punctured and bleeding spread to one or 2 shanks. We examined the short or long term effect of bleeding on neuronal and glial cell densities.

Signs of serious bleeding were visible at both 1 and 12 weeks after surgery. Tissue around the probe tracks was damaged and very few, if any neurons or glial cells could be observed. A large hole was typically surrounded by dark, unspecific staining (result of the peroxidase reaction) that masked any stained neural or glial cell (Figure 3.3.A-C.). In some cases, but not always, patches with severe neuron loss were detected near damaged tissue (Figure 3.3.C.), and in these regions glial cells were larger and darker than in the control case.

Dex reduces blood viscosity, erythrocyte aggregation and platelet adhesiveness resulting in a better lysis of clots [70, 71]. We therefore expected a reduced tissue reaction around Dex coated probes that had induced bleeding. Indeed, signs of bleeding were considerably less for the Dex coated E100P probe than for probes not coated with Dex at 4 weeks of survival. A lysed blood clot was outlined by a severe neuronal loss, but we did not detect either dark unspecific staining or damaged tissue (Figure 3.3.D.) at light microscopic level.

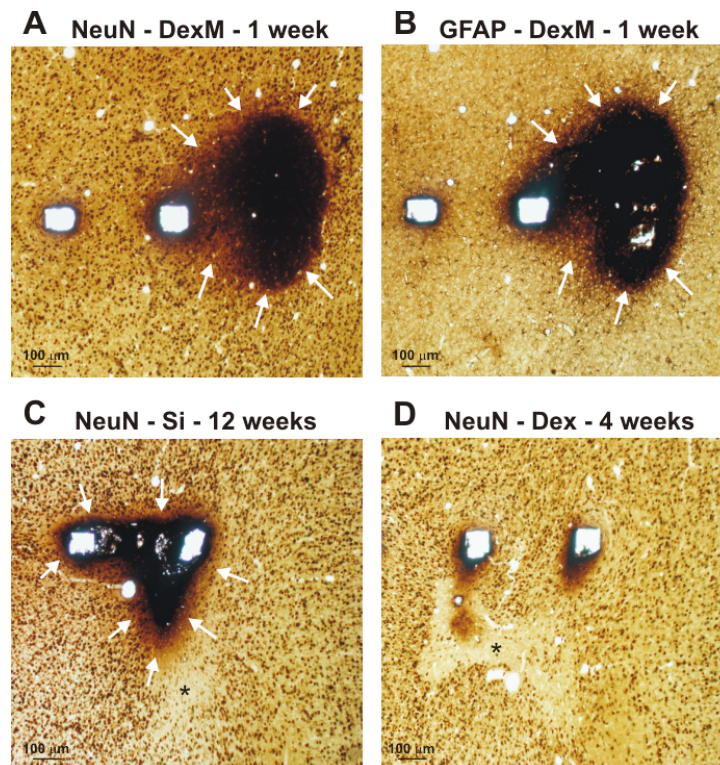


Figure 3.3. Effects of bleeding during implantation. Signs of serious bleeding during implantation were evident at both 1 week (A, B, arrows) and 12 weeks (C). The tissue was damaged around the probe tracks: a dark unspecific staining masked neuronal (A) and glial (B) immunostaining (DexM coated probe). In some cases, patches with severe neuron loss (asterisk) were observed near damaged tissue (C, Si probe) or next to the probe track without the signs of tissue damage (D, Dex coated probe).

Next, we attempted to estimate differences in blood vessel distribution between superficial and deep layers of rat neocortex (Figure 3.4.). We determined the cross sectional area of all blood vessels detected in photos of 2 NeuN-stained horizontal sections, one from layer II-III (supragranular layers), and the other from layer V-VI (infragranular layers). We found 274 blood vessels in a 2.55 mm² area in the supragranular region, with cross sectional areas ranging from 12 μm² to 1467 μm², and a mean of 165±186 μm² (mean±st.dev.). In the infragranular layers, 188 blood vessels were present in the same area. The smallest and largest cross sectional areas were similar to that found in layers II-III: between 12 μm² and 1273 μm². The mean cross sectional area was lower, 132±169 μm². Both small and large blood vessels were more abundant in supragranular layers of the cortex, as shown by the frequency distribution analysis of the blood vessel cross sectional area (Figure 3.4.E.). Blood vessels covered 1.77% and 0.97% of the total cortical area in supragranular and the infragranular layers, respectively (Figure 3.4.F.). In summary, more and larger blood vessels are present in superficial layers, than in the deep layers of the neocortex.

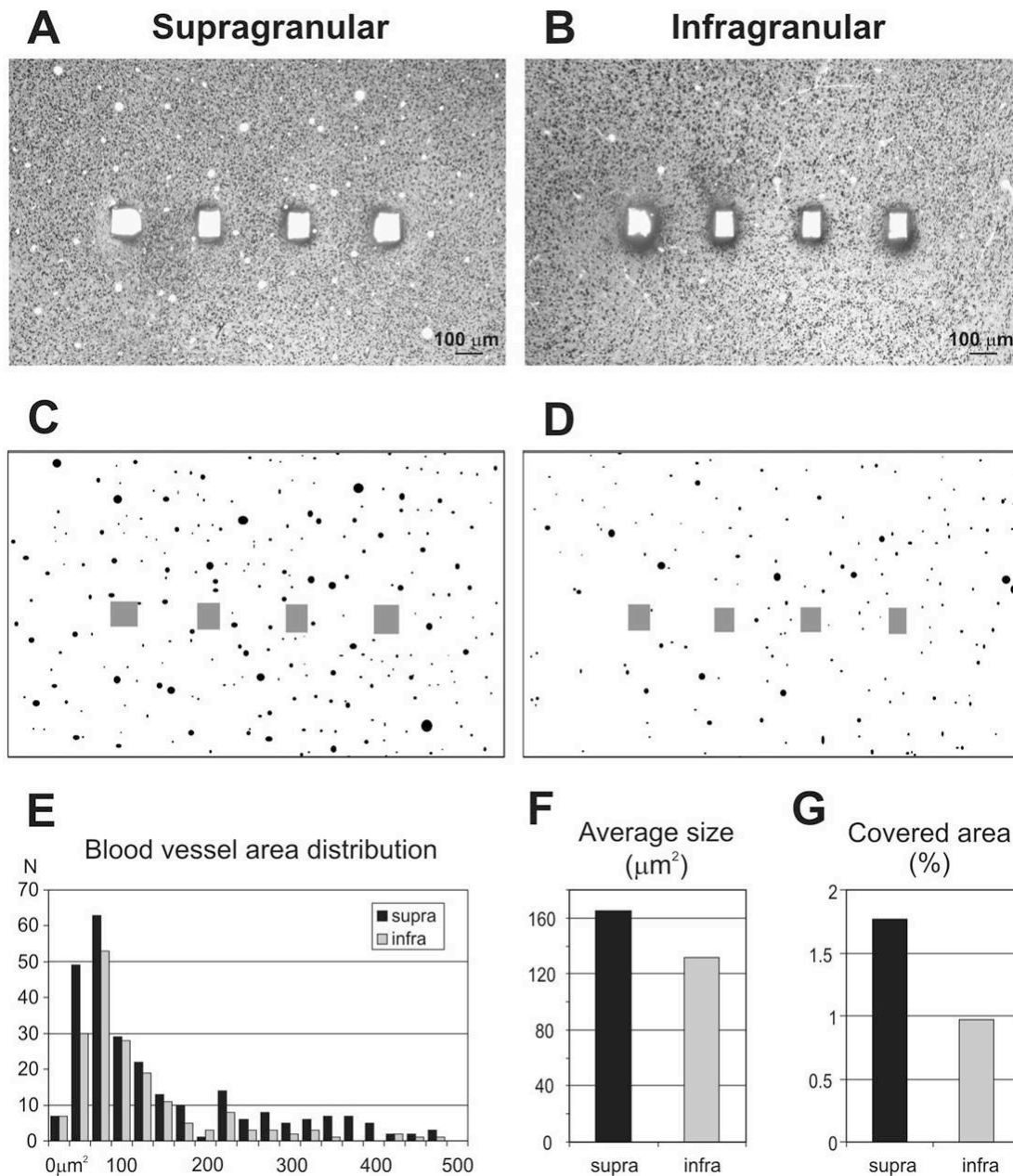


Figure 3.4. Blood vessel distribution in rat neocortex. Photos (A, B) and drawings (C, D) show the cross section area of blood vessels in supragranular (A, C) and infragranular (B, D) layers of the cortex. Both small and large size blood vessels are more abundant in the supragranular layers (E); the average size (F) and the total area covered by the vessels (G) are also larger.

3.3. Effects of different coatings on neuron survival

Different molecular surfaces might differentially influence neuronal and glial survival [11]. We examined this question by quantifying neuron loss and by describing glial reaction around tracks of silicon probes with no coating or coated with different molecules. The following coatings were tested: hyaluronic acid (Hya), dextrane (Dex), dexamethasone (DexM) and a mixture of hyaluronic acid and dexamethasone

(Hya/DexM). Rats were sacrificed after 1, 2, 4, 8 or 12 weeks after implantation (Table 3.I.). Neurons were counted in squares of 100x100 μm around the probe tracks, and at distances of 200, 300 and 400 μm . All probe tracks where severe bleeding occurred during implantation were excluded from this part of the study. Control squares were defined in a line crossing the entire width of the cortex, at least 600 μm from the probe track (see Methods section), and these values were used as a control for cell numbers at sites closer to the probe.

At 1 week survival, we examined neuron numbers (n=21 950 cells in total) in a rat implanted with D150C type probes with different coatings. There was a considerable neuronal loss at distances within 100 μm of all tracks. The proportion of surviving neurons varied from $49.7\pm 2.8\%$ to $76.0\pm 3.6\%$, compared to control with the highest neuronal death near Hya coated probes and the highest survival for the DexM coated probe. (Table 3.II., Figure 3.5.A., Figure 3.5.B.). At distances of 200, 300 and 400 μm , neuronal loss was reduced with values of $80.4\pm 3.5\%$ to $102.0\pm 3.3\%$ of control at 400 μm from the track. The efficiency of the coatings in terms of optimal neuronal survival was the following: Hya<Dex<Si<Hya/DexM<DexM (Figure 3.5.D.). At distance of 100 μm neuronal survival around DexM probe was significantly higher (Kruskal-Wallis ANOVA, $p<0.001$) than around Hya, Dex and Si probes. Furthermore, Hya/DexM showed significantly larger neuron numbers than Hya (Table 3.II., Table 3.III.). Neuronal survival detected at 100 μm from the track of all probes was significantly reduced compared to that at 200, 300, 400 μm , and to control values (Table 3.IV.).

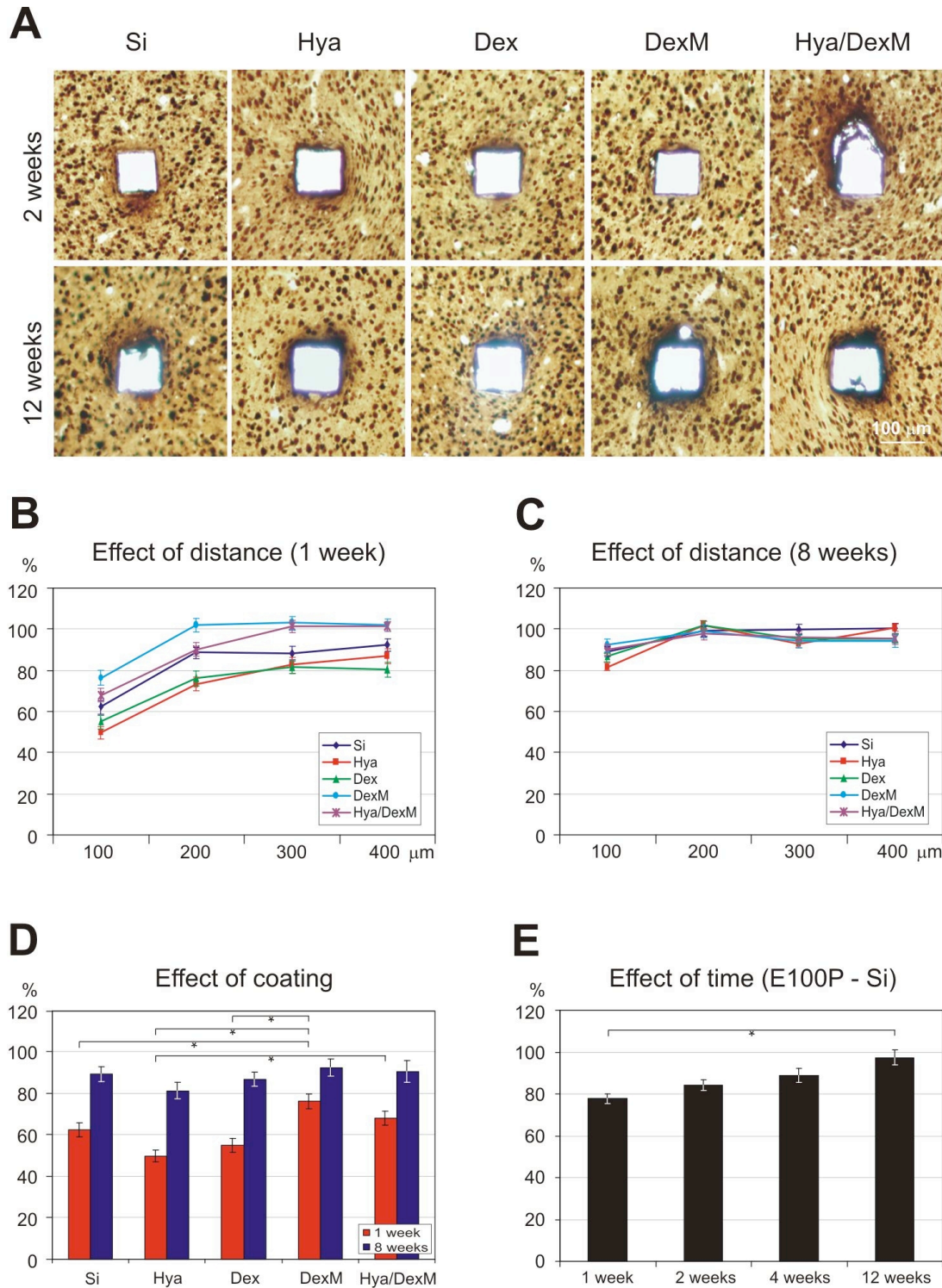


Figure 3.5. Effect of coating on neuronal densities. Light micrographs show similar neuron numbers around tracks made by probes with different coatings (A). The most serious neuron loss was observed at 1 week survival, in the vicinity of the track ($<100 \mu\text{m}$), neuron numbers ranging from 50% to 76% compared to control (B). The neuronal density increases with distance from the track, and with survival time, reaching 80% to 102% at 8 weeks (C). Different coatings affect neuronal survival at 1 week survival, but effects become less significant at longer intervals. The efficacy of the different coatings $\text{Hya} < \text{Dex} < \text{Si} < \text{Hya/DexM} < \text{DexM}$ is similar for short or long term survival (D). Neuronal loss observed at short term decreases with survival time (E). Error bars represent mean \pm S.E.M. * $p < 0.001$

TABLE 3.II. PERCENTAGE OF NEURONS AT CERTAIN DISTANCES FROM THE PROBE TRACK, COMPARED TO CONTROL, AT SHORT TERM (1 WEEK) SURVIVALS. DATA ARE PRESENTED IN MEAN±S.E.M.

1 week	100 µm	200 µm	300 µm	400 µm
Si (n=5396 cells)	62.3±3.2%	88.5±2.7%	88.3±3.3%	92.6±3.1%
Hya (n=4744 cells)	49.7±2.8%	73.3±3.3%	82.7±3.8%	87.1±3.5%
Dex (n=4124 cells)	55.0±3.4%	76.2±3.7%	81.5±2.9%	80.4±3.5%
DexM (n=3798 cells)	76.0±3.6%**	101.8±3.2%	103.0±3.2%	102.0±3.3%
Hya/DexM (n=3888 cells)	67.9±3.4%*	90.2±3.3%	101.3±2.9%	101.4±2.3%

DexM>Hya/DexM> Si> Dex>Hya

** significantly different from Si, Hya and Dex at 100 µm, p<0.001

* significantly different from Hya at 100 µm, p< 0.001

For statistical significances for the different locations around the same probe see Table 3.IV.

TABLE 3.III. NEURON NUMBERS AT CERTAIN DISTANCES FROM THE PROBE TRACK AT 1 AND 8 WEEKS SURVIVAL. DATA ARE GIVEN IN MEAN±S.E.M.

1 week	100µm	200µm	300µm	400µm	Control
Si (n=5396 cells)	12.8±0.7	18.2±0.6	17.8±0.7	19.1±0.6	20.6±0.7
Hya (n=4744 cells)	12.2±0.7	18.0±0.8	20.3±0.9	21.4±0.9	24.5±0.6
Dex (n=4124 cells)	11.8±0.7	16.3±0.8	17.5±0.6	17.3±0.8	21.5±0.5
DexM (n=3798 cells)	14.0±0.7	18.8±0.6	19.0±0.6	18.8±0.6	18.5±0.6
Hya/DexM (n=3888 cells)	14.6±0.7	19.3±0.7	21.7±0.6	21.7±0.5	21.4±0.5
8 weeks	100µm	200µm	300µm	400µm	Control
Si (n=8074 cells)	23.6±0.9	26.3±0.9	26.5±0.9	26.5±0.8	26.5±0.8
Hya (n=8004 cells)	26.4±1.2	32.6±0.9	29.9±1.3	32.2±1.1	32.6±0.6
Dex (n=8649 cells)	24.6±0.9	28.4±0.9	26.8±0.9	26.7±0.8	28.4±0.6
DexM (n=6735 cells)	24.7±1.1	26.6±1.0	25.2±1.2	25.3±1.1	26.6±0.9
Hya/DexM (n=6343 cells)	25.9±1.5	28.1±1.3	27.6±1.3	27.4±1.1	28.7±0.9

TABLE 3.IV. STATISTICAL SIGNIFICANCES FOR THE DIFFERENT LOCATIONS AROUND THE DIFFERENT PROBES, AT 1 WEEK SURVIVAL. * P<0.05, NS= NOT SIGNIFICANT

Si	100 µm	200 µm	300 µm	400 µm	Control
100 µm	---	*	*	*	*
200 µm	---	---	ns	Ns	*
300 µm	---	---	---	Ns	ns
400 µm	---	---	---	---	ns
Control	---	---	---	---	---
Hya	100 µm	200 µm	300 µm	400 µm	Control
100 µm	---	*	*	*	*
200 µm	---	---	ns	*	*
300 µm	---	---	---	Ns	*
400 µm	---	---	---	---	*
Control	---	---	---	---	---
Dex	100 µm	200 µm	300 µm	400 µm	Control
100 µm	---	*	*	*	*
200 µm	---	---	ns	Ns	*
300 µm	---	---	---	Ns	*
400 µm	---	---	---	---	*
Control	---	---	---	---	---
DexM	100 µm	200 µm	300 µm	400 µm	Control
100 µm	---	*	*	*	*
200 µm	---	---	ns	Ns	ns
300 µm	---	---	---	Ns	ns
400 µm	---	---	---	---	ns
Control	---	---	---	---	---
Hya/DexM	100 µm	200 µm	300 µm	400 µm	Control
100 µm	---	*	*	*	*
200 µm	---	---	ns	*	ns
300 µm	---	---	---	Ns	ns
400 µm	---	---	---	---	ns
Control	---	---	---	---	---

We also examined neuronal survival at 8 weeks after implantation. Neuronal densities (n=37 805 cells) were measured in a rat implanted with D100C probes. At distances of 100-400 µm from the probe track, neuronal loss was slight with densities at 100 µm ranging from 81.1±4.0% to 92.2±4.0% of control values, and between 93.8±3.2% and 100.0±2.9% at 400 µm (Table 3.V, Figure 3.5.C.). While neuronal loss was reduced at this long survival period (and the D100C probe was different in size to the D150C probe used in the short survival period experiment), the efficiency of the coatings in terms of optimal neuronal survival followed a similar order: Hya<Dex<Si<Hya/DexM<DexM (Figure 3.5.D.). At long term survival no statistical differences were found either

between the different coatings or between the different locations (Kruskal-Wallis ANOVA, $p > 0.001$).

TABLE 3.V. PERCENTAGE OF NEURONS AT CERTAIN DISTANCES FROM THE PROBE TRACK, COMPARED TO CONTROL, AT LONG TERM SURVIVALS (DEXM>HYA/DEXM>SI>DEX>HYA). DATA ARE PRESENTED IN MEAN±S.E.M.

8 weeks	100 μm	200 μm	300 μm	400 μm
Si (n=8074 cells)	89.0±3.6%	99.0±3.4%	99.7±3.5%	100.0±2.9%
Hya (n=8004 cells)	81.1±4.0%	100.1±2.9%	91.9±4.2%	98.9±3.6%
Dex (n=8649 cells)	86.6±3.4%	100.0±3.5%	94.2±3.5%	93.8±3.2%
DexM (n=6735 cells)	92.2±4.0%	99.2±3.6%	94.1±4.5%	94.2±4.0%
Hya/DexM (n=6343 cells)	90.3±5.4%	97.7±4.4%	96.2±4.4%	95.5±3.7%

We obtained further data on how neuronal survival depends on time and varies with probe type, by measuring neuronal density after implantation of the same probe type at both short and long survival times (Table 3.V.). We counted neurons around E100P uncoated Si probes at 1, 2, 4 and 12 weeks survival (n=38 773 cells, Figure 3.5.E.). At all time points, neuronal loss was largely restricted to distances less than 100 μm from the probe track (Table 3.VI., Table 3.III.). Values for neuronal survival within this distance were lowest at 1 week (77.8±2.3%). 2 weeks after implantation these values were approximately 85% of control. Values at 1 week were significantly different from values at 12 weeks (Kruskal-Wallis ANOVA, $p < 0.001$). At distances of 200 to 400 μm, neuronal density was at least 90% of control values.

TABLE 3.VI. PERCENTAGE OF NEURONS AT CERTAIN DISTANCES FROM THE PROBE TRACK, COMPARED TO CONTROL, AT DIFFERENT TIME POINTS, AROUND E100P UNCOATED SI PROBES. DATA ARE PRESENTED IN MEAN±S.E.M.

	100 μm	200 μm	300 μm	400 μm
1 week (n=8576 cells)	77.8±2.3%*	91.6±2.9%	96.0±2.7%	97.1±3.1%
2 weeks (n=10 557 cells)	84.3±2.5%	93.2±2.5%	89.9±2.1%	89.6±2.5%
4 weeks (n=9965 cells)	86.5±3.6%	99.9±3.2%	99.3±2.5%	100.0±2.8%
12 weeks (n=9675 cells)	85.1±3.5%	98.7±3.2%	97.4±3.3%	100.0±3.4%

* significantly different from 12 weeks at 100 μm, $p < 0.001$

In summary, maximal neuronal loss occurs at 1 week after probe implantation and at distances less than 100 μm . The considerable neuron loss observed at this time point is reduced with time after implantation, as value of neuronal densities returned toward control values. Different probe coatings have an effect on neuronal survival at 1 week. However, this effect is reduced for longer delays after implantation.

3.4. Glial reaction around the probes

Insertion of probes into the brain provokes a glial reaction [54, 56-59, 61]. Both glial cell density and the length and complexity of glial cell processes increase. Gliosis around probe tracks was investigated in qualitative analysis at light and electron microscopic levels of sections stained with the astroglial marker GFAP (Figure 3.6.;Figure 3.7). Native silicon and all coatings of all 3 probe types were examined at all time points (1, 2, 4, 8 and 12 weeks).

In brains examined at 1 week after probe implantation, large, strongly stained “reactive astroglial cells” [84] were visible around the probe tracks, independent of the coating (Figure 3.6.A.). At longer delays, glial cell numbers and shape returned to control levels even close to probe tracks and a dense glial scar was not observed visually, however we did not quantify our results statistically in the case of the glial observations. Light microscopic examination revealed no major influence visually, of probe size or coating on the gliotic response. Larger or smaller glial reactions were sometimes associated with different shanks of the same probe (Figure 3.6.B.), possibly related to localized bleeding. If a major bleeding occurred during probe insertion, tissue was considerably damaged with large, dark glial cells surrounding the injured area.

In summary, slight gliosis was observed visually in all cases, but not a dense glial scar. Furthermore, we could not find any clearly visible correlation between the degree of the glial response and the coating of the probe. Higher glial reaction was usually seen at short survival time (1 week), or around bleedings.

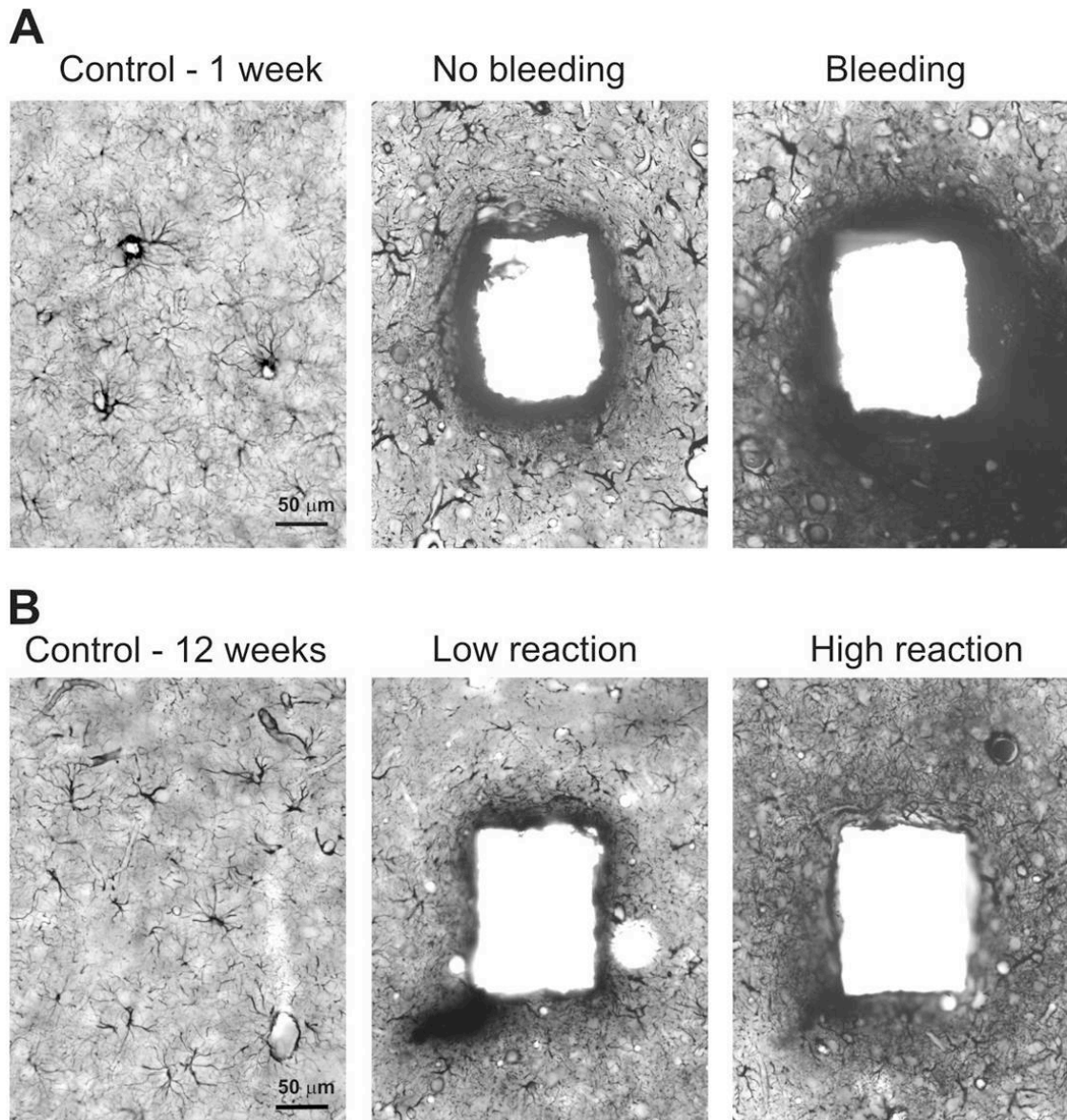


Figure 3.6. Glial reaction around the probe tracks. In general, only moderate gliosis occurred at short (A, middle) and long (B, middle) term survival. Compared to control, larger and darkly stained reactive astroglial cells were visible around the tracks at 1 week survival (A, middle, right). At longer delays (12 weeks, B) glial cell numbers and shape returned to control levels (B, middle). In some cases, lower and higher glial reaction occurred around different shanks of the same probe (A, B), sometimes related to a serious bleeding (A, right).

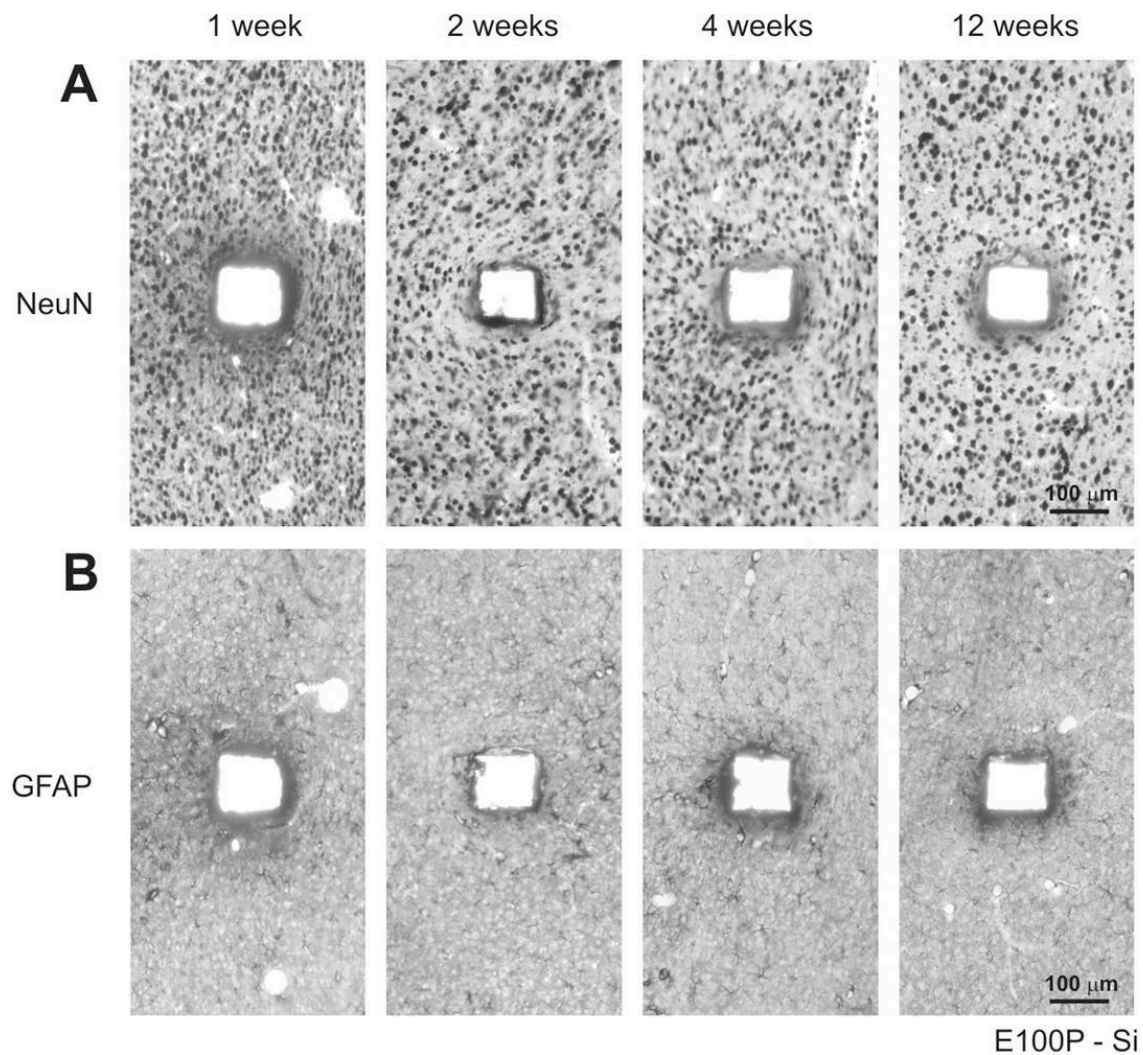


Figure 3.7. Light micrographs show good preservation of neurons (A) and a slight gliosis (B) around native silicon probes after 1, 2, 4 and 12 weeks of survival.

3.5. Transmission electron microscopy of the probe tracks

Light microscopic examination showed statistically significant neuronal loss near probe tracks at 1 week after implantation. This cell loss decreases with distance from the track, and with survival time of the animal. Glial reactions judged by visual inspection were moderate, unless probe insertion provoked bleeding. We pursued the ultrastructural correlates of these changes in neurons and glial cells near probe tracks at the electron microscopic level. GFAP-stained sections were prepared from tissue close to the tracks of E100P Hya coated probes in animals at 1, 2, 4 and 12 weeks after implantation. In the animal at 1 week survival, one shank of the probe had provoked local bleeding whereas no signs of bleeding were detected at the other shanks (Figure 3.6.A.; Figure 3.8.A-B.). In the animal at 12 weeks survival, there was a high glial reaction around one shank but not around the others (Figure 3.6.B., Figure 3.8.C-D.). Comparing various sections let us

examine tissue preservation around the same probe type with the same coating, with or without bleeding and in the presence or absence of a strong glial reaction.

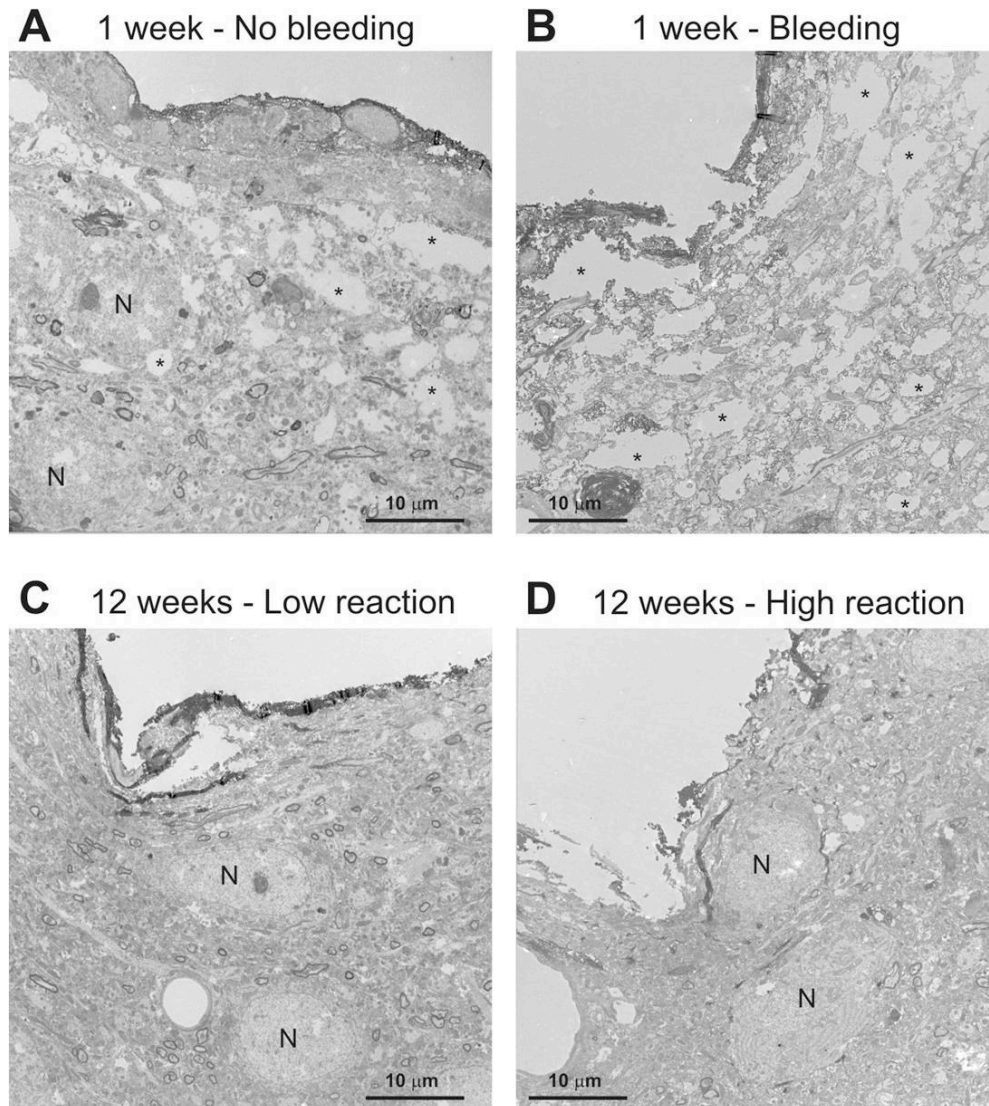


Figure 3.8. Transmission electron micrographs of the probe tracks shown in Figure 3.6. at 1 week (A, B) and 12 weeks (C, D) survival. Large caverns (asterisks) and damaged membranes were found next to the tracks at 1 week survival (A, B), whereas the tissue was not damaged at 12 weeks (C, D). In all cases, neuronal cell bodies (N on A, C, D) were found within 100 μm from the border of the probe tracks.

Numerous neurons were observed at less than 20 μm from the track.

3.6. Neuronal cell bodies - tissue preservation

Healthy neuronal cell bodies must exist sufficiently close to implanted probes for any signal to be recorded. Light microscopy always showed numerous NeuN-stained neurons around the tracks of the probes. In the electron microscope, we examined the cell bodies of neurons located at distances less than 100 μm from probe tracks (Figure 3.8). Neurons were distinguished from glial somata by the absence of the astroglial marker GFAP, by a

light, homogenous nucleus, an electron-dense nucleolus and by a clear cytoplasmic structure and organelles. Immunopositivity for GFAP was used to distinguish astrocytes while glial cell types including oligodendrocytes and microglia possess either very light cytoplasm with poor structure, or exhibit a dark, electron dense homogenous cytoplasm and nucleus [86, 87]. Furthermore, the diameter of neuronal somata is typically 12-25 μm , whereas the diameter of glial cell is rather smaller at 5-10 μm .

At 1 week after probe implantation, we detected considerable tissue damage (Figure 3.8.A-B.). Caverns, degenerating structures and incomplete membranes were observed around all shanks, including those where tissue damage was not apparent in the light microscope. Tissue injury extended to distances of 30-40 μm from tracks where no bleeding occurred (Figure 3.9.A.). In tissues around the track, where bleeding was observed, signs of damage extended over a considerably larger region at distances up to 120-150 μm (Figure 3.9.B.). Glial cells and processes typically formed a layer of 5-10 μm thickness surrounding all probe tracks. There was no evidence for a dense glial scar, but rather glial and neuronal processes were intermingled. Neuronal cell bodies were detected at distances as close as 10 μm from tracks with no bleeding (Figure 3.8.A.), and were never observed closer than ~ 50 μm when bleeding was detected during implantation (Figure 3.8.B.).

2 weeks after probe implantation, tissue damage around the tracks was less than that detected at 1 week. Caverns were distributed in a patchy fashion, and the number of incomplete membranes and degenerating structures was reduced. The glial layer surrounding the track was unchanged. At 4 weeks after implantation, tissue preservation was good and few signs of injury were evident. Healthy neuronal cell bodies were present at distances as low as 10 μm from probe tracks. The glial margin of 5-10 μm thickness was retained. At one edge of one track, we detected an unusually thick and densely packed scar with a diameter of about 10-20 μm .

At 12 weeks survival, tissue preservation within distances of 100 μm from probe tracks was very good and difficult to distinguish from that at distances greater than 300 μm (Figure 3.8.C-D.). We specifically compared tissue where a stronger or weaker glial reaction was observed in the light microscope. Little structural difference was evident although the number of GFAP-positive astroglial processes seemed to be higher in a 30-50 μm thick region around the track with high glial reaction. This network of astroglial processes did not form a dense glial scar according to our light microscopic visual

inspection. Neuronal cell bodies were abundant around the tracks, sometimes at distances less than 10 μm (Figure 3.8.C-D).

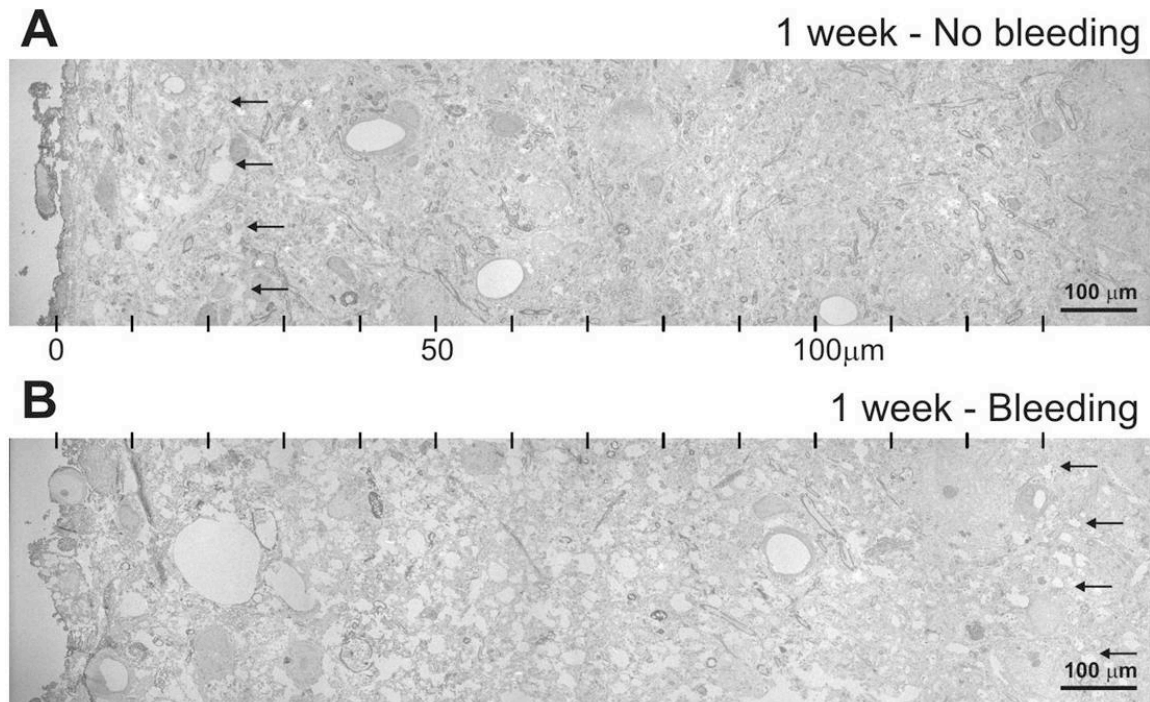


Figure 3.9. Transmission electron micrographs show the ultrastructure of the neural tissue 1 week after probe implantation. In case of no bleeding (A) signs of tissue damage were observed up to 30 μm from the track (arrows). When bleeding occurred (B) the tissue was damaged in a considerably higher radius (up to 130 μm in this case, arrows).

3.7. Synapses

Electron microscopy also permits an estimate of the functional state of synaptic connections between neurons. We examined asymmetric, i.e. excitatory and symmetric i.e. inhibitory synapses close to tracks of implanted silicon probes. Numerous synapses were detected within 100 μm of the tracks at 1, 2, 4 and 12 weeks survival times, as well when bleeding or a strong glial reaction was detected (Figure 3.10.).

Damaged synapses were detected, mostly at one or 2 weeks survival times and their extent was closely related to the degree of tissue damage. Typically, the outer membranes of pre- and postsynaptic elements were discontinuous, whereas the synaptic cleft was unaffected as were synaptic vesicles (Figure 3.10.A-B.). When tissue damage was considerable, asymmetrical (excitatory) synapses seemed to predominate over symmetrical (inhibitory) synapses. In well preserved cortical areas numerous asymmetrical and symmetrical synapses were detected. Synapses of both types were

detected close to probe tracks, sometimes as close as 5 μm when tissue damage was only moderate or very slight (Figure 3.10.C-D).

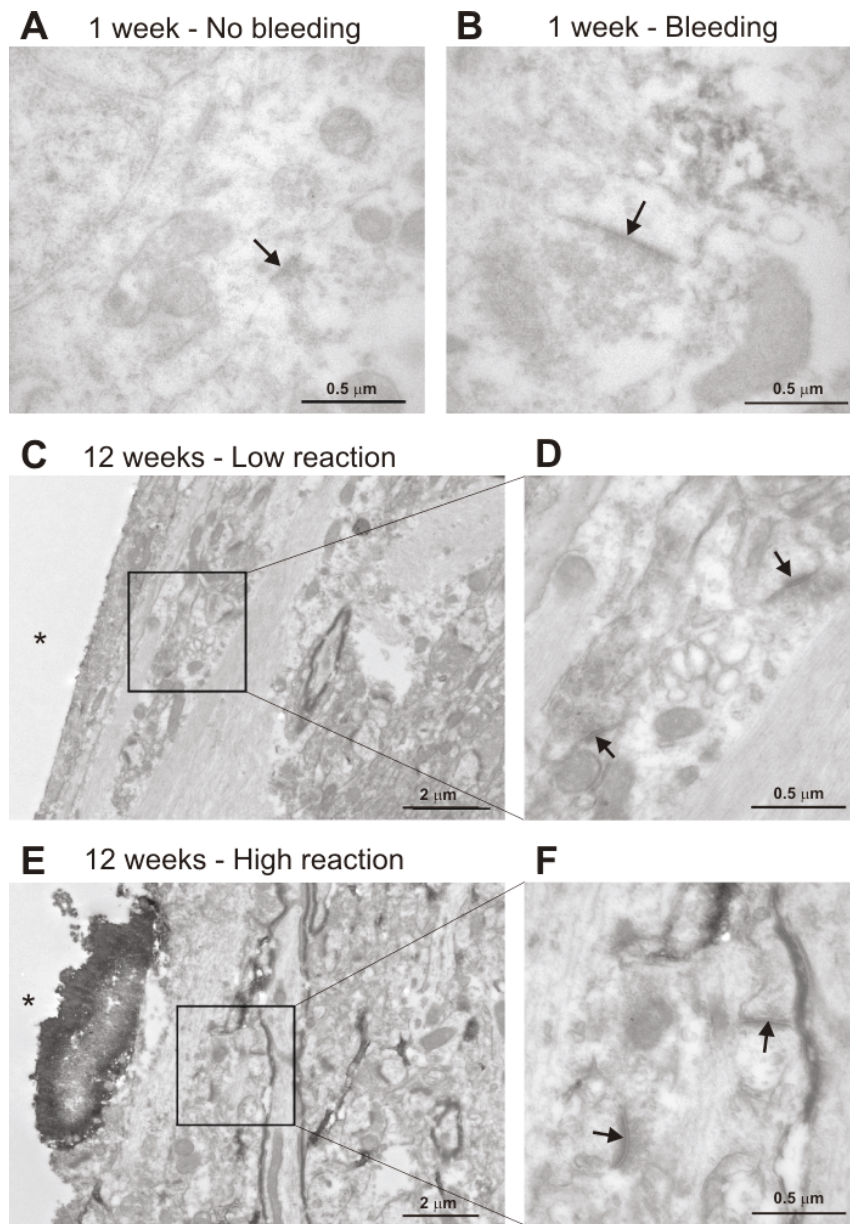


Figure 3.10. Transmission electron micrographs show synapses found close to the probe tracks at 1 week (A, B) and 12 weeks (C-F) survival. Membranes of the pre- and postsynaptic elements were discontinuous when the tissue was damaged around the probes (A, B), but the synaptic cleft seemed to be preserved (arrows). Numerous synapses were found in the close vicinity of the track, at both with low (C, D) and high (E, F) glial reaction. Squares on C and E are enlarged on D and F, respectively. Asterisk indicates part of the track.

3.8. Scanning electron microscopy of the explanted probes

Brain tissue exhibits a glial reaction, including the liberation of inflammatory molecules, in response to injury [56, 61]. Furthermore, extracellular compartments even

in undamaged brain may contain water-soluble elements that affect electrode surfaces. To obtain a qualitative insight into possible changes at the electrode surface without strict statistical power, we examined explanted probes with scanning electron microscopy to see how the surface of the silicon was altered after spending short and long periods in the rat neocortex (E100P probes, 1, 2, 4 and 12 weeks of survival, all different coatings).

As in previous works [57, 64], all examined explanted probes were partly covered by tissue residues and/or by a cell layer (Figure 3.11.A.). We expected obvious differences in the probe surface coverage, due to different attributes of bio-coating molecules: more tissue residues/cells on the good neural adhesion surface Hya coated probe, than on the others. However we detected no clearly visible relation between the covered probe surface and the coating.

Cells with different morphologies remained in contact with the surface of explanted probes. They were typically small, flat and round cells forming a densely packed, continuous layer (Figure 3.11.B.). Less frequently, we detected large multipolar amoeboid cells, similar to fibrous astrocytes (Figure 3.11.C.), as well as fusiform glial-like cells (Figure 3.11.D.) and in some cases red blood cells (not shown) were present. Pt electrode contacts were also covered by tissue residue to different extents from no to total coverage (Figure 3.11.E-F.).

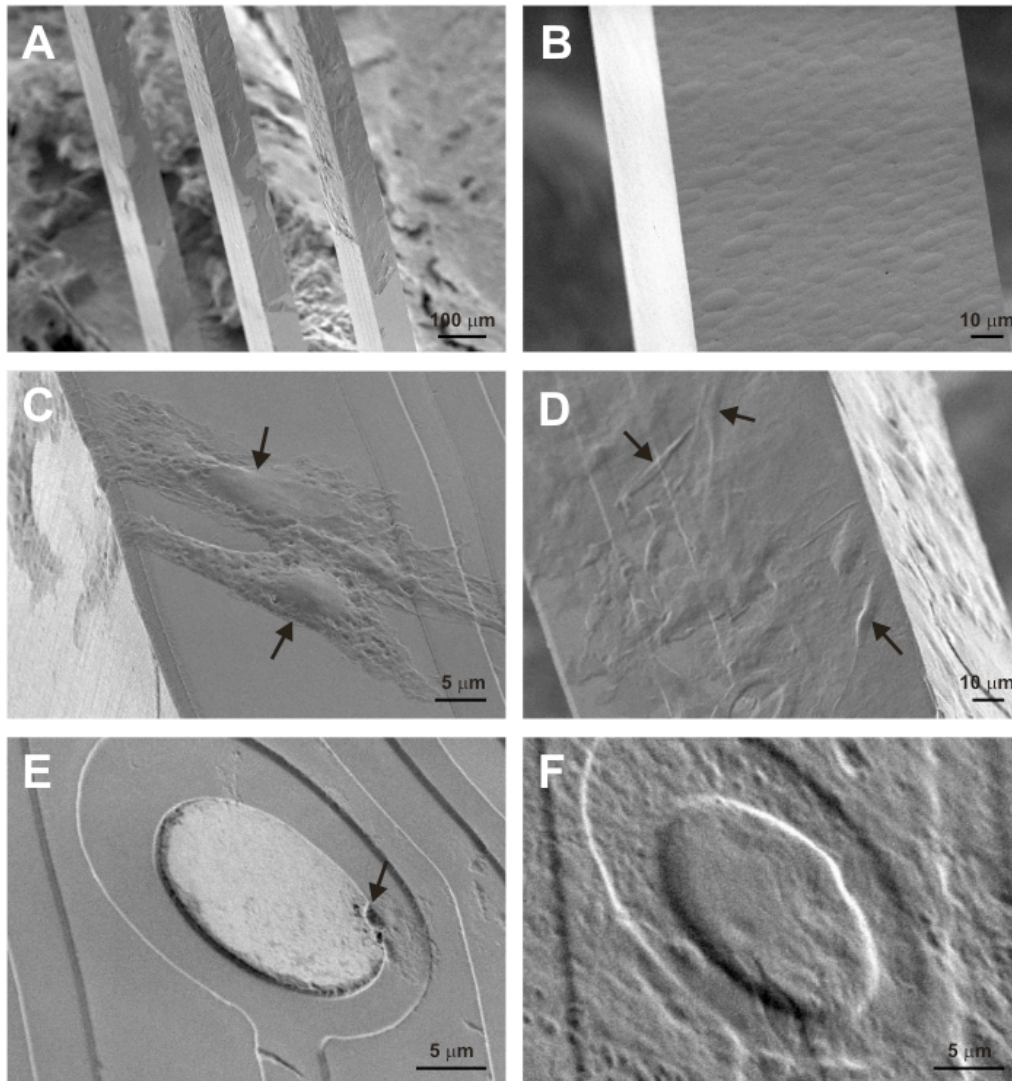


Figure 3.11. Scanning electron micrographs of explanted probes. Low magnification photo shows the tissue residue partly covering the probe surface (A). Usually activated microglia-like, small round cells formed a densely packed layer on the explanted probes (B). Astroglia-like large (C), and small fusiform cells (D) were also observed. In some cases, electrode contacts were free of tissue residue (E), but totally covered contacts were also observed (F).

4. Discussion

Implanted recording and stimulation microprobes are indispensable tools for research on the function of the intact brain, but their utility depends on biocompatibility and long-term viability. Silicon-based surfaces are known to be highly biocompatible [88]. However, acute and chronic inflammatory processes seem likely to affect the surrounding neural tissue ([61]).

In this study we explored the biocompatibility of NeuroProbes silicon probes, and also investigated how the brain environment modifies the probe surface. We showed that

major bleeding during the implantation procedure can result in serious tissue damage. Even without large bleeding, implantation induces considerable short-term neuronal loss. However, neuronal density close to the probe recovers to ~90% of control values at 2-4 weeks after implantation. Some gliosis occurs around probes implanted for short and long periods. Coating the silicon surface with different bioactive molecules has only a minor impact on neuronal loss. DexM coated probes gave the most promising results. The surface of recovered probes was usually partly covered by tissue residue containing diverse cell types.

4.1. Probe implantation

Probe insertion is the first step in long-term brain recording and stimulation. The best recordings are achieved from a neural tissue that is as intact as possible. Several approaches have been tried by different research groups to achieve the best insertion procedure. Similar to our group [13-15, 89-93], many researchers insert the probes by hand [59, 94-97], whereas others use microdrive [5, 16, 98]. Insertion speed might also considerably differ, from slow (100 $\mu\text{m/s}$) [16] to rapid (8.3m/s) [98] insertion. In addition, a more recent report [64] gives an interesting insight to the comparison of hand versus mechanically guided implantation. Biran et al. implanted un-tethered probes by hand and tethered ones with a microdrive. The tissue reaction outcome was favorable for the un-tethered, hand implanted probes. In conclusion, hand implantation may represent a worst case scenario, but it is still a viable and reliable method as indicated by several reports ([61]).

4.2. Effects of bleeding

As it was demonstrated in previous studies [57, 95] we also showed that if a blood vessel is punctured during probe implantation and serious bleeding results, surrounding tissue is considerably damaged. Although neuronal cell bodies were observed in damaged tissue within 100 μm from the track, electron microscopy showed that their membranes were disrupted, and large cavities were present throughout damaged tissue. Electrode contacts located in highly damaged tissue probably generate low quality signals since neurons with incomplete membranes seem likely to be functionally compromised. This hypothesis should be tested with functional probes.

Our work revealed larger and more numerous blood vessels in upper than in deep layers of rat neocortex. Bleeding due to vessel disruption is therefore most likely near the

cortical surface. However, the largest vessels typically run on the cortical surface and so can be visually avoided when the skull is open. Puncture of large vessels during implantation leads to severe bleeding and widespread neuronal death. In this experimental series, large blood vessels were penetrated in only 4 out of 65 cases (6.2%). In previous studies [99, 100], we imaged the vasculature of the superficial 300 μm of the rat cortex, and found a very dense network of vessels. It seems that there is a limited chance to preserve all the fine vessels without precisely imaging the vasculature and specifically plan the probe implantation trajectory. Our blood vessel quantification results further strengthen these observations, and indicate that the chance to avoid bleeding by “blind” implantation is limited.

We used some probes coated with the antithrombotic agent Dex, in an attempt to reduce tissue damage during probe implantation. Considerable bleeding occurred while one such Dex-coated probe was implanted and in this case signs of tissue damage seemed to be reduced. The clot was lysed and characteristic unspecific dark staining disappeared, but neuronal loss was still evident. One case does not permit firm conclusions, but Dex coating may assist clot lysis and reduce tissue response, even though it clearly does not prevent the associated neuronal death.

4.3. Effects of coatings on neuron numbers

Probe surfaces were coated with Hya, Dex, DexM or Hya/DexM, in an attempt to diminish acute and chronic inflammatory and glial responses. Hya, a component of the extracellular matrix, has been shown to reduce glial scar formation in rat neocortex [68]. Dex is an antithrombotic agent helping clot lysis [70, 71], whereas DexM is an agent decreasing inflammatory response [58, 74, 78, 79]. Since all coating molecules are known to reduce tissue reaction, we expected better neuronal survival around coated probes. However only DexM coating had satisfactory effects on neuronal survival, while proportions of surviving neurons with Dex and Hya coated probes were lower than when uncoated Si probes were used (DexM>Hya/DexM>Si>Dex>Hya was the rank order of coating efficacy). As in previous work [64], cell loss was restricted to distances of less than 100 μm from the probe surface. Neuronal loss within such a radius may severely compromise spike records since different types of probes seem to record action potentials only within a radius of 80-100 μm [3, 93, 101].

Numbers of neurons were considerably decreased (49.7 \pm 2.8% to 76.0 \pm 3.6% of neurons surviving compared to control regions) close to all probes during the acute

inflammatory response at 1 week after implantation. Interestingly, cell density was largely restored after 2 months ($81.1\pm 4.0\%$ to $92.2\pm 4.0\%$). This raises the question how neuronal density increases with time. Neurogenesis in the adult rat neocortex is debated, but the consensus is that newly generated cells are glial elements [102, 103]. Possibly neurons migrate back towards the probes when the acute edema decreases. Transmission electron microscopy showed caverns of variable size surrounding tracks at 1 week, within a radius of about $\sim 30\ \mu\text{m}$ with no bleeding and in a radius of $\sim 150\ \mu\text{m}$ with extensive bleeding. These caverns and incomplete membranes presumably result from mechanical damage and the inflammatory reaction to probe insertion [11]. Damaged structures are presumably removed over time [104, 105], permitting surviving neurons to migrate into and fill the volume around the probe.

Our analysis of the pattern of neuronal loss also suggested that surface coating of silicon probes affects neuronal density in the acute but not the chronic phase of inflammatory processes, and only if bleeding during probe implantation is avoided. Conceivably bioactive coating molecules may have been degraded or destroyed by activated microglial cells or macrophages [104, 105].

4.4. Effects of coatings on glial response

Reactive tissue tends to engulf objects implanted in the brain [57, 59, 60, 106-108]. This encapsulation response includes the formation of a glial scar. Such a scar could tend to insulate electrode contacts from neurons, and degrade unit recording quality [57, 108, 109]. In contrast to this pessimistic scenario, as others in a previous study [63], we detected only a moderate gliosis around all probes at all time points, independent of the presence or absence of any coating. Large and more strongly stained reactive astroglial cells [61] were observed at the borders of injured areas both during acute inflammation at 1 week and after site specific bleeding. However while glial processes clearly surrounded probe tracks, the formation of a dense glial scar was not evident in transmission electron microscopy. Electron microscopy also revealed neuronal somata (cf. Figure 3.8.), dendrites, and synapses (cf. Figure 3.10.) at distances as close as $10\ \mu\text{m}$ to probe tracks. Two factors might account for the absence of a notable glial scar. First, the probes used were non-functional silicon probes with no connecting cable fixed to the skull with a reduced possibility of movement that might aggravate mechanical injury [64]. Second, we assured probe sterility by storage in ethanol until surgery and transfer to distilled

water a day before use. Such enhanced sterility standards may reduce astroglial encapsulation of implanted probes.

4.5. Surface of the probes

We examined the surface of probes implanted in the brain for different time periods by scanning electron microscopy. Cells of diverse morphologies were detected in the tissue residue covering explanted probes. Since Hya is an extracellular matrix element, we assumed it might provide an adhesive surface to attract neurons and glial cells. However, Hya coated probes were not covered by a more profuse tissue residue than uncoated probes. Furthermore, as suggested [59], the quantity of tissue residue was uncorrelated with the duration of the implantation. We note however, that the quantity of tissue residue and the number of cells visible on the surface of the explanted probes might also depend on the probe removal method. Our probes were removed manually after perfusion. It is possible that different removal procedures may provide more tissue residue on the probe surface, but a standardized removal method has yet to be established to effectively compare tissue residue on differently treated probes.

Cells with different anatomical features were distinguished on the probe surface (Figure 3.11.). The small, flat, round cells forming a densely packed continuous layer probably correspond to activated microglia [64]. The large multipolar, amoeboid cells resemble fibrous astrocytes [74, 110] or fibroblasts [111], whereas the fusiform cells may correspond to either glial cells [74] or macrophages [64]. Specific staining techniques are needed to identify definitively the cell types that attach to probes.

4.6. Conclusions

Biocompatibility and long term viability are crucial questions for chronic applications of implanted devices. Our data shows that the silicon-based microprobes developed in the framework of the NeuroProbes project are highly biocompatible. Neuronal loss around the probes was evident at 1 week after implantation within distances of 100 μm from the probe track. However, it was considerably reduced with time, with neuronal densities returning to 90% of control levels at 2-4 weeks after implantation. Disruption of major blood vessels resulted in considerable tissue damage, destroying most neurons over an area with a radius of several 100 μm . Both light and electron microscopic analyses showed a moderate gliosis around the probes in cases of minor or no bleeding, but a dense glial scar did not develop. We coated the silicon surface of the probes with

different bioactive molecules in order to diminish tissue reactions. Coatings had minor effects on neuronal survival with only DexM showing an improvement as compared to native silicon probes. Our study suggests that avoiding blood vessel disruption during implantation may be a very important factor in preserving neuronal density around implanted devices.

*Chapter Four***INFORMATION PROCESSING IN THE CAT AUDITORY CORTEX DURING THE NATURAL SLEEP-WAKE CYCLE AND ANESTHESIA****1. Introduction**

Sensory processing undergoes fundamental changes as vigilance level turns from activated to quiescent states. Traditionally, thalamus was thought to be the main vigilance state dependent gate of sensory information flow [112-114] towards the cortex, however emerging findings questioned this assumption [115-117]. Over 40 years, only a few reports have been published about information processing in naturally sleeping animals even with applying simple stimuli. Lesser data was derived from non-rodents but higher order species in chronic experiments and only a very few which tried to explore the role of cortical layers in sensory processing during sleep in a specific sensory cortical area, as the auditory cortex. Thus, despite decades of research, the cortical neuronal mechanism of altered acoustic sensory processing in natural slow wave sleep (SWS) is unknown [116-122]. I show that in the primary and secondary auditory cortex, sound evoked down-state is responsible for shutting down sensory information processing for a brief period of time during SWS. I found that transient acoustic stimuli in auditory cortex initiates large inward currents substantially decreased neural firing and diminished cortical oscillations similar to spontaneously occurring down-states. Processing of a second stimulus arriving during this interval is impaired compared to wakefulness. Down-state was previously thought to exist only as a phase of the slow sleep oscillation (SO) which may modulate sensory responses [123], in contrast I show that acoustic stimulation can reliably and precisely modulate cortical oscillatory state in natural SWS. This finding is compatible with the idea that the down-state, which spreads over large cortical areas [124] in an acoustic environment may serve as a sleep protecting mechanism [91] and the origin of the down-state initiation may be located in the auditory cortex.

1.1. The auditory thalamocortical system

Above the brain stem ascending auditory information spreads towards the thalamus and auditory cortex (AC). Both medial geniculate body (MGB) of the thalamus and the AC show partial tonotopic organization [125], meaning neither the whole MGB nor the whole AC are represented in a simple form of a tonotopic map and have different subregions (Figure 4.1.). An important part of the afferent auditory system, where the ascending information is conveyed, is the thalamocortical pathway.

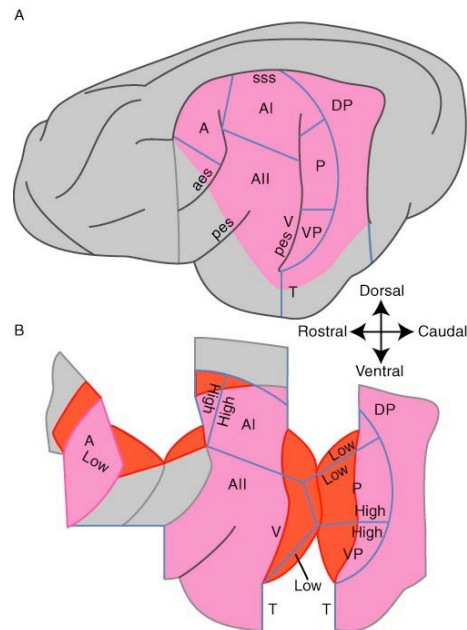


Figure 4.1. Auditory cortical fields on the temporal cortex of the cat [125]. (A) Lateral view. (B) Lateral view that is unfolded to show the part of the field that are normally hidden within the sulci (orange shading), as well as the high- and low-frequency limits of the tonotopic fields.

The brain itself can condition its own sensory input by controlling all receptors and nuclei through the efferent system which important part is the corticothalamic pathway. By using this feedback pathway, the complex processing circuit may be completed through a functional ‘closed-loop’ system [126].

Corticocortical connections between the different auditory cortical areas have particular role in the incoming signal processing. However, we have no clear view so far about how corticocortical connections influence AC function. The detailed description of AC follows later.

The thalamus responds first to external sound stimuli; however the thalamus and the cortex are simultaneously active giving the opportunity for both the corticothalamic and/or cortico-colliculo-thalamic feedback to shape responses at each level [127-132].

We do not completely understand how the brain processes incoming sensory information, however it is widely accepted that neural networks involved, can change depending on the information they receive in different state of the sleep-wake cycle.

1.2. The auditory thalamocortical loop

The simplified thalamocortical loop includes three major components: (1) the excitatory thalamocortical cells (TC), the excitatory corticothalamic cells (CT) and the inhibitory cells of the thalamic reticular nucleus (nRT) (Figure 4.2.). There is a specific well-defined auditory zone within the reticular nucleus (RE ventroposterior zone) that is connected to other thalamic regions and to the AC. The RE receives its input from the MGB, most likely via a collateral of the axons projecting to the AC, however the existence of such a collateral has not been proven for the auditory system but only for the somatosensory [133]. The RE also receives input from descending pathways of the AC via a collateral of the axons terminating in the MGB [133]. Thus, nRT cells receive excitatory inputs from both the TC cells which project into the cortex and the CT cells which target is the thalamus [134]. The primary target of ventroposterior RE cells is the MGB. The RE has a strategic position allowing a feedback control, which is GABAergic [133]. The feedback effect is modulated through the thalamocortical and corticothalamic connections.

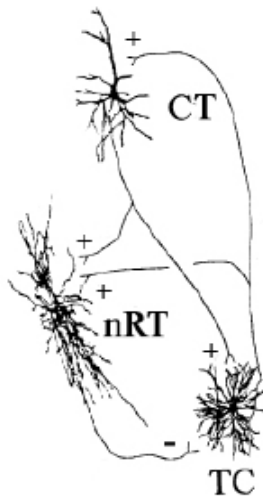


Figure 4.2. The thalamocortical loop. The CT cell sends excitatory synapses to TC and nRT cells. The CT cells excite CT and nRT cells. nRT neurons inhibit TC cells. TC: thalamocortical, CT: corticothalamic; nRT: thalamic reticular cell [113].

1.3. The auditory thalamocortical pathway

The auditory thalamus receives its main input from the central nucleus of the Inferior Colliculus (IC), passes on towards the laminated ventral division of the MGB then terminate at most of the tonotopic cortical fields. Another pathway begins in the dorsal cortex of the colliculus, passes through the dorsal part of the MGB and projects mainly to cortical field AII. This pathway connects less tonotopic areas. A third pathway called polysensory pathway begins in the external and dorsal nuclei of the colliculus, continues to the medial part of the geniculate and terminates almost all the cortical fields. The MGB has vital roles in signal transformation toward the cortex [135, 136], attentional modulation [137] and intracortical communication [138, 139]. The various auditory cortical areas receive extrathalamic ascending inputs from the locus coeruleus (noradrenergic projection), the nuclei of the raphe (serotonergic), the basal forebrain (cholinergic), the ventromedial tegmentum (dopaminergic), the hypothalamus (histaminergic) and the brachium of the inferior colliculus [140]. Projections of the thalamic nuclei are highly specific, even in non-primary areas or in regions devoid of tonotopic organization [141, 142]. Many details are not mentioned in this summary, however, one important point is evident: the auditory system includes many parallel pathways and therefore designed for parallel processing.

Huang et al. distinguishes 3 types of auditory thalamocortical projections from a laminar perspective, and these patterns are both nucleus and area specific [143]. Type 1 projects mainly into layer III-IV with little input to layer I, and it arises from the ventral division and the dorsal superficial, dorsal and suprageniculate nuclei of the dorsal division of MGB. Type 2 has considerable input to layer I and less to layers III-IV, arising from the dorsal division nuclei mainly, especially from the caudal dorsal and deep dorsal nuclei. Type 3 arising from the medial MGB and gives input to layers I, III-IV and VI.

These laminar patterns suggest different redistribution of ascending thalamic information. Layer I and II cells, those are concerned with mainly intrinsic connections (horizontal cells) receive different thalamic input than layer III-IV cells. Layer V and VI cells, which are mainly corticofugal, receive less type I thalamic projections. The type 2 pattern includes many non-primary areas and has a much wider laminar distribution than the type 1 pattern. The type 3 projection is more variable, giving input to almost all the

auditory cortical layers. These different patterns might underlie essential system features, i.e. precise timing of thalamocortical information flow [143].

1.4. The auditory corticofugal pathway

The auditory system has a conspicuous efferent component that makes it unique. The thalamus receives input from the cortex via corticothalamic fibers. Inactivating or cooling the cortex strongly affects thalamic excitability, RF structure and oscillations [144]. According to the classic theory [145], the corticothalamic system is reciprocal to thalamic input. However, recent studies proved it was an oversimplification [146, 147] because some thalamic nuclei do not receive input from their cortical targets and some cortical regions project beyond thalamic regions that terminate in them. The non-reciprocity of these pathways suggests functional asymmetry and existence of multiple, independent corticothalamic pathways [146, 147]. It has also been proven that the corticothalamic projections are among the larger connection systems in the brain [147], and the number of corticothalamic connections exceeds the thalamocorticals [146]. Thus, corticofugal connections play a complementary, and perhaps even an executive, role in the control of sub-cortical excitability [148].

Two corticofugal systems have been described: the first is connected to the MGB, the other one with a wider distribution, is projected towards the IC, the non auditory thalamic nuclei, the striatum and the lateral pontine region [149]. Auditory corticofugal pathways compose a descending pathway innervates the MGB monosynaptically [146], the IC [150], the CN [151], and the olivo-cochlear nucleus [152]. Only a few data have been published about the effects of the AC on the MGB cell activities [153]. Sauerland et al. reported the existence of presynaptic excitability increase in this nucleus [154], a fact that might play significant role in answering the question how the efferent pathway is capable to modulate the incoming information that tends toward the AC [126].

The classic view stresses the importance of layer VI origin of the corticothalamic pathway. Others found the deepest one third of layer V equally involved, with smaller discontinuous projections from superficial layer V [155, 156]. The middle parts of layer V projects to the IC. It might have a complementary corticothalamic role.

1.5. The auditory corticocortical pathways

The corticocortical system consists of pathways connecting neurons within a specific subunit area (intrinsic), or 2 different areas (extrinsic).

The major input (>50%) to all auditory cortical areas arises from intrinsic sources [141], meaning that cells in each cortical sub-areas prefer projecting within a specific part. This fact strongly suggest that the functional profile of cortical neurons is shaped largely by local and remote cortical influences and that the impact of thalamic pathways is comparatively much smaller and perhaps more limited than it was thought [141]. The extrinsic corticocortical connections link familial areal groups of which the individual areas are distinguished by the strength and patterns of their individual principal inputs [141]. Thus, tonotopic, non-tonotopic, multisensory and limbic areas have their own preferential connections.

Intrinsic input arose from all layers except layer I, and extrinsic input had unique, area-specific infragranular and supragranular origins. The many areal and laminar sources of input may contribute to the complexity of physiological responses in AC and suggest that many projections of modest size converge within each area rather than a simpler area-to-area serial or hierarchical pattern of corticocortical connectivity [141].

1.6. The cat auditory cortex (AC)

The cat AC is located on the brain convexity, thus it is easier to investigate it than that of other animals ACs (i.e. monkeys) [157]. It has tonotopic, non-tonotopic, multisensory and limbic areas (Figure 4.3.). Tonotopic areas are the primary auditory cortex (AI), the anterior auditory field (AAF), the posterior auditory cortex (P), the ventral posterior auditory area (VP) and the ventral auditory area (Ve). The non-tonotopic areas include the secondary auditory cortex (AII), the anterior ectosylvian field (AES) and the dorsal auditory zone (DZ). Multisensory areas are the dorsal part of the posterior ectosylvian gyrus (ED), the intermediate part of the posterior ectosylvian gyrus (EI) and the ventral part of the same gyrus (EV), while limbic areas are the temporal (Te) and insular (In) cortices [144]. Hereafter, this thesis concentrates on the AI and AII areas.

The AI area is located on the dorsal part of the gyrus ectosylvius which is positioned laterally. AI, the primary auditory cortex is tonotopically organized: the base of the cochlea (high frequencies) is represented anteriorly, while the apex (low frequencies) is represented posterior [158, 159]. This fact was confirmed by Lakatos et al. as well [157]. The cat AC has a classical cytoarchitecture formed by 6 layers like most of the other cortical areas [160]. The lamination of the AC is related to the topography of the interconnections of the AC areas as it was mentioned in previous chapters.

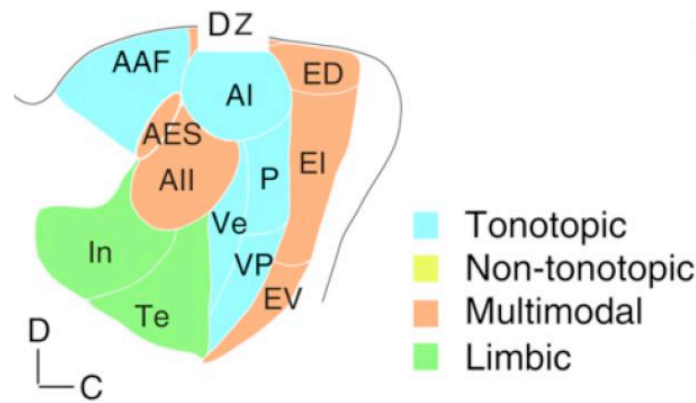


Figure 4.3. Areas of the cat auditory cortex [161]

The AII and AI can be separated by cytoarchitectonic features: in the layer III of AII, pyramidal cell density increases significantly, meanwhile layer V is characterized by large pyramidal cells. Proving the tonotopic organization of this area is pending however more and more authors describe facts that underpin this theory [162-164]. Contrarily, others report convincing data about the non-tonotopical organization of AII [144]. The AII is considered as a subsequent node in the information processing chain, after the AI. The PAF and P are usually mentioned as association areas. It seems these areas are tonotopically organized, however early unit activity of the signal recorded by microelectrodes show increased latency and less correlation with time of the applied stimuli. Tuning curves of AII cells are broader than of AI cells [165, 166]. Several studies refer to these areas as components required for later cognitive information processing. Connecting pathways between AI and AII show tonotopic arrangement.

The principal inhibitory neurotransmitter in the cortex is γ -aminobutyric acid (GABA) as it known from the cortical supra-granular zone in AI. Noradrenalin has also been reported as an inhibitor but it has a slower time course than GABA. Small number of cholinergic cortical neurons can be found in the basal nuclei of the basal forebrain and they project diffusely to different areas of the neocortex [167-169]. The cholinergic actions on AI have a long latency and a long duration of several minutes [126]. The excitatory efferent system is mainly glutamatergic [170].

1.7. The Auditory Evoked Potential (AEP)

The event related potentials (ERP) reflect potential changes that are generated, in response to physical events (i.e. commencing a movement) or various sensory stimuli (i.e. sound, light, tactile), in the brain structure corresponding to the event or stimuli. We distinguish between acoustic, visual, somatosensory, olfactory, gustatory, vestibular and

pain induced ERPs in the sensory division of ERP. The deflection in EEG, in response to acoustic stimulus, is called the Auditory Evoked Potential (AEP). According to the classic theory, the main feature of ERPs is the strict time-lock between the evoking stimuli and the neuronal background activity accountable for generating the ERP [133]. The time-lock is a congenital feature of ERPs since EEG components that are not time-locked to the given stimuli cease with averaging. In my dissertation I discuss the features of AEPs only.

ERPs consist of positive and negative deflections in the EEG signal, which follow each other. The labels given to the peaks of an ERP waveform often include descriptors of polarity and latency. According to this logic, for example P300 refers to a positive deflection with a modal peak latency of 300 ms. The ERP waves, as well as the spontaneous EEG waves, are generated on neuronal population by summation of excitatory (EPSP) and inhibitory postsynaptic potentials (IPSP). Those waves spread from their place of origin to surrounding tissue via volume conducting. Waves corresponding to a specified generator are called components. We distinguish between exogenous and endogenous ERP elements according to their functional features [133]. The amplitude and latency of exogenous components rely on the physical parameters of applied stimuli to a great extent, whereas the endogenic components rather show relation to cognitive processes. Researchers used to distinguish mesogenic components which are influenced by both the above mentioned factors however this terminology is not in use anymore. Dividing the AEPs into exogenous and endogenous components also splits acoustic ERPs into distinct groups, in which waves are distinguished by their latency.

The peak latency of the first surface positive component (P_1) of AEPs in waking cats is 10.5-13 ms (Figure 4.4.). This early component displays the so called 'phase reversal' in the deep layers of the cortex but the peak of the deep negative wave occurs 2 ms earlier than that of the surface positive one [171, 172]. In wakefulness, the second surface positive component (P_2), which typical latency is 20-25ms, is separated from the first by a negative peak (Figure 4.4.). These 2 positive waves are considered independent. A negative wave with 45-70 ms peak-latency is a typical late component of the AEP recorded from surface (Figure 4.4.). This N_1 wave is followed by a positive wave of low amplitude (P_3), with latency depending on the duration of the N_1 component and showing considerable fluctuation. This description refers to AEPs, which are recorded from the surface of the median ectosylvian gyrus, however shape and latency of AEP components may differ from the above mentioned if they are recorded from other parts of the same

gyrus [173]. The shape and timing of different components of the brain surface recorded AEPs are vigilance state dependent, as well as the laminar profile of the AEP [120, 171, 172, 174].

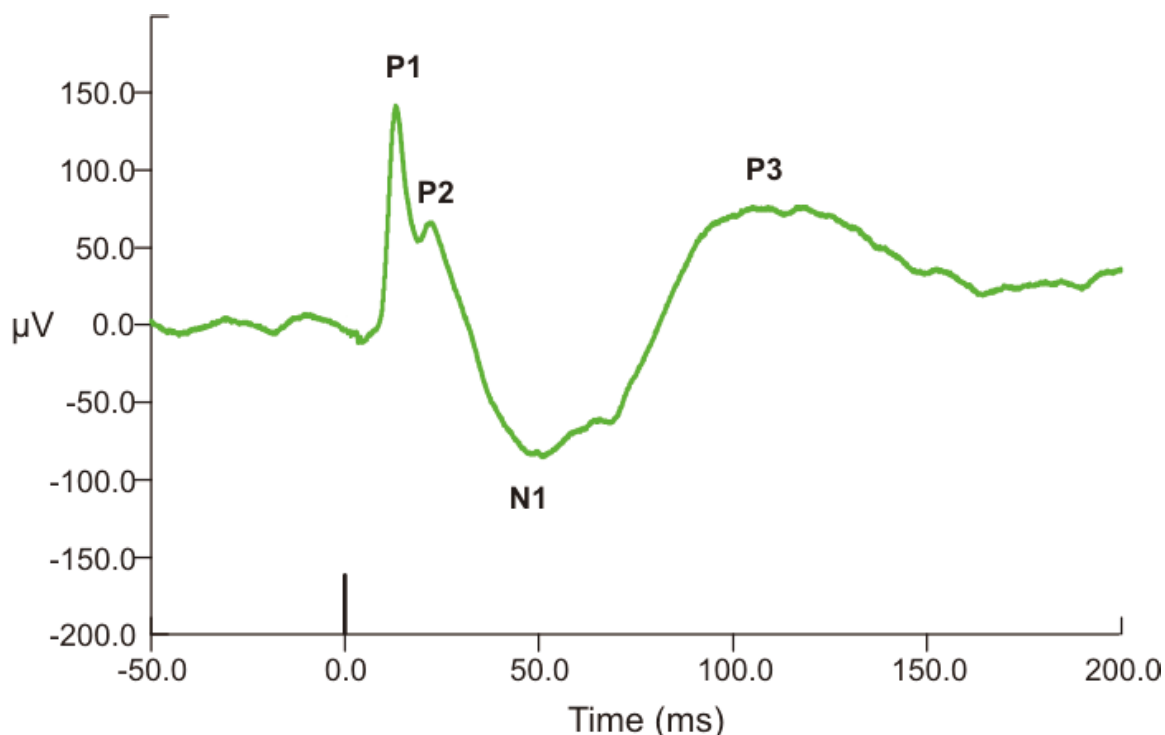


Figure 4.4. Shape and latencies of the main components of the auditory evoked potential (AEP) recorded from the median ectosylvian gyrus of an alert cat. The click stimulus was presented at 0 ms.

Matching the AEP components of cats and humans is not done completely, and achievement of this goal is not entirely possible because of the anatomical diversities of ACs. Nevertheless, some have published remarkable results on this topic [157]. We might use AEP data deriving from cat studies to investigate the background of cognitive processes but we must take into consideration the differences between human and cat auditory cortices. Invasive investigations of generator structures could give us valuable data referring to the neural processes producing the ERPs. This is necessary in order to understand the background of different sensory and cognitive phenomena.

1.8. Sleep states and related oscillations

Sleep is a process during which significant physiological changes can be observed in humans and animals [175] affecting both the peripheral and the central nervous system [176]. Sleep seems to be one of the last complex integrated behaviors for which the adaptive advantage remains unknown. There is, however, no shortage of theories

explaining the functions of sleep: energy conservation and protection against energetic exhaustion, restoration of tissular integrity, neuronal plasticity, processing of memory traces. The situation becomes more complicated because of the presence of two special types of sleep (Rapid Eye Movement (REM) and Slow Wave Sleep (SWS)), which may have different and independent functions [177].

The incoming information processing mode of the brain depends on its physiological state. Wakefulness, sleep stages I-IV and paradoxical sleep states characterize the human sleep-wake cycle, however in animals, wakefulness, rapid-eye-movement (REM) and slow-wave-sleep (SWS) states describe the natural cycle.

REM sleep is commonly identified with dreaming. Its timing is linked to circadian rhythm and body temperature. During this stage, the activity of the cortical neurons is quite similar to that during waking hours [114]; for this reason, the phenomenon is often called paradoxical sleep (PS). Electroencephalography (EEG) shows arousal and similarities to stage 1 in humans, at times including beta waves too. Motor neurons are not stimulated and thus the body's muscles do not move (REM atonia), except for sudden clonic twitches. Lack of such REM atonia causes REM Behavior disorder; sufferers act out the movements occurring in their dreams. In hippocampus theta oscillation can be observed. If REM sleep is repeatedly interrupted, the subject will make up for it with longer REM sleep at the next opportunity. Acute REM sleep deprivation can improve certain types of depression. Most antidepressants selectively inhibit REM sleep.

We can distinguish between wakefulness, SWS and REM sleep states based on their different electroencephalographic (EEG), electromyographic (EMG) and electrooculogram (EOG) signs. Tonic muscle atonia, sudden eye movements and increased hippocampal theta (4-6 Hz) activity [178] are typical features of REM, while muscle activity in wakefulness is characterized by periodic contractions. SWS can be described with oscillations in the slow (<1Hz) and delta (1-4 Hz) frequency. Slow oscillation (SO) groups delta waves as it is known from intracellular studies on cats [49, 179]. The active phase of the SO, or up-state is characterized by a negative Local Field Potential (LFP) deflection and the silent phase, or down-state as a positive LFP deflection in the deep of the cortex (Figure 4.5.) [180]. In the up-state, the majority of the cortical neurons are depolarized, showing increased gamma oscillations [181] and action potentials, whereas in the down-state most of the neurons are relatively hyperpolarized with decreased gamma oscillations and firing activity. In contrary to SWS, local field

potential shows low-amplitude fast activities with increased power in fast frequencies (15-75 Hz) during wakefulness and REM (Figure 4.5.) [180].

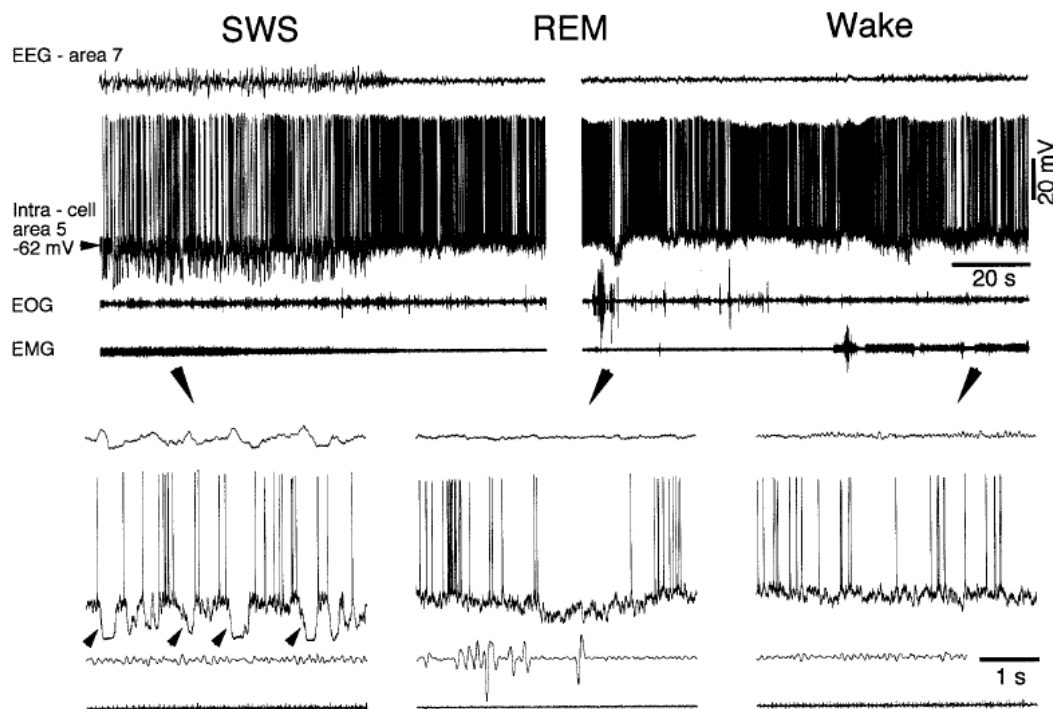


Figure 4.5. Cortical intracellular correlates of natural SWS, REM and waking states. Parts indicated by arrows are expanded below (arrows). Note cyclic hyperpolarizations in SWS and diminished firing rate during ocular saccade in REM sleep [182].

1.9. The slow oscillation (SO)

In 1993 Mircea Steriade and his colleagues described a slow (<1 Hz) oscillation in the membrane potential of intracellularly recorded neocortical and thalamic neurons and proposed that this oscillation observed in anesthetized and naturally sleeping cats is the emergent activity of a synchronized network [49]. Steriade and his colleagues showed with intracellular recordings that both in ketamine-xylazine (KX) anesthesia and natural SWS the cortical neurons produce rhythmic hyperpolarization and depolarization periods [49, 112, 179, 183-185]. During EEG deep positivity (down-state), cortical neurons remain in hyperpolarized, silent state for a few hundred milliseconds, while during EEG deep negativity (up-state) cortical neurons shift to active states (depolarization period), reveal barrages of synaptic events and fire action potentials (Figure 4.5.) [186].

In vivo and in vitro animal experiments as well as computational models [22] revealed that synaptic and non-synaptic network activities and intrinsic membrane currents are involved in the production of slow oscillation. Different studies assumed intracortical

origin for SO since it can be recorded from neocortex after thalamic lesion [179] but not after the disruption of corticocortical connections [187] and it is absent in the thalamus of decorticated cats [188]. The SO activity could be disrupted by the sectioning of intracortical pathways, though it was restored a few hours later. The intracortical origin is supported by the observation that up-state as well as down-state appears in the cortex earlier than in the thalamus [189-191].

Thalamic and cortical neurons showed phase relationship that is restricted to a narrow time window during SWS [192]. It was revealed that the onsets of down-states are more synchronized than the onsets of up-states. Moreover, the onsets of down-states showed no change in latency bias in regard to the cell type or its location [124]. Intracellular studies on anesthetized and non-anesthetized cats have shown that the down-state of the slow oscillation is associated with disfacilitation, a temporal absence of synaptic activity in all cortical and thalamic neurons [182, 188].

Many different basic mechanisms have been proposed as possible explanation of the background of SO. The most important are discussed.

Spike-independent release of transmitter vesicles, which are regulated at the single synapse level, cause mini Postsynaptic Potentials. Excitatory Postsynaptic Potentials (EPSP) can summate and activate persistent sodium currents during the down-states of SO. Those sodium currents depolarize cortical pyramidal cell membranes that might be sufficient to generate spikes, which triggers an up-state that propagates through the entire network [193, 194].

Sanchez-Vives and her colleagues revealed that membrane potential of cells in a cortical slice preparation can oscillate between up- and down-states in the frequency range of SO [195, 196]. The activity initiated from the layer V in her experiments and propagated over the entire slice. However, the extracellular concentration of K^+ was maintained relatively high (3.5 mM). Further increase in K^+ level might depolarize more neurons which can reach the firing threshold. Summed high amplitude EPSPs might recruit postsynaptic neurons into an up- state. Nevertheless, the slice preparation limits the universality of Sanchez-Vives' conception about the layer V origin of SO, since crucial connections of neurons which might have key role in up- and down-state ignition and/or termination can not be put in the slice.

Our group measured the action potentials of single cells and synaptic/trans-membrane activity of cell populations in different layers of human frontal cortex during deep non-REM sleep [197, 198]. We concluded that unlike in animals [196, 199], the cortical

generators of SO, as well as the associated high frequency oscillations are all primarily localized in the supragranular layers and the onset of the up-state is not layer specific. Furthermore, in humans the firing rate in the up-state was a small fraction of what has generally been observed in animals [114, 200, 201].

Crunelli found that the dialogue between 3 cardinal oscillators explains the underlying mechanisms of SO [202]. These generators are the following: the primarily, but not necessarily exclusively, synaptically based cortical oscillator (with a layer 4 thalamocortical input and a layer 5/6 corticofugal output) and two intrinsic, conditional thalamic oscillators, the thalamocortical and NRT neurons. He published that each of these 3 oscillators is capable of producing its own slow oscillation, however the full EEG manifestation of the slow rhythm requires the essential dynamic tuning provided by their complex synaptic interactions [202].

Current source density (CSD) analysis [203] was used to localize the generators of the low frequency (<1 Hz) components of the artificial, anesthesia induced SO to the middle cortical layers [204, 205]. In contrast, the fast (30-40 Hz) components are more distributed, composed of “alternating microsinks and microsources” along the whole cortical depth [204] in cats.

Toward the end of up-states the synaptic conductance diminishes progressively. Thus, it is very likely that up-state termination is accompanied by a progressive run-down of synaptic activity. Intrinsic mechanisms (build-up of a slow K^+ conductance in single cells, reducing their firing) and/or synaptic mechanism (build-up of a depressed state of excitatory synapses) might play role in active state termination [206]. Either of these mechanisms may potentially explain refractoriness of the active states of slow-wave sleep found in slices [196]. In contrast with these results, the active state is associated with prolonged depolarizing states, eventually lasting for the duration of the active state in *in vivo* recordings. Thus, refractoriness of an active state seems to be present in *in vitro* preparation only and could be attributed to the property of reduced network. *In vivo* study revealed surprisingly high synchrony of active states termination [124] that implies the existence of a network mechanism which switches activity to silence. While down-states are relatively short *in vivo* (few hundred ms), their duration can be tens of seconds in relatively small cortical slabs [194]. This suggests that the period and regularity of slow-wave sleep oscillations might depend on the network size.

Emerging evidences suggest that non-REM period in humans, especially SO underlies restorative sleep functions and serve memory consolidation [207-209] via ensemble

reactivation [210-213] and synaptic strength normalization [209]. The basic substrates of these processes are identified as theta/gamma interactions, spindle and numerous other, including gamma frequency band oscillations linked to the up-state of the slow oscillation. Findings of coalescing neuronal rhythms orchestrated by the cortical slow oscillation also strengthen the role of sleep in memory consolidation [190, 207, 214]. It has been proposed that synaptic plasticity associated with slow and delta oscillations could contribute to the consolidation of memory traces acquired during wakefulness [113]. Based on the analysis of multiple extracellular recordings of slow oscillations during natural sleep, it was suggested that fast oscillations during active states of slow-wave sleep could reflect recalled events experienced previously; these events are "imprinted" in the network via synchronized network events that appear as slow-wave complexes in the EEG [180].

It is well known, that sleep modulates epileptic activity [215]. Slow wave sleep (SWS) enhances paroxysmal activity and nocturnal seizures are often observed in patients with frontal lobe epilepsy. In animal models, extensive intra- and extracellular observations revealed, that seizures also often develop from the cortical slow oscillation (SO). In these models, the epileptiform activity and seizures consist of several well defined electrical patterns of intracortical events, such as spike-wave, polyspike-wave complexes and fast runs [191]. Similar building blocks were found in the human disease too with scalp and intracranial field potential recordings.

Destexhe found that slow oscillation is significantly different from REM sleep and wake state in its spatiotemporal properties [180]. In cats he experienced that slow wave sleep is correlated over large cortical distances (7 mm), but not during REM or wakefulness.

Several physiological consequences can be drawn from these findings. One of them indicates that recurrent fast oscillations reflect recalled events experienced previously, which are imprinted in the system via synchronized networks that appear as slow-wave complexes [180]. Another interpretation of the slow oscillations is a fluctuation in gross cortical excitability [216]. This conclusion is derived from the finding that the phase of slow oscillation was robustly correlated with the magnitude of faster EEG oscillation, as well as with the occurrence of interictal epileptiform events and K-complexes in humans [191]. It could mean that slow oscillations predispose brain to epileptic activity.

My aim was to investigate how information processing in the AC of cats alters as a function of change in vigilance level. Special emphasis was given to SO phase because

the classic theory by Steriade et al. stressed the importance of thalamus as a switch that is in off mode during the SO phase [112-114]. According to their theory the information transfer is blocked at the thalamic level, since the thalamocortical neurons are steadily hyperpolarized in SWS (in contrary to waking where thalamocortical cells' membranes are tonically depolarized), and afferent stimuli do not reliably evoke an EPSP that reaches firing threshold [113]. So, 'the thalamic gates are closed for signals from the outside world during SWS, because of obliteration of synaptic transmission in thalamocortical neurons, the intracortical dialog and responsiveness of cortical neurons to callosal volleys are maintained and even increased during SWS' [113].

It was also published that KX is an appropriate anesthetic that reproduces the whole repertoire of brain rhythms what can be seen during the natural sleep of the cat [217]. I investigated how does the mode of information processing of the AC is different in natural sleep and KX anesthesia.

2. Methods

2.1. Surgical procedure and electrodes

5 cats were implanted with laminar multielectrodes (ME) (Figure 4.6.) into the primary and secondary AC. The animals' head were placed in a stereotaxic frame (Kopf) after Nembutal anesthetic was administered (40mg/kg, i.p.). Anesthesia was maintained with Nembutal during the whole length of the surgery. Body temperature was maintained at 37-38°C with a heating pad (Temperature Controller, Supertech Inc.) and respiration was monitored during the surgery with a respiratory meter (ECG Respiratory meter). Stainless steel bipolar twisted electrodes (diameter: 0.23 mm) (Fine Wire Inc, California), insulated except for 1 mm of their tips were inserted bilaterally to the dorsal hippocampus (AP:4.5; ML:4.5; DV:8.0 according to Snider and Niemer, 1961). Muscle activity was sampled with a twisted wire EMG electrode implanted in the neck muscle.

Eye movements were monitored with 2 EOG electrodes permanently implanted into the posterior part of the left and right orbital bone. Stainless steel electrodes were placed epidurally over the visual and motor cortices in order to record electrocorticogram. The reference and ground mini screws (Small Parts Inc.) were drilled into the frontal and occipital bone, respectively. Mapping the AC was carried out before the laminar ME insertion, via recording AEPs with epidural stainless steel electrodes. On one side of the cranium holes were drilled through the bone in a matrix like fashion beyond the AC. 6

stainless steel wires recorded AEPs through those holes. A 5x5 matrix (Figure 4.7.) that was made via gluing together stainless steel guiding tubes, was placed over the other AC for helping the insertion of a 24 channel laminar multielectrode [13].

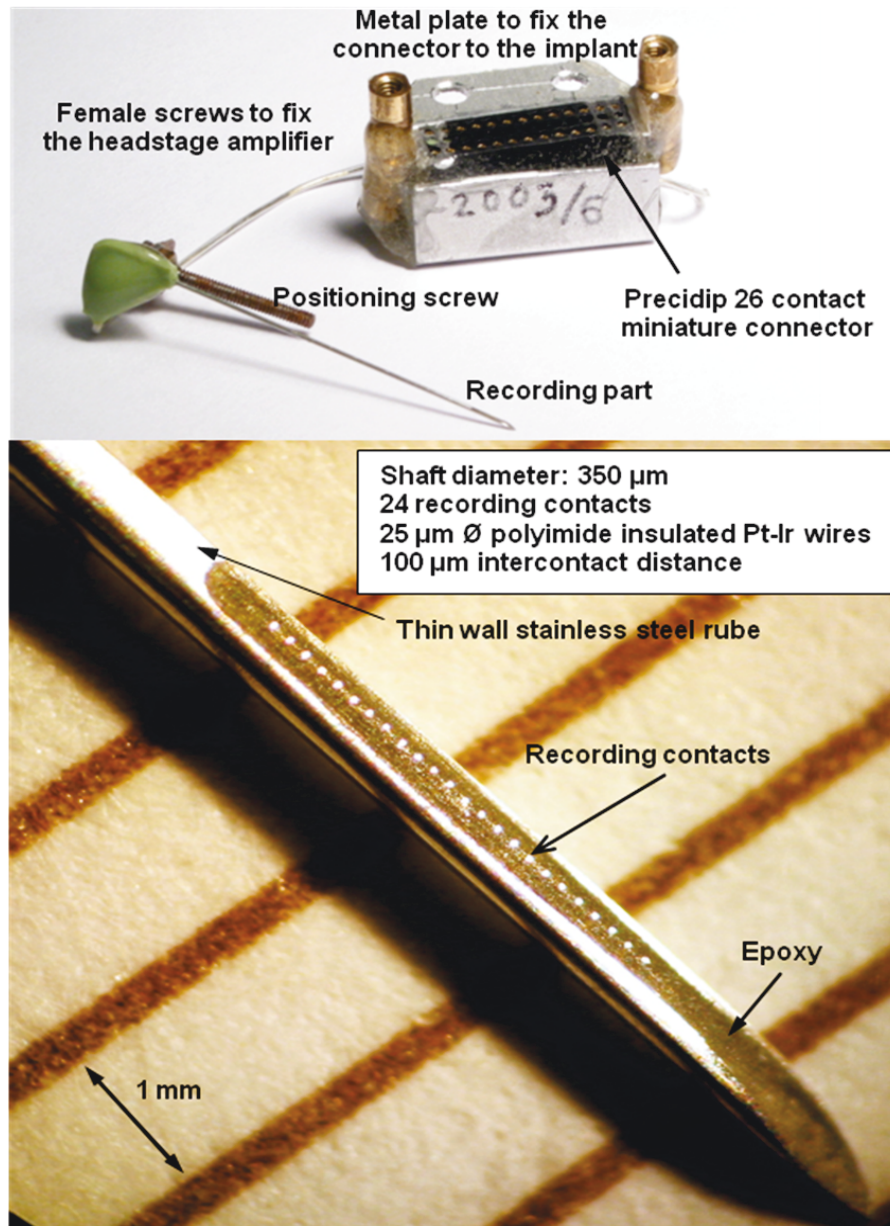


Figure 4.6. Chronically implantable stainless steel laminar multielectrode with 24 Pt-Ir recording contacts.

The AI was mapped with the aid of the 8 epidural electrodes passing through the silicon pad located on the bottom of the matrix (Figure 4.7.). The exact position of the AI was determined by the amplitude and timing of AEPs evoked by click stimuli given with the calibrated bone conductor. The laminar ME was finally inserted through the guiding tube into the AI by a homemade micromanipulator that was fixed to the electrode. At the end of the procedure all the electrode contacts were in the cortex below each other in a

line perpendicular to the surface. The wire electrodes were crimped to a miniature Winchester socket. Dental acrylic (Duracryl Plus, SpofaDental, Frankfurt am Main, Germany) was used to fill up frontal sinuses, to fix the electrodes and the socket to the skull and to create chambers for the bone conductor.

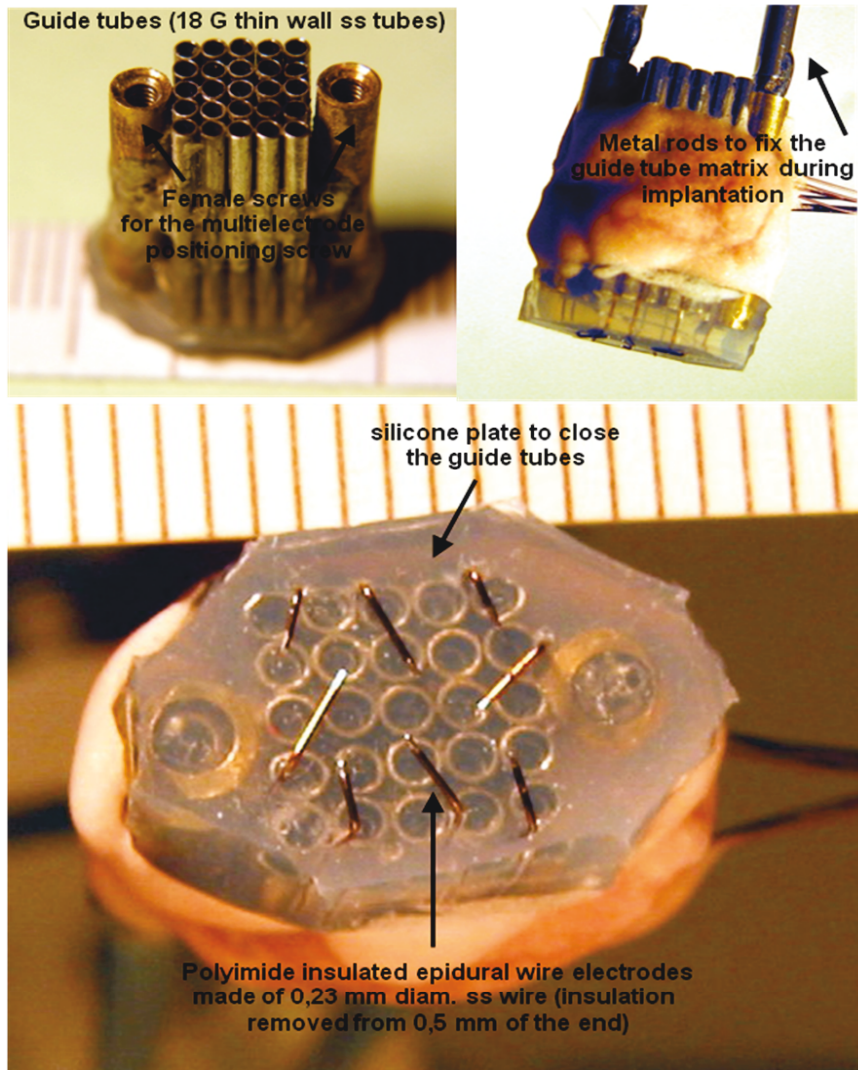


Figure 4.7. A 5x5 guide tube matrix for chronic implantation.

The experiments were begun 5-6 days after surgery. The animals were placed in a 0.8x0.7m experimental cage, being in a soundproof chamber. Their activity was video monitored by using a conventional camera system. The animals got accustomed to the cage since they were regularly fed there and also spent considerable amount of time sleeping in that environment.

Besides recording the natural sleep-wake sessions, 3 cats were also anesthetized with ketamine-xylazine (KX, 15ml/kg ketamine and 2.5 mg/kg xylazine, i.p.), which is a reliable SO inducing substance. The animal experiments were done according to Animal

Care Regulations of the Institute of Psychology of the Hungarian Academy of Sciences, approved by the National Board on Animal Health (Nr. 22.1/77/001/2010).

2.2. Acoustic stimulation

To assess the effect of vigilance level change and KX anesthesia related modulation of cortical sensory processing, repetitive single and double auditory click stimuli were delivered. Single and double sound clicks (0.1 ms long, 1-3 1/sec, random and rhythmic, 20-80dB SPL) were delivered via a bone conductor (Oticon A/S, Copenhagen, Denmark, Type 10380) attached to the skull covering the frontal sinus to maintain the constant intensity acoustic stimulation in the sleeping animal [218]. Acoustic stimuli were generated by Tucker-Davis Technologies (TDT, Gainesville, FL) System III hardware and software. Click stimuli were presented via bone conductor fixed to the head of the animal and were recorded on the 24th channel.

The animals were habituated to the clicks, until they were able to fall asleep with the ongoing auditory stimulation.

2.3. Data acquisition

In order to maintain attentive vigilance level in wakefulness, recordings were made during the period when the animals were waiting for alimentation. After having food 'ad libitum', the animals usually initiated a sleep session. Depending on the subject, 1-5 complete sleep cycles were detected in one experimental session.

To reliably assess the vigilance level at the time of offline data analysis, neck muscle (EMG), eye movement (EOG), macroscopic auditory cortical (EEG), and hippocampal (Hc) activities were recorded. The Local Field Potentials (LFP) and Multiple Unit Activities (MUA) that were generated in different layers of the AC were recorded with a 24 channel multisite probe. It allowed us to reveal the laminar profile of the auditory cortical activities in different vigilance level.

LFP, EEG, EMG, EOG, Hc recordings after amplification (gain: 5000) and filtering (0.1Hz-500Hz, 24 dB/decade) were sampled at 2kHz/channel rate with 16bit precision, while MUA (band pass filter: 300Hz-5000Hz, 24dB/oct) were sampled at 20kHz/channel rate with 12bit precision (LabView, National Instruments, Austin, TX), and stored on hard drive for off-line analysis. The low noise pre- and main amplifiers, necessary for good quality signal recording, were designed and built in house [219].

2.4. Data analysis

The recorded continuous file format (.cnt) was epoched by using the exact timing of the given sound stimuli as trigger. An epoch contains each channel neural activity from a few ms before to some hundred ms after the stimuli time. This file format is called .eeg. The grand average of each epoch of one recorded file is called the averaged file (.avg). Artifact free epochs were analyzed with Matlab (The MathWorks, Natick, MA) based codes and a commercial software (NeuroScan 4.3 Edit Compumedics, El Paso, TX). The Neuroscan software helped me in filtering, voltage thresholding, epoching, baselining, averaging and smoothing the LFP and MUA signals. A Matlab code (Multiple Channel Frequency Analyzer, MCFA) based on the EEGLAB open-source software [220] was written to compute multichannel time-frequency spectra of selected epochs with Fast-Fourier or Wavelet analysis [221], and also made it possible to run different time-frequency related statistical functions. Up-state and down-state detection, firing frequency of cells, Peri- and Post-Stimulus Time Histograms (PSTH) in different phases of the sleep-wake cycle was carried out with a novel Matlab based multifunctional software (Wave Solution) that has been developed by Richárd Csercsa and Andor Magony. Spontaneous recordings were analyzed with the NeuroScan, MCFA and Wave Solution as well.

2.5. Current Source Density (CSD) analysis

CSD is the local summation of a neuron population's transmembrane currents that gives the spatiotemporal pattern of current sinks (positive charges flowing across the plasma membrane to the inside of the cell) and sources (out-flowing current to the extracellular space). CSD identifies synaptic/trans-membrane generators of LFP in laminated neural structures [222-224]. The physiological relevance of CSD lies in the fact that current sinks can be interpreted either as a synaptic depolarization of the membrane or a return current source while source could mean hyperpolarization (synaptic or non-synaptic) or a return current sink.

CSD was calculated as the second spatial derivative of the LFP smoothed by a spatial Hamming window [13]. The second derivative of field potential approximates the depth distribution of the current sources in laminated structures, such as the cerebral neocortex. Inhomogeneous conductivity and electrode spacing were not taken into account.

2.6. Time-frequency analysis

Spectral content (in dB) and power of the multichannel LFP as well as CSD maps were computed with the built in function of MCFA. This software provided us the possibility to run Wavelet or Fast Fourier analysis on epochs of imported files. The Wavelet/Multichannel Event Related Spectral Perturbation function calculates the event related changes of power in a given frequency and time interval while the Multichannel Inter Trial Coherence function help us to reveal coherency between epochs [220, 221].

2.7. Up- and down-state detection

The up- and down-state detection is not self-evident, so we need to apply diverse methods for disambiguation. Comparing the 3 built in state detection methods of Wave Solution (MUA, LFP gamma band power and Hilbert transform based) we have found the Hilbert transformation as the most robust and stable one. MUA method was sometimes unusable, because of the lack of large action potentials. The gamma band power method was also ambiguous sometimes, if the signal contained contaminations from movement and muscle activity [198].

Though Hilbert transform is a linear operator, it is useful for analyzing non-stationary signals by expressing frequency as a rate of change in phase, so that the frequency can vary with time. Typically multiple time-varying frequencies coexist in raw recordings, so in biological usage it is recommended to use a filter before the transformation in order to remove the irrelevant components (e.g. frequencies out of the 4-7 Hz range in case of examination of theta activity in the hippocampus). Fast Fourier Transform gives high frequency resolution, while Hilbert transform gives better temporal resolution of rapid changes in analytic state variables for frequency, phase and amplitude, since the temporal resolution of wavelets and FFT is bounded by the Nyquist criterion: the digitizing rate must be at least twice and preferably 3 times the highest component frequency [198].

The definition of the Hilbert transform is as follows:

$$\widehat{s}(t) = \mathcal{H}\{s\} = (h * s)(t) = \int_{-\infty}^{\infty} s(\tau)h(t - \tau)d\tau = \frac{1}{\pi} \int_{-\infty}^{\infty} \frac{s(\tau)}{t - \tau} d\tau.$$

where $h(t) = \frac{1}{\pi t}$

During down-state detection I first filtered the signal recorded with the desired electrode in the frequency range of the slow oscillation (0.5 – 3 Hz). Thus I get a sinus-

like signal on which we can apply the Hilbert transform that specifies the phase in every sample point. The result is a sawtooth curve with small increments of phase lag along a diagonal from the lower bound to the upper bound, and a downward fall in one step to the lower bound on reaching the upper bound. This happens once in each cycle. The valley of the sinus signal is defined as the down-state and the peak as the up-state of the slow oscillation in intracellular recordings (Figure 4.8.). In extracellular recordings the down-state is accompanied by depth positive LFP and might accompanied by surface negative LFP as it was mentioned earlier in this chapter. The reliability of down-state detection based on depth LFP profile, as well as high correlation between such detected down-states and surface intracellular recordings were proven by different groups [181, 225].

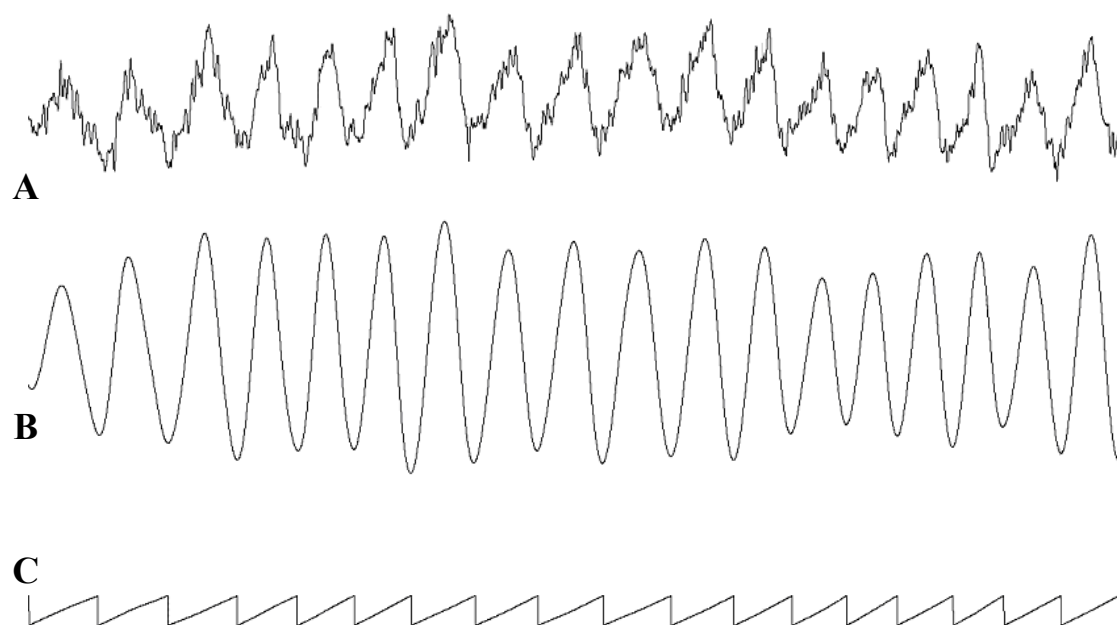


Figure 4.8. Up- and down-state detection method based on linear filtering (B) and Hilbert transformation (C) of the recorded field potential (A).

2.8. Peri or Post-Stimulus Time Histograms (PSTH)

A PSTH or Post-Stimulus Time Histogram forms a frequency histogram of events on one channel around a stimulus event on another trigger channel. One of the cells (channel) will be the reference cell or stimuli - the spikes of this cell's spike train or stimulus time will provide the reference marker. To make the PSTH we proceed as follows: line up the 2 spike trains (so that their time markers are vertically aligned); for each spike in the reference spike train center a window broken into small segments of

time called bins; now examine the target spike train within the window, and increment the bins in which we find any spikes [198].

The PSTH thus shows a count of the spikes of the target cell at specific time delays with respect to the spikes of the reference cell or stimulus. The time delay is given by the distance along the horizontal axis, and both "positive" and "negative" delays are recorded. Bin counts on the positive side - counts that occur after time 0 which is the window center - mean that the target cell spike came after the reference cell spike; conversely for the negative side. By the way, if we compute the PSTH using neuron A as reference and B as the target, and then compute the PSTH using B as reference and A as the target, we'll get the same result, only reversed in time (i.e., the horizontal axis). PSTHs give some measure of the firing rate or firing probability of the target neuron around the time that the reference neuron fires or around stimuli time. Therefore, the PSTH provides some indication of the dependence, or lack thereof. If, for instance, the output of neuron A is completely unrelated to neuron B, then (by definition) the spike times of A are just random instants of time from B's point of view. On the other hand, if there is a higher probability that the target cell fires immediately following the reference cell's spike (or marker), then we would see a peak in the PSTH at that time [198].

2.9. Statistical methods

Bonferroni corrected t-test was used in order to find significant difference between spontaneously occurring deep positive waves of SWS with evoked deep positive LFP in the latency range of the down-state. In this case CSD and MUA was averaged time locked to the onset of the detected down-states.

The difference of recurrence frequency of the down-states was compared in SWS and KX anesthesia by using Kruskal-Wallis ANOVA [226, 227] statistical method. This method was used to assess significant difference between percentages of evoked down-states in SWS and KX anesthesia. T-test was used to statistically compare the average durations of evoked down-states in SWS and KX anesthesia.

3. Results

Since the cortical neuronal mechanisms of altered acoustic sensory processing in natural slow wave sleep (SWS) is unknown and only limited data is available from chronic experiments in behaving animals, I investigated what kind of role does the AC play in information processing during this phase and how this function differs from those

in wakefulness and REM. Cats implanted with laminar multielectrodes were used for these experiments.

3.1. Distinguishing the different states of the natural sleep-wake cycle

Attentive wakefulness in cats was characterized by fast, low amplitude surface EEG and LFP (Figure 4.9.A.), high EMG and EOG, desynchronized Hc activity with occasional theta bursts linked to eye and head movements and explorative behavior. In quiescent wakefulness, the cats were sitting with eyes open, infrequent head turns, rare eye movements and little exploratory behavior. Occasional frontal spindles could be observed in the slowing EEG. EOG and EMG was less dynamic, sharp wave ripple (SPW-R) activity started to appear in the Hc.

Sphinx position with eyes closed was chosen as the criteria for the earliest stage of non rapid eye movement (non-REM) sleep or light SWS. LFP (Figure 4.9.C.) and EEG become more synchronized with emerging slow oscillations interspersed with frontal EEG spindles, SPW-R appeared more frequently in the Hc, EOG and EMG became less dynamic. Deep SWS stage was characterized by curled-down position, eyes closed, slow eye movements if any, low amplitude EMG tone, frequent frontal spindles and SPW-Rs in the Hc.

Deep SWS sleep was usually followed by the REM stage. Video monitoring revealed frequent paw, whisker and tail movements, while EMG tone was virtually absent, only short and violent twitches were detected together with rapid fluctuations in the EOG traces. EEG become desynchronized, spindles and slow activity completely disappeared. Rhythmic theta replaced the SPW-R activity in the Hc as rapid eye movements appeared in the EOG. Auditory LFP also become desynchronized, dominated by fast and low amplitude oscillations, while the large deep positive waves completely disappeared.

3.2. AEPs in different states of the natural sleep-wake cycle and anesthesia

I recorded auditory stimulus evoked neural activity during the three states of the natural sleep-wake cycle and KX anesthesia (see the Method section). Repetitive click stimuli evoked LFP and MUA activities recorded from different layers of the cortex under wakefulness (Figure 4.9.A-B.) and SWS (Figure 4.9.C-D.) are shown. Evoked responses during SWS had significantly different characteristics [120, 171-174]. Click stimuli evoked an easily distinguishable positive LFP component in the deep layers that

appeared after a deep layer early negativity. MUA was absent during the time range of that deep positivity [120, 171-174].

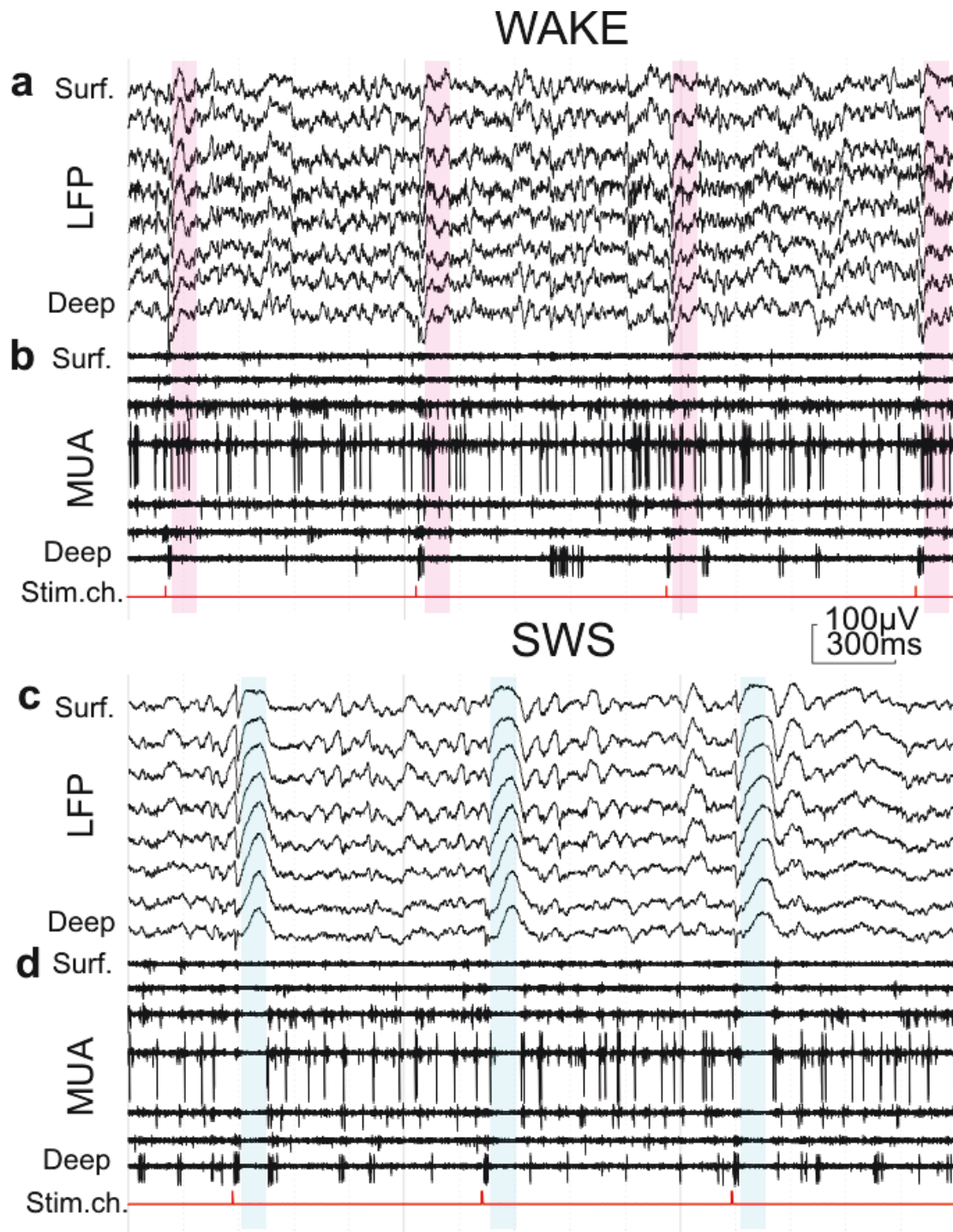


Figure 4.9. LFP and unit responses to click stimuli in wakefulness and SWS. **a.** Continuous LFP traces in the wake state from representative depths of the AC covering superficial - top traces - and deep layers - bottom traces - respectively. **b.** Simultaneously recorded unit activity. Click stimulation is indicated by the trigger line below the unit traces. **c.** LFP traces in SWS. **d.** Unit traces in SWS. Translucent red marker strips indicate the time of AEPs in wake, while blue strips indicate the time evoked down-states. Note the large deep positive wave evoked by click stimulus only in SWS.

Comparing LFP averages of evoked activities recorded from the depth of the neocortex during the three states reveal that an early and short latency exogenous negative component (11-16 ms, min: -180 μ V), analogous with the surface P₁ component but negative because of the phase reversal, is followed by the short positive P2 component (16-62 ms, max: 130 μ V) in wake and REM (Figure 4.10.). The FP average reaches the zero value around 130 ms after the click stimuli in wake and REM. The similarities in shape and timing of evoked components of these states are remarkable however there is a minor difference in both the deep early negative component and the late P2 amplitude. The deep early negativity appears with a little higher amplitude in REM.

The grand average of evoked potentials recorded during SWS has an early exogenous component (8-25 ms, max: -204 μ V), which is slightly more negative than the same component in wake or REM (Figure 4.10.). This component is followed by a long lasting positive wave (25-100 ms), which is characterized by its high amplitude (max: ~400 μ V). This component is absent in wake or REM. It is obvious even at the first sight of averaged LFPs that there is no significant difference between the deep negative initial components of the three states. The exogenous components are similar, and since the earliest component reflects the incoming information to the cortex, it seems the incoming auditory information passes into the cortex, even in SWS [120, 171-174]. The endogenous components modulate the incoming information according to the present state of the sleep-wake cycle. The mode of action, how that modulation takes place, is similar in wake and REM but different in SWS. This is why an enormous difference in the middle latency FP components is visible.

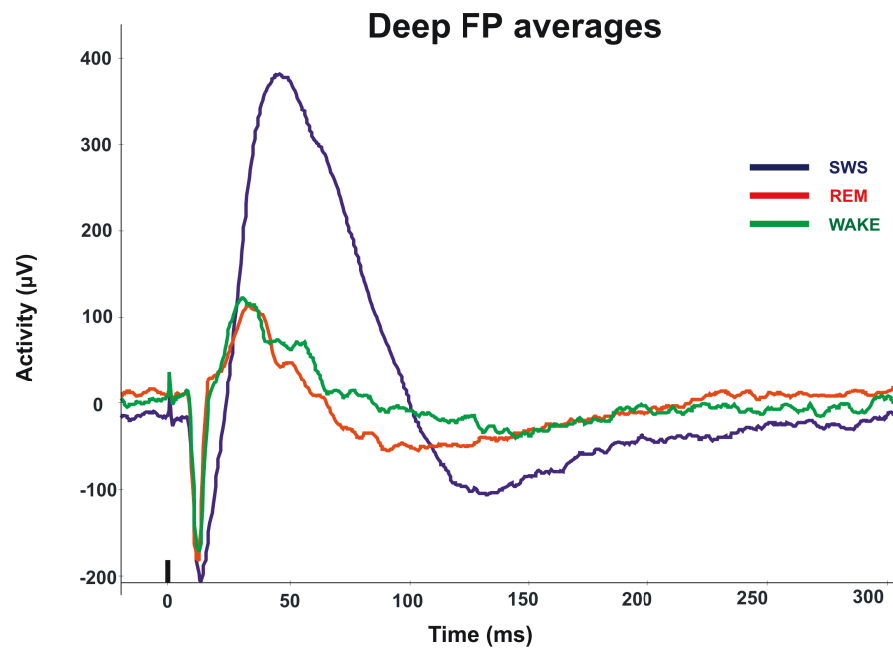


Figure 4.10. Click stimuli evoked LFP averages. The data was recorded from layer IV of the AC during SWS (blue), REM (red) and wakefulness (green). Click stimuli was given at 0 ms.

As revealed by the current source density (Figure 4.11.A.) and multiple unit activity (Figure 4.11.B.) analysis click evoked LFP started with an initial excitation peaking around 9-10 ms in layer IV followed by deeper and superficial excitation in attentive wakefulness. The initial excitation was followed by a presumably GABA-ergic fast inhibition peaking around 25-30 ms as reflected by the rapidly decreasing current sink and firing rate. LFP in the deep layers were usually small and mostly negative in the following 50-100 ms (Figure 4.10.A.; Figure 4.11.), while LFP spectrogram (Figure 4.11.E.; Figure 4.12.) showed elevated power in the gamma range from 10 ms to 100 ms post stimulus indicative of local processing.

Click evoked single sweep responses showed preserved initial excitation occasionally followed by large amplitude positive LFP deflections in the depth of the cortex during quiescent wakefulness (similar to Figure 4.9.C.). The state detection algorithm classified the stimulation related positive deflections as down-states, while down-states were detected infrequently in the absence of the clicks.

In light SWS, the evoked responses were similar to the quiescent wakefulness, except the prevalence of the sound evoked (10-30% of the clicks) and spontaneous (0.1-0.2 1/sec) down-states became more frequent. In deep SWS, virtually each click (presented at 60dB peSPL) was followed by a deep positive LFP deflection (60-100%) (Figure 4.9.C.; Figure 4.10.; Figure 4.11.C.), MUA decrement (Figure 4.9.D.; Figure 4.11.D.), a

large source in the middle layers (Figure 4.11.C.), and decreased oscillatory power (Figure 4.11.F.; Figure 4.12.) indicative of a down-state, regardless if the stimulus was rhythmic or random. The initial activation remained unchanged even in deep SWS. Comparing CSD and MUA between wake and sleep conditions, significant differences (t-test, $p < 0.001$) were found in the depth distribution of the response mostly in the 25-100 ms latency range. Similar results were obtained by comparing LFP spectral activities. The no stimulus condition yielded high amplitude spontaneous SO with down-states appearing 0.5-1/sec frequencies.

In REM sleep, we were unable to detect down-states regardless of the stimulus being switched on or off.

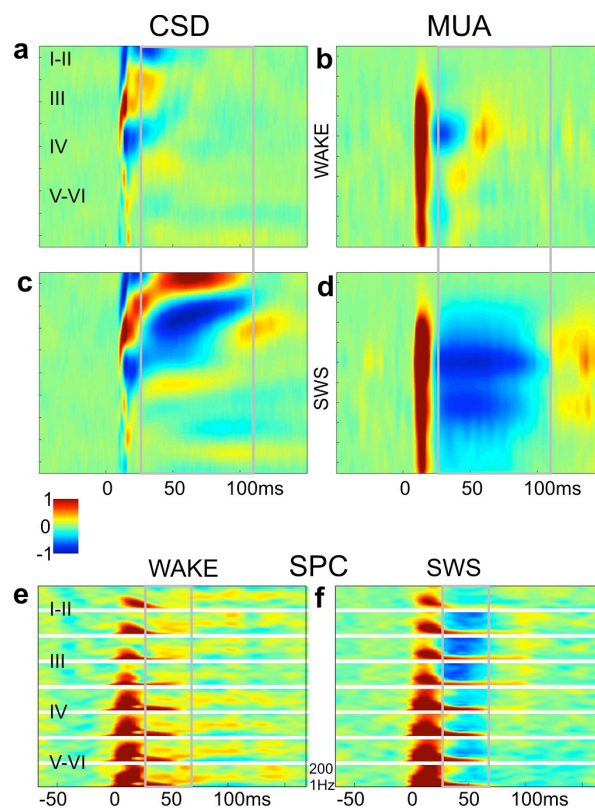


Figure 4.11. Averaged CSD, MUA and spectral responses time locked to click stimuli in wakefulness and SWS. **a**, CSD map of stimulus locked activity in wakefulness. Time: x-axis, stimulus is presented at 0 ms, cortical depth: y-axis. Sinks are depicted in red, sources in blue, arbitrary units. Laminarization is indicated by Roman numerals. **b**, Simultaneously recorded MUA map. Red indicates firing rate increase, blue decrease compared to baseline activity, arbitrary units. **c**, CSD map in SWS. **d**, Simultaneous MUA map in SWS. Note the large source and neuronal firing silence in SWS. **e**, LFP spectrogram (1-200Hz) from representative depths of the cortex in response to click stimuli in wakefulness. Each elongated rectangle represents different channel. Red indicates increased, blue decreased activity in arbitrary units compared to baseline. **f**, LFP spectrogram in response to the click in SWS. Grey rectangle shows the time frame of the down-state.

Morlet wavelet analysis was used to compare the oscillatory power of AEPs evoked in the three states. Intensive power increase is seen in every frequency bands during SWS after the click stimuli (Figure 4.11.F.; Figure 4.12.). The most intense increase is apparent in the low frequency ranges (at ~10 ms in SWS, ~8dB). This is followed by a long lasting power decrease in SWS (25-100 ms, min: -4dB), mostly apparent on higher frequencies. There is a slight power decrease even in REM (85-200 ms, min: -1.5 dB) after the initial increase, which is not present in wakefulness. LFP spectrogram (Figure 4.11.E.; Figure 4.12.) showed elevated power in the gamma range 10-100 ms post stimulus indicative of local processing only in wake and REM.

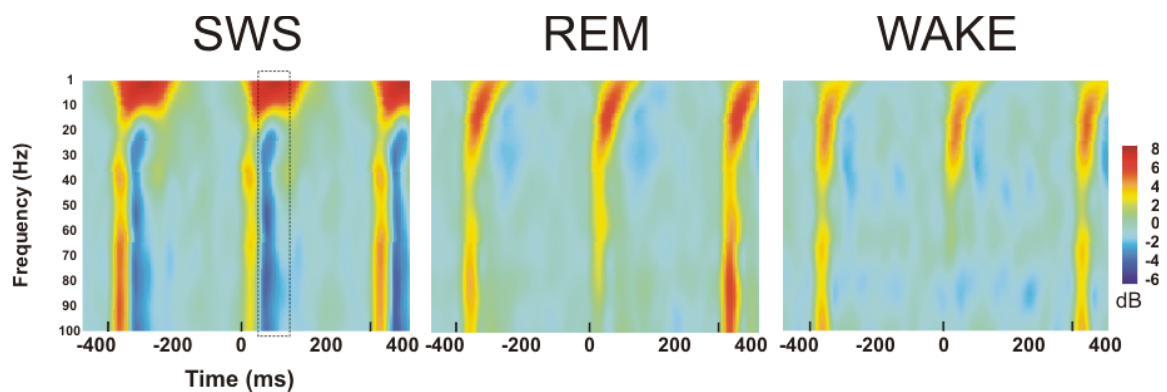


Figure 4.12. Time-frequency analyses (Morlet wavelet) of evoked activities (3/sec click) in SWS, REM and wakefulness. The timing of each stimulus is indicated with short black lines on time-axis. Intensive power increase is seen in every frequency band after the click stimuli in SWS, especially in the low frequency ranges. Note the long-lasting power decrease in SWS that is absent in REM or waking states. The wavelet maps were calculated using recordings derived from the same contact.

The depth analyses of AEPs power spectra reveals that the initial power increase, that comes after the click stimuli, is more apparent in the deep layers after the click stimuli both in SWS and wakefulness. Elevated power in the gamma range is seen in every cortical layer in wakefulness however it is more explicit in the deep. The long-lasting power decrease in SWS appears in the middle layers, as well as power increase in the low frequency ranges during the initial component.

3.3. Comparing evoked and spontaneous down-states of SWS

To further validate the unity of the sound evoked (Figure 4.13.A-B.) deep positive LFP deflection and the spontaneously occurring (Figure 4.13.C-D.) deep positive wave in SWS, CSD (Figure 4.13A-C.) and MUA (Figure 4.13.B-D.) was averaged time locked to the onset of the detected down-states. Confirming our initial assumption, we could not find significant difference in the depth distribution of CSD (Figure 4.13.E.) or MUA

(Figure 4.13.F.) in the temporal range of the down-state (t-test, Bonferroni corrected, $p > 0.2$) suggesting similar neuronal generator mechanisms.

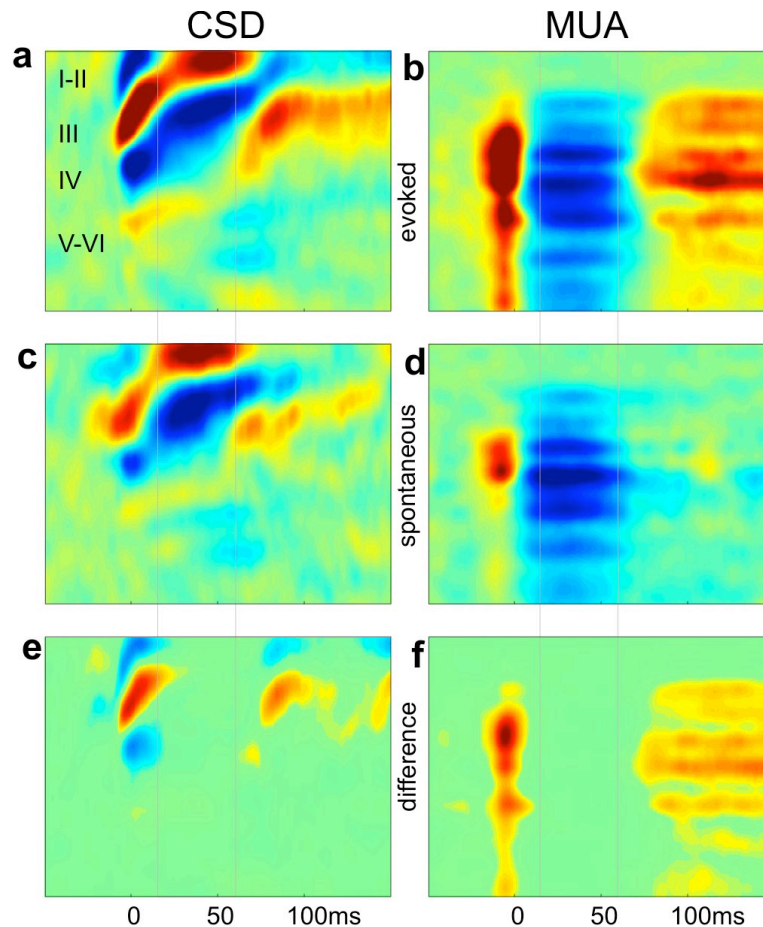


Figure 4.13. CSD and MUA maps of evoked and spontaneous down-states in SWS. **a**, Click evoked down-state (only if a down-state was detected within 15-35 ms interval post stimulus) onset locked CSD map. **b**, Stimulus evoked down-state onset locked MUA map. **c**, Spontaneously occurring down-state onset locked CSD map (the stimulus was switched off). **d**, Spontaneously occurring down-state onset locked MUA map. **e**, Difference CSD map of evoked and spontaneous down-states. Green indicates no significant differences (t-test, Bonferroni corrected to multiple comparison, $p > 0.2$). **f**, Difference MUA map of evoked minus spontaneous down-states. Green indicates no significant differences (t-test, Bonferroni corrected to multiple comparison, $p > 0.2$). During the approximate time of the down-state (grey box) there are no significant differences between evoked and spontaneous activity.

3.4. Cortical oscillatory dynamics in SWS and anesthesia

KX anesthesia is frequently used as a model of natural SWS without careful criticism. Comparing neural signatures of spontaneous and click evoked neural activities recorded in KX anesthesia as well as in SWS we have found a number of important differences. The AC under KX anesthesia exhibited much more spontaneous rhythmic SO than in

SWS. The recurrence frequency of the spontaneous down-states was significantly (Kruskal-Wallis ANOVA, $p < 0.001$) lower in SWS (0.2-0.5 1/sec) than under KX (0.5-1.5 1/sec). The average duration of the down-states in KX was significantly longer (t-test, $p < 0.001$) than in SWS (Figure 4.14.; Figure 4.15.). In deep SWS 60-100% of the random or rhythmic stimuli elicited precisely synchronized down-states, while this measure significantly dropped (Kruskal-Wallis ANOVA, $p < 0.001$) in deep KX anesthesia (5-10%). According to these observations, KX anesthesia freezes cortical oscillations and prevents natural sleep related cortical dynamics to develop.

The MUA and CSD revealed that random/rhythmic click evoked down-states of SWS has similar background mechanism as spontaneously occurring down-states of KX anesthesia. However, there are some significant differences. The main difference is their duration, being about 100 ms and 200 ms respectively. Besides, CSD of KX down-states implied simpler intracortical patterns during anesthesia since the serial sink-source present in layer V-VI CSD of SWS do not appear on KX maps but only a slight source present in layer V-VI CSD of SWS do not appear on KX maps but only a slight source (Figure 4.14.; Figure 4.15.). Moreover a significant sink-source-sink triplet series can be found in SWS in the layer III after the click presentation while only a source is present on the KX map in the same time interval. Similarly, there is a source-sink-source triplet in layer I on the CSD map which is the inverted activity pattern of layer III. The inverted activity pattern of layer III KX CSD map can be found in layer I as well, which is accordingly a sink.

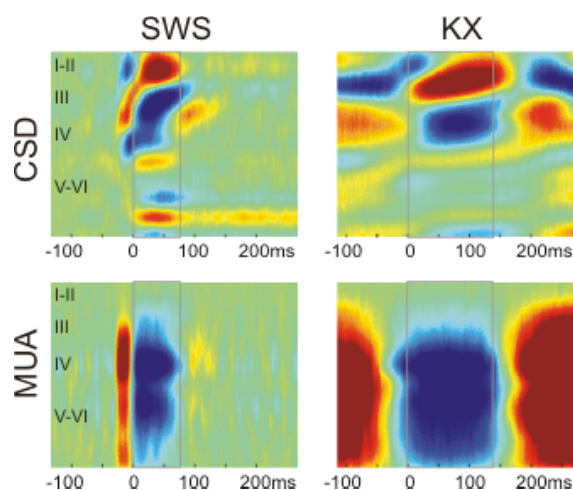


Figure 4.14. MUA and CSD maps related to averages of down-states evoked with click stimuli in SWS and spontaneously occurring in KX anesthesia. Cortical layers are represented with roman numerals. Sinks on CSD maps are depicted with red, sources with blue, arbitrary unit. Red on MUA maps indicates increased, blue decreased activity in arbitrary units compared to baseline. Laminarization is indicated by Roman numerals.

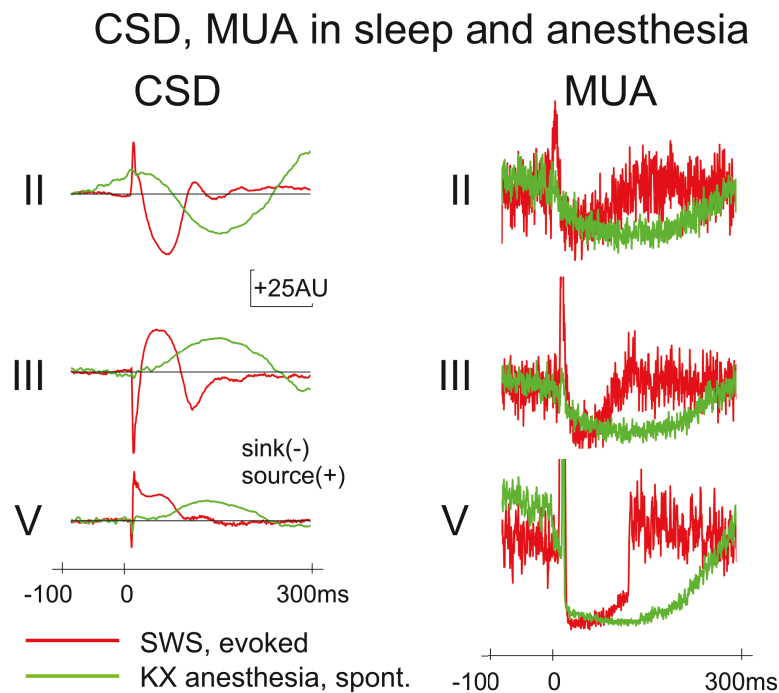


Figure 4.15. CSD and MUA averages related to down-states evoked with click stimuli in SWS and spontaneously occurring in KX anesthesia.

3.5. Double click stimuli evoked responses in the cat AC in SWS and wakefulness

The down-state character of the click evoked positive LFP and the decreased MUA in the 25-100 ms latency range could be demonstrated by double click stimuli. In active wakefulness a second click presented at 20-40 ms delay after the first one (Figure 4.16.A.; Figure 4.16.E.), elicited significantly smaller initial excitation indexed by the peak amplitude of layer III sink (t-test, $p < 0.001$) and corresponding MUA (t-test, $p < 0.001$). The initial CSD and MUA response recovered to at least 80% of its initial value if the second click was presented at 80-100 ms delay or longer (Figure 4.16.C.; Figure 4.16.E.). In SWS the initial CSD (Figure 4.16.B.) and MUA (Figure 4.16.F.) response to the 20-40 ms delayed second click was even more suppressed compared to the wake state (t-test, $p < 0.001$), however it also recovered to at least 80% of its initial value after an 80-100 ms delay (Figure 4.16.D.; Figure 4.16.F.).

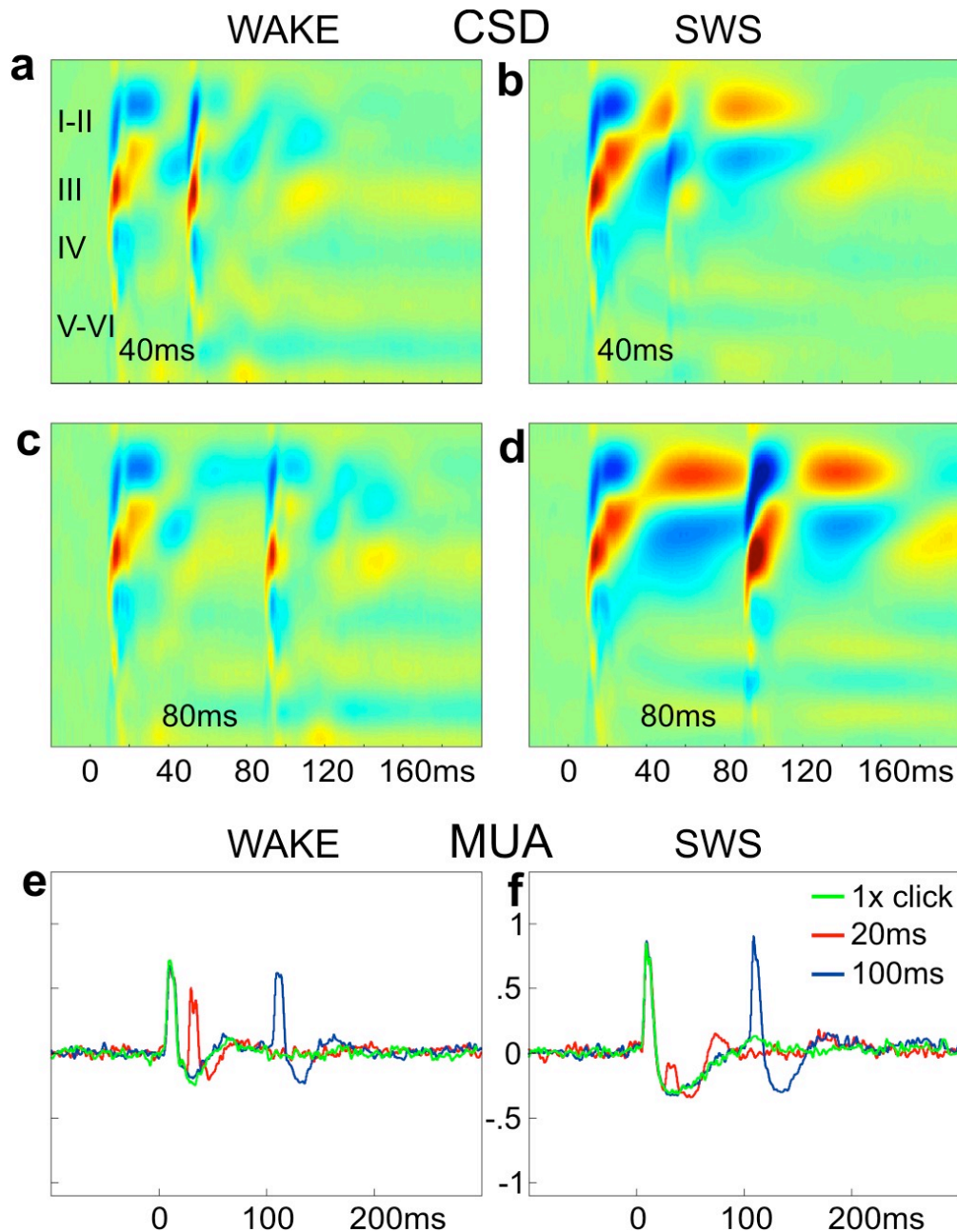


Figure 4.16. CSD and MUA responses to double click stimuli in wakefulness and SWS. **a**, CSD map in response to a short delay (40 ms) double click stimuli in wakefulness. **b**, CSD map in response to the short delay stimuli in SWS. **c**, CSD map in response to a long delay (80 ms) double click stimuli in wakefulness. **d**, CSD map in response to the long delay stimuli in SWS. Note that the CSD response to the second click on **b**, is highly suppressed and even the 80 ms delayed second stimulus on **d** can evoke a clear down-state. **e**, MUA (arbitrary units) from layer III of another cat time locked to the stimulus in wakefulness. Single click response in green, short (20 ms) delay double click response in red, long (100 ms) delay response in blue. **f**, MUA responses in SWS. Note the large difference at short delays (red trace) between wakefulness and SWS. Note also that the evoked down-state is present even in response to the 100 ms delayed second click in SWS.

4. Discussion

The sensory representation in sleep is rarely studied. Some animal studies in the 1960's and 1970's investigated the changes of evoked potentials along sensory pathways during the sleep-wake cycle [118, 120, 171-174, 228-231]. Besides, studies based on single cell recordings in animals or event related brain potential recordings in humans are only available. Many studies made strong conclusions in relation with the mode of action of a specific sensory modality in sleep but used anesthetized animal preparations. So far, very few studies are available that report data derived from non-anesthetized, naturally sleeping animals. Perhaps the technical difficulties and the time-consuming recording sessions contributed to the low number of published papers. Studies based on long-term recordings from higher order species that stay phylogenetically closer to humans are very rare. Therefore, I investigated the changes of information processing methods in different layers of the feline AC during the natural sleep-wake cycle on long-term, as well as in KX anesthesia.

Before we conclude in connection with the information processing modes of the thalamocortical loop it is wise to consider others' results on how the sensory information processing mode alters in the prethalamic structures as a function of change of the vigilance level. Steriade's group published that prethalamic transmission is unaffected by changes in vigilance state [232, 233]. Soja revealed that transmission from lumbar spinal neurons and trigeminal sensory neurons does not differ in waking and REM, but is suppressed during SWS [234-236]. Moreover, the modulation of sensory transmission in different vigilance states is not uniform for all types of stimuli conveyed by the same sensory tract. While tooth-pulp evoked responses were decreased in REM compared to wakefulness, responses of facial hair mechanoreceptors to air puff were increased [235, 237-239]. In the rat visual system retinal ganglion cells responded differently to flashes of light in wake and SWS states. Their responses were variable during REM, either showing SWS or wakefulness like features [240]. Significant amount of recorded cells exhibited changes in firing rate in the pre-thalamic auditory system with change of the vigilance level. Cells of the cochlear nucleus, the lateral superior olive or the inferior colliculus changed their activities from wakefulness to SWS and from SWS to REM, however no dominant effect was observed because almost as many cells increased their activity as decreased. Velluti investigated the cochlear microphonic potential and the compound action potential of the VIIIth nerve in SWS and REM and also found some

differences [241]. In the light of these results Steriade's idea about unchanged pre-thalamic transmission seems unrealistic because prior to diencephalic processing, state-dependent information transmission modulation occurs.

The classic theory of forebrain serial processing considers thalamus as a relay for ascending information that is propagated towards the cortex in a point-to-point fashion [113, 114, 184, 232, 233, 242, 243]. In the visual [244, 245], somatosensory [246, 247] and auditory thalamus [248] decreased evoked responses were recorded in SWS compared to wakefulness. In the auditory thalamocortical system the frequency tuning curves were systematically investigated as well [116]. In the auditory thalamus the RF size and enhanced frequency selectivity was seen during SWS compared to waking. In REM they found neurons with significant RF changes as well as neurons which RF size was comparable to those in waking. On the population level the shape of the auditory thalamic neurons' intensity-function was not changed in SWS or REM. In contrast, many auditory cortical neurons showed RF change in SWS, however on the population level the RF size and the frequency selectivity was not modified significantly because of the compensating effect of response heterogeneity [116, 239].

Transfer ratio (the ratio between EPSPs and spikes) of feline visual thalamic neurons fell from 0.9 to 1.0 in wakefulness to 0.4-0.5 in SWS [249]. Livingstone and Hubel reported [244] that RF size of visual thalamic cells did not change during arousal from drowsiness or SWS and the orientation and direction selectivity of visual cortical neurons did not change or slightly increased.

The classic view overlooks the importance of feedback system that interacts with the ascending auditory pathway nearly continuously, as well as the influence of the limbic system on perception, not to mention the effect of corticocortical information processing [144]. In the thalamus high frequency bursts characterize the SWS state [250-252]. Some groups stressed the importance of these bursts in sensory processing to cortex [253], while others seriously criticized and tried to confute that hypothesis [254, 255]. When auditory thalamic neurons fire in response to acoustic stimuli burst firing mode is usually triggered at neuron's best frequency and they have smaller latency variability and shorter response latency [256]. Thalamic bursts enhance the probability of cortical neurons firing [257, 258] therefore they likely play role in maintaining cortical neurons' responsiveness to sensory inputs during SWS [239].

The burst mode of thalamus in SWS and sustained single spike activity in REM and wakefulness is influenced by different modulatory systems originating in the brainstem,

the hypothalamus and the basal forebrain [233, 259]. The limbic system influences auditory information processing by modulating behavioral arousal level, meanwhile corticothalamic input modifies ongoing behavior very rapidly [144]. Attentional processes influence sensory processing either by facilitating responses to target stimuli or by suppressing responses to non-target stimuli [260]. Another factor that might modulate sensory processing at least in humans during sleep is the timing of experiment within one sleep session [261].

Investigations at cortical cell level provided less homogenous results. Some found no response alteration from waking to sleep [262, 263] or less responsive cells in SWS [244, 264]. In other studies cortical cells showed heterogeneous response changes from waking to SWS. There were cells with decreased (38%), increased (48%) and unchanged firing rate in SWS (14%) in the AC of guinea pigs. On the whole cell population level, the response latency, the frequency selectivity and the size of the suprathreshold RF of auditory cortical cells showed no significant differences between waking, REM and SWS [116]. Issa and Wang revealed that the evoked responses in the marmoset monkey primary AC were also increased or decreased during SWS and that of the secondary auditory cortical (lateral belt) neurons' responses showed no clear systematic depressive effect during SWS. They reported well-preserved sound evoked activity on the population level during REM and SWS [117].

While the thalamic neurons are hyperpolarized and inactive as a consequence of inhibition from GABAergic thalamic reticular neurons cortical neurons display rich activity. The hypothesis was earlier raised that cortical networks might act as amplifiers of incoming thalamic information [113, 233]. Given the fact that thalamocortical connectivity dedicated to transform incoming sensory information constitutes a minor proportion of synaptic contacts in the cerebral cortex, because corticocortical and corticothalamic excitatory synapses far exceed the number of thalamocorticals [265-267], this hypothesis seems a good starting point.

In contrast to the classic theory of thalamic gating in sleep, it seems that different sensory cortical areas receive input from the periphery even during SWS. Indeed, peripheral stimulation evoked sensory information passed the thought thalamic gate and reached the cortex during all phases of the slow oscillation [268]. The change in sensory responses is less significant at the cortical neurons' population level than in the thalamic and sub-thalamic levels. Nevertheless, changes observed at the cortical level in SWS compared with waking were significantly heterogeneous than at thalamic or sub-thalamic

levels. It might be due to the variability of cortical responsiveness in different phases of SWS [269] or due to the diversity of morphological and physiological cell types in cerebral cortex [243]. Since the cortical neurons remain responsive to sensory stimuli in SWS and REM, the classic theory according to which the thalamus plays a relay that disconnects the external world from the sleeping brain seems unrealistic.

According to our and others' results it is proved that sensory information reaches the corresponding cortical area in SWS and REM but it remains unknown what information is conveyed through the sensory system during sleep and what content that information carries. Some studies reported similar firing rates of acoustic cortical neurons to different acoustic stimuli, however the authors could discriminate between the given stimuli based on other features of the cells' response [270, 271].

In humans auditory event related brain potential recordings showed that early components (<10-15ms) are relatively state independent. These components reflect peripheral and brainstem activation. The middle latency components, that reflect thalamocortical involvement, are less consistent and more affected in SWS than in REM. The late components (>100 ms) are the most altered, especially in SWS. The late components show increased complexity due to the non-REM sleep specific pattern of K-complex and the vertex sharp wave. The ERP morphology in REM is similar to what can be recorded in wakefulness [239].

Mismatch negativity (MMN) experiments with humans proved that MMN does not appear on human EEG in non-REM sleep, however it was thought that it reflects pre-attentive processes occurring automatically [272-274]. In REM MMN with reduced amplitude was found [272, 273, 275]. It was suggested that previously acquired information can facilitate automatic change detection in sleep, since MMN to infrequent acoustic stimuli was found in subjects that were trained earlier to behaviorally discriminate two complex patterns in waking.

Functional magnetic resonance imaging (fMRI) studies revealed decreased activation on the primary and secondary auditory cortical areas during non-REM sleep in humans. The acoustic stimulation induced negative fMRI signal was more pronounced during stage 2 sleep and positively correlated with increases in EEG delta power and occurrence frequency of human K-complexes. It was concluded that these evoked negative deflections represent cortical deactivations, thus having sleep protecting role in humans [276]. ERP and fMRI results indicate that some capabilities for auditory discrimination are preserved in the sleeping brain, allowing monitoring of the physical environment and

recognition of intrinsically meaningful stimuli (subject's name) [239]. These results support the idea, that sensory representation may be active during sleep. The fact that awakening of sleeping mothers to their own baby's cry increased from 58% on the first three postnatal nights to 96% on the fourth night also underpin this idea. Moreover, it was shown in animal experiments that sensory thresholds for awakening from SWS or REM are lowered, if the awaking acoustic stimulus acquires significance during wakefulness [277-279]. It is obvious that behaviorally important information can be identified during sleep in humans and animals [239] The question is what neural mechanisms play the key role in that process.

Audition may have evolutionally developed such a way, that it had to fulfill two antagonistic tasks. It had to filter out unnecessary information to protect sleep, while it had to detect potentially dangerous sounds to facilitate awakening. The stability of the initial components of the auditory response in SWS as well as the evoked down-states in natural sleep - similar to the down-state phase of spontaneous slow oscillation under anesthesia - are major contributors to fulfill these needs in the cat AC. I hypothesize that induced down-state as a special cortical processing mode acts as a sleep protecting mechanisms. At short timescale, evoked down-states gate sensory processing via literally 'shutting down' cortical oscillations and pushing membrane potential away from the firing threshold. Down-states disrupt local neuronal activity, thus the continuity of perception becomes blocked and stimuli will not be further processed. I proved with the paired pulse experiment that cellular and trans-membrane response to the second stimulus was attenuated if it was presented within the time frame of the evoked down-state. In contrast, at longer timescales, signal changes can disrupt the generation of the evoked down-states in a probabilistic manner, which might lead to awakening. Neural signals emitted during sleep have some content and some functional relevance, carrying some information. The absence of attentional and intentional processes limits the online processing of environmental stimuli [239]. According to our results, information processing in the cortex during sleep is inhibited by the evoked down-states which blocks the information processing in the 25-100 ms time interval after the stimuli and prevent from awakening if the stimulus is irrelevant. A functional network very likely exists that detects emotionally relevant acoustic stimuli during sleep and alerts the organism. On the global cortical scale, human K-complexes [91] act similarly as the evoked down-states in the cat auditory system, implicating that sleep protecting mechanisms may essentially be uniform across species.

Several groups tried to draw inferences relating information processing of the sensory system by using anesthetized animal models. Castro Alamancos published papers related to information processing in the barrel cortex of rats of whom arousal state were mimicked by stimulation of the brainstem reticular nucleus, however they were anesthetized with urethane [115, 280]. He reported that evoked responses in the barrel cortex were suppressed during arousal, which limited the spread of sensory inputs through the cortex and reduced the size of sensory representations [115, 239, 280]. These results have many weaknesses. It was reported previously that with increasing the anesthetic depth the RF size of thalamic and cortical neurons increased not decreased. Moreover, SWS not waking was characterized by reduced thalamic responsiveness before and wider RF size was found in SWS not in the desynchronized state of wakefulness [239]. The most important point is that they used anesthetic that is known to alter the mode of action of sensory neurons therefore the information processing as well [281]. Our results reflect that slow oscillation recurs significantly often in the AC in KX anesthesia compared even to deep SWS. The average duration of down-states in KX was significantly longer than in SWS. Moreover, probability of evoking potentials with random or rhythmic acoustic stimuli during KX was significantly lower than in SWS. That is why drawing conclusions in connection with sensory information processing of the sleeping or wakeful brain based on data recorded from anesthetized animals is impermissible. Further studies strengthening this statement revealed that the evoked response patterns in SWS were significantly different from waking, from the sensory periphery up to the thalamocortical system [282-286].

Chapter Five

SUMMARY

1. Novel scientific results

I. Thesis group: Design, fabrication and test of a novel double-sided wet etched multisite silicon neural probe.

The idea of designing and fabricating a novel multisite silicon probe in Hungary came to my mind after spending my first Ph.D. year at the NeuroNexus Technologies and the Neural Engineering Laboratory of the University of Michigan.

On one hand the multisite small scale but fragile silicon probes they had developed for a long while in Michigan, on the other hand the robust, reliable but handmade, therefore labouriously reproducible stainless steel shank based microwire laminar arrays that were fabricated in Hungary in the early 90's, motivated me to give rise to a highly reproducible batch fabricated silicon multisite probe with small dimensions and less tissue damaging shape but good mechanical properties.

I.1. I designed a multisite probe with 24 sites and good mechanical properties for acute intracortical recordings.

I.2. By using a CMOS compatible process, based on double-sided anisotropic etching of silicon monocrystal, a multisite neural probe with parallel lateral walls, rounded edges and a yacht-bow like tip was fabricated, which dimensions are variable in a wide range.

I.3. I proved that the probe presented under thesis point I.2., is capable to record good quality field potentials, multiunit and unit activities in acute rat experiments.

II. Thesis group: Analyzing tissue reactions around inactive NeuroProbes silicon probes coated with biocompatible coatings and implanted into the rat cortex for short- and long-term.

NeuroProbes, a project within the frame of the European Union's FP6 program, has 14 participants. 11 research laboratories and 3 companies. Its main aim is to fabricate 3D multisite electrode arrays that, beyond recording neural activities, are capable to

stimulate the tissue, have drug delivery capacities and less tissue damaging. One of the consortial projects, which I had the luck to work on and which the IP-HAS was responsible for, was biocompatibility issues related investigations. I have gathered precious experiences in this project that I can use to predict the effect of expected immunoreactions around the Hungarian probes.

II.1. I have shown that biocompatible coatings deposited on the surface of inactive NeuroProbes silicon probes have immunosuppressing/reaction decreasing effect, especially on short-term. The efficiency of the coatings in terms of optimal neuronal survival followed the same order on short- (1 week) and long-term (8 weeks): 1. dexamethasone (DexM), 2. a mixture of hyaluronic acid (Hya) and DexM, 3. uncoated Si, 4. dextrane (Dex), 5. Hya (less efficient).

II.2. I proved that microbleeding that occurs incidentally during the implantation, has serious destructing effect on the tissue located in the vicinity of the probe track on short- and long-term. According to my results the chance of hitting a blood vessel, therefore the destructing effect of bleeding, decreases by going from superficial towards the deep layers. These results might explain the reason why a fraction of sites often cannot record satisfactory quality bioelectrical activities (especially from the superficial layers).

III. Thesis group: Information processing in the cat auditory cortex during the natural sleep-wake cycle and anesthesia

The field of application of multi-site laminar probes, in studying the cortical mechanisms of information processing, has been widening. I investigated the alteration of acoustic evoked potentials and spontaneous cell activities during the natural sleep-wake cycle and anesthesia on freely moving cats that were implanted with a 24 sites microwire based laminar stainless steel array for chronic use.

III.1. After analyzing bioelectrical signals recorded from a chronically implantable multisite probe that was inserted into the auditory cortex of cats I have shown that local positivity, following the early components of intracortical evoked potentials, exhibits similar mechanisms than that of

spontaneously occurring down-states. In addition, I proved that ketamine-xylazine anesthesia is not a good model for slow wave phase of natural sleep.

III.2. I have shown, by application of paired stimuli, that the second click stimulus is impaired and evokes significantly smaller response in the 25-100 ms timeframe during SWS compared to wakefulness, that is namely the down-state phase and which seems to have sleep protecting role in the auditory cortex.

2. Application of the results

The three thesis groups of my dissertation focus on the topic of application of intracortical multisite probes and recording of bioelectric signals. The presented Hungarian silicon probe is a specific example for application, however, with its fabrication technology and with the new Deep Reactive Ion Etcher (DRIE) of the Research Institute for Technical Physics and Materials Science of the Hungarian Academy of Sciences, the research for a novel, 5-8 cm long silicon based deep brain probe with 2 hidden drug delivery channels has been started. The dimensions and geometry of the existing silicon probe, thus its mechanical properties, as well as the number of shafts and recording electrodes are all variable in a wide range. Chronically implantable probes can be produced, by combining the existing silicon probe with flexible polyimide output cable. Impedance of electrodes can be significantly decreased, by coating them with various coatings (e.g. carbon nanotube). The surface of the electrodes can be used as extracellular ion sensors with the application of ion selective membranes. Suchlike of research directions are expected to come in the near future.

In order to reliably employ multisite probes in chronic recordings and to prevent the recorded signal from degradation it would be important to efficiently reduce or suppress short- and long-term immunoreactions around the probe track. It is visible, after reading the results section of the biocompatibility topic related chapter of my thesis, that different coatings did have impact on the degree of emerging immunoreactions around the probe track, especially on short-term. Significantly reducing the immunoreaction would be probably possible by administrating dexamethasone slowly in a controlled manner on long-term. Dexamethasone filled nanoparticles embedded into the coating or immobilized on the surface of the probe might be a solution of the future. According to our results the degree of neuronal loss and immunoreaction increase, and very likely the

quality of recorded signal decreases, thanks to the considerable amount of cytokines entering from blood vessels to extracellular space at the time of microbleedings by probe implantation occurs. It was proven that more and larger blood vessels are present in superficial layers, than in the deep layers of the neocortex. Therefore, the chance of puncturing a vessel during implantation is higher in the supragranular layers. The chance of hitting a vessel might be lowered by using modern imaging processes before the surgery. Employing biocompatible coatings together with modern imaging processes before the surgery might increase the success rate of long-term recordings.

Down-state was previously thought to exist only as a phase of the slow sleep oscillation which may modulate sensory responses. In contrast, I revealed, by application of multisite recording technology, that acoustic stimulation can reliably and precisely modulate cortical oscillatory state in natural SWS. Besides, it was proven that acoustic intracortical mechanisms, related to information processing, are different in SWS compared to REM and wakefulness. An incomparable feature of the information processing method of the acoustic cortex in SWS was demonstrated, which was not found on other sensory areas.

Audition is the only modality that continuously monitors our environment, even when we sleep. I hypothesize that the novel cortical processing mode, which I described, acts as a sleep protecting mechanisms by disrupting local neuronal activity for a short period of time, thus the continuity of perception becomes impaired and stimuli will not be further processed. The existence of such a deep sleep protecting mechanism implies the important role of SWS in connection with the balanced maintenance of basic life functions. The presented evidence according to KX anesthesia is not a proper model of natural SWS, from the viewpoint of cortical oscillatory dynamics, is an important result. Steriade and his colleagues drawn far-reaching conclusions in connection with the role of thalamus during SWS but used KX anesthetized cats for their experiments. My results warn the reader to think those conclusions over again.

THE AUTHOR'S PUBLICATIONS

Journal papers (cumulative impact factor: 21.298)

- [1] R. Csercsa, B. Dombovári, D. Fabó, L. Wittner, L. Eröss, L. Entz, A. Sólyom, G. Rásonyi, A. Szűcs, A. Kelemen, R. Jakus, V. Juhos, **L. Grand**, A. Magony, P. Halász, T. Freund, S. Cash, G. Karmos, E. Halgren, and I. Ulbert, "Laminar analysis of the slow wave activity in humans," *Accepted for publication in Brain*, 2010.
- [2] D. Fabó, Z. Maglóczky, L. Wittner, A. Pék, L. Eross, S. Czirják, J. Vajda, A. Sólyom, G. Rásonyi, A. Szűcs, A. Kelemen, V. Juhos, **L. Grand**, B. Dombovári, P. Halász, T. F. Freund, E. Halgren, G. Karmos, and I. Ulbert, "Properties of in vivo interictal spike generation in the human subiculum," *Brain*, vol. 131, pp. 485-99, Feb 2008.
- [3] **L. Grand**, B. Dombovari, R. Csercsa, L. Wittner, A. Magony, G. Karmos, and I. Ulbert, "Cortical gating of auditory information processing in sleep," *In preparation for submission*.
- [4] **L. Grand**, A. Pongrácz, É. Vázsonyi, G. Márton, R. Fiáth, B. P. Kerekes, D. Gubán, G. Karmos, I. Ulbert, and G. Battistig, "A novel multisite silicon probe for high quality laminar neural recordings," *Submitted to Sensors and Actuators A - Physics*.
- [5] **L. Grand**, L. Wittner, S. Herwik, E. Göthelid, P. Ruther, S. Oscarsson, H. P. Neves, B. Dombovari, R. Csercsa, G. Karmos, and I. Ulbert, "Short and long term biocompatibility of NeuroProbes silicon multielectrodes," *Journal of Neuroscience Methods*, vol. 189, pp. 216-29, Jun 2010.

Conference paper

- [1] A. A. A. Aarts, H. P. Neves, I. Ulbert, L. Wittner, **L. Grand**, M. B. A. Fontes, S. Herwik, S. Kisban, O. Paul, P. Ruther, R. P. Puers, and C. Van Hoof, "A 3D slim-base probe array for in vivo recorded neuron activity," *Conf IEEE/EMBS*, pp. 5798-5801, 2008.

Patent

- [1] G. Battistig, **L. Grand**, G. Karmos, K. Payer, A. Pongrácz, I. Ulbert, and É. Vázsonyi, "Eljárás CMOS technológiába integrálható, egykristályos Si alapú, nedves kémiai marással készített, párhuzamos oldalfalakkal és lekerekített élekkel határolt extracelluláris elektródok előállítására," *Hungarian patent application (Nr. P0900774)*, 10 December, 2009.

Conference posters

- [1] R. Csercsa, B. Dombovari, **L. Grand**, A. Magony, L. Wittner, L. Eross, G. Karmos, and I. Ulbert, "Supragranular origin of slow sleep oscillations in the human frontal lobe," *Codybs Workshop (Dresden)*, 21-25 June, 2009.
- [2] R. Csercsa, A. Magony, B. Dombovari, **L. Grand**, D. Fabo, L. Entz, L. Wittner, L. Eross, and I. Ulbert, "Laminar properties of sleep slow oscillation in humans," *FENS Forum Abstracts (Genova, Switzerland)*, vol. 4, p. 160.3, 12-16 July, 2008.

-
- [3] B. Dombóvári, **L. Grand**, L. Wittner, G. Karmos, and I. Ulbert, "Comparison of auditory information processing in sleep and anesthesia," *IBRO workshop (Debrecen, Hungary)*, p. P85, 24-26 Jan, 2008.
- [4] B. Dombóvári, K. Seidl, S. Herwik, T. Torfs, **L. Grand**, R. Cserecsa, O. Paul, H. P. Neves, P. Ruther, and I. Ulbert, "Acute recordings using microelectrode arrays with electronic depth control," *IBRO workshop (Pecs, Hungary)*, pp. P7-05, 21-23 Jan, 2010.
- [5] R. Fiáth, D. Horváth, **L. Grand**, L. Wittner, B. Dombóvári, G. Karmos, I. Ulbert, and R. Cserecsa, "Laminar distribution of the spontaneous multiunit activity in the cat auditory cortex during slow wave sleep," *IBRO workshop (Pecs, Hungary)*, pp. P4-10, 21-23 Jan, 2010.
- [6] **L. Grand**, B. Dombóvári, E. Boldizsár, G. Karmos, and I. Ulbert, "Cortical gating of auditory information processing in sleep," *FENS Forum Abstracts (Vienna, Austria)*, vol. 3, 8-12 July, 2006.
- [7] **L. Grand**, B. Dombóvári, R. Cserecsa, L. Wittner, A. Magony, G. Karmos, and I. Ulbert, "Cortical gating of auditory information processing in sleep," *Codybs Workshop (Dresden)*, 21-25 June, 2009.
- [8] **L. Grand**, A. Pongrácz, É. Vázsonyi, G. Márton, D. Gubán, G. Battistig, G. Karmos, and I. Ulbert, "A novel multisite silicon probe fabricated by using an economical wet etching process for high quality laminar neural recordings " *IBRO workshop (Pecs, Hungary)*, pp. P7-11, 21-23 Jan, 2010.
- [9] **L. Grand**, L. Wittner, E. Göthelid, P. Janssen, S. Oscarsson, H. P. Neves, P. Ruther, and I. Ulbert, "Characterization of long-term tissue reaction around Neuroprobes silicon multielectrodes," *Front Syst Neurosci. Conf Abst: 12th Meeting of the Hungarian Neuroscience Society*, 22-24 Jan, 2009.
- [10] **L. Grand**, L. Wittner, E. Göthelid, S. Oscarsson, S. Herwik, P. Ruther, H. P. Neves, G. Karmos, and I. Ulbert, "Assessing tissue reaction around Neuroprobes silicon multielectrodes with different coatings " *SFN Abstracts (Chicago)*, p. 390.1/HH9 17-21 Oct, 2009.
- [11] D. Horváth, **L. Grand**, L. Wittner, B. Dombóvári, S. Kisban, S. Herwik, P. Ruther, H. Neves, G. Karmos, and I. Ulbert, "Long term implantation of silicon-based micro probe arrays " *IBRO workshop (Pecs, Hungary)*, 21-23 Jan, 2010.
- [12] N. B. Langhals, **L. Grand**, R. J. Vetter, and D. R. Kipke, "Characterization Of Noise And Capacitive Losses Of Microelectrodes Through Recordings And Modeling," *IEEE BMES Conf*, p. P3.112., 26-29 Sept, 2007.
- [13] K. Seidl, S. Herwik, R. Cserecsa, B. Dombóvári, **L. Grand**, T. Torfs, H. Neves, I. Ulbert, O. Paul, and P. Ruther, "Acute recording in rat using CMOS-based high-density silicon microprobe array for electronic depth control " *SFN Abstracts (Chicago)*, p. 664.10/DD41 17-21 Oct, 2009.
- [14] I. Ulbert, R. Cserecsa, **L. Grand**, E. Boldizsár, A. Magony, B. Dombóvári, and G. Karmos, "Evoked 'up' states in the cat auditory cortex," *FENS Forum Abstracts (Vienna, Austria)*, vol. 3, p. A073.19, July 8-12, 2006.
- [15] I. Ulbert, **L. Grand**, B. Dombóvári, R. Cserecsa, A. Magony, E. Boldizsár, and G. Karmos, "Evoked cortical hyperpolarization controls auditory information processing in natural non-REM sleep," *SFN Abstracts (Atlanta)* p. 239.1/G5, 14-18 Oct, 2006.

BIBLIOGRAPHY

- [1] M. Chicurel, "Windows on the brain," *Nature*, vol. 412, pp. 266-8, Jul 19 2001.
- [2] A. Bragin, J. F. Hetke, C. L. Wilson, D. J. Anderson, J. Engel, and G. Buzsáki, "Multiple site silicon-based probes for chronic recordings in freely moving rats: implantation, recording and histological verification," *J Neurosci Methods*, vol. 98, pp. 77-82, 2000.
- [3] G. Buzsaki, "Large-scale recording of neuronal ensembles," *Nat Neurosci*, vol. 7, pp. 446-51, May 2004.
- [4] T. A. Christensen, V. M. Pawlowski, H. Lei, and J. G. Hildebrand, "Multi-unit recordings reveal context-dependent modulation of synchrony in odor-specific neural ensembles," *Nat Neurosci*, vol. 3, pp. 927-31, Sep 2000.
- [5] J. Csicsvari, D. A. Henze, B. Jamieson, K. D. Harris, A. Sirota, P. Bartho, K. D. Wise, and G. Buzsaki, "Massively parallel recording of unit and local field potentials with silicon-based electrodes," *J Neurophysiol*, vol. 90, pp. 1314-23, Aug 2003.
- [6] B. L. McNaughton, J. O'Keefe, and C. A. Barnes, "The stereotrode: a new technique for simultaneous isolation of several single units in the central nervous system from multiple unit records," *J Neurosci Methods*, vol. 8, pp. 391-7, Aug 1983.
- [7] J. O'Keefe and M. L. Recce, "Phase relationship between hippocampal place units and the EEG theta rhythm," *Hippocampus*, vol. 3, pp. 317-330, 1993.
- [8] M. A. Wilson and B. L. McNaughton, "Dynamics of the hippocampal ensemble code for space," *Science*, vol. 261, pp. 1055-8, Aug 20 1993.
- [9] G. Karmos, M. Molnar, and V. Csepe, "A new multielectrode for chronic recording of intracortical field potentials in cats," *Physiol Behav*, vol. 29, pp. 567-71, Sep 1982.
- [10] J. L. Kubie, "A driveable bundle of microwires for collecting single-unit data from freely-moving rats," *Physiol Behav*, vol. 32, pp. 115-8, Jan 1984.
- [11] K. C. Cheung, "Implantable microscale neural interfaces," *Biomed Microdevices*, vol. 9, pp. 923-38, Dec 2007.
- [12] I. Ulbert, "Multiple Channel Microelectrode System for Human Epilepsy Research," *Conf IEEE/BiOCAS*, pp. 222 - 225, 2006.
- [13] I. Ulbert, E. Halgren, G. Heit, and G. Karmos, "Multiple microelectrode-recording system for human intracortical applications," *J Neurosci Methods*, vol. 106, pp. 69-79, Mar 30 2001.
- [14] D. Fabo, Z. Magloczky, L. Wittner, A. Pek, L. Eross, S. Czirjak, J. Vajda, A. Solyom, G. Rasonyi, A. Szucs, A. Kelemen, V. Juhos, L. Grand, B. Dombovari, P. Halasz, T. F. Freund, E. Halgren, G. Karmos, and I. Ulbert, "Properties of in vivo interictal spike generation in the human subiculum," *Brain*, vol. 131, pp. 485-99, Feb 2008.
- [15] I. Ulbert, Z. Magloczky, L. Eross, S. Czirjak, J. Vajda, L. Bogнар, S. Toth, Z. Szabo, P. Halasz, D. Fabo, E. Halgren, T. F. Freund, and G. Karmos, "In vivo laminar electrophysiology co-registered with histology in the hippocampus of patients with temporal lobe epilepsy," *Exp Neurol*, vol. 187, pp. 310-8, Jun 2004.
- [16] M. A. Nicolelis, D. Dimitrov, J. M. Carmena, R. Crist, G. Lehew, J. D. Kralik, and S. P. Wise, "Chronic, multisite, multielectrode recordings in macaque monkeys," *Proc Natl Acad Sci U S A*, vol. 100, pp. 11041-6, Sep 16 2003.

- [17] G. Kotzar, M. Freas, P. Abel, A. Fleischman, S. Roy, C. Zorman, J. M. Moran, and J. Melzak, "Evaluation of MEMS materials of construction for implantable medical devices," *Biomaterials*, vol. 23, pp. 2737-50, Jul 2002.
- [18] K. D. Wise, J. B. Angell, and A. Starr, "An integrated-circuit approach to extracellular microelectrodes," *IEEE Trans Biomed Eng*, vol. 17, pp. 238-47, Jul 1970.
- [19] K. Najafi, K. D. Wise, and T. Mochizuki, "A high-yield IC-compatible multichannel recording array," *IEEE Trans Electron Devices*, vol. 32, pp. 1206-1211, 1985.
- [20] K. Najafi and K. D. Wise, "An implantable multielectrode array with on-chip signal processing," *IEEE SOLID-STATE CIRC*, vol. 21, pp. 1035 - 1044, 1986.
- [21] Q. Bai, K. D. Wise, and D. J. Anderson, "A high-yield microassembly structure for three-dimensional microelectrode arrays," *IEEE Trans Biomed Eng*, vol. 47, pp. 281-289, 2000.
- [22] M. Ghovanloo, K. D. Wise, and K. Najafi, "Towards A Button-Sized 1024-Site Wireless Cortical Microstimulating Array," *1st Intl. IEEE/EMBS Conf Neural Eng. Proc*, pp. 138- 141, 2003.
- [23] M. D. Gingerich, J. F. Hetke, D. J. Anderson, and K. D. Wise, "A 256-site CMOS microelectrode array for multipoint stimulation and recording in the central nervous system," *Int Conf Solid State Sens Act*, pp. 416-419, 2001.
- [24] D. J. Anderson, K. Najafi, S. J. Tanghe, and D. A. Evans, "Batch fabricated thin-film electrodes for stimulation of the central auditory system," *IEEE Trans Biomed Eng*, vol. 36, pp. 693-704, 1989.
- [25] P. K. Campbell, K. E. Jones, R. J. Huber, K. W. Horch, and R. A. Normann, "A silicon-based, three-dimensional neural interface: manufacturing processes for an intracortical electrode array," *IEEE Trans Biomed Eng*, vol. 38, pp. 758-68, Aug 1991.
- [26] D. Rakwal, S. Heamawatanachai, P. Tathireddy, F. Solzbacher, and E. Bamberg, "Fabrication of compliant high aspect ratio silicon microelectrode arrays using micro-wire electrical discharge machining," *Microsyst Technol*, vol. 15, pp. 789-797, 2009.
- [27] D. T. Kewley, M. D. Hills, D. A. Borkholder, I. E. Opris, N. I. Maluf, C. W. Stormont, J. M. Bower, and G. T. A. Kovacs, "Plasma-etched neural probes," *SENSORS ACTUAT A-PHYS*, vol. 58, pp. 27-35, 1997.
- [28] S. J. Oh, J. K. Song, J. W. Kim, and S. J. Kim, "A high-yield fabrication process for silicon neural probes," *IEEE Trans Biomed Eng*, vol. 53, pp. 351 - 354, 2006.
- [29] T. H. Yoon, E. J. Hwang, D. Y. Shin, S. I. Park, and S. J. Oh, "A micromachined silicon depth probe for multichannel neural recording," *IEEE Trans Biomed Eng*, vol. 47, pp. 1082-1087, 2000.
- [30] K. C. Cheung, K. Djupsund, Y. Dan, and L. P. Lee, "Implantable multichannel electrode array based on SOI technology," *J Microelectromech Syst*, vol. 12, pp. 179-184, 2003.
- [31] Norlin, M. Kindlundh, A. Mouroux, K. Yoshida, and U. G. Hofmann, "A 32-site neural recording probe fabricated by DRIE of SOI substrates," *J Microelectromech Microeng*, vol. 12, pp. 414-419 2002.
- [32] M. Kindlundh, P. Norlin, and U. G. Hofmann, "A neural probe process enabling variable electrode configurations," *SENSORS ACTUAT B-CHEM*, vol. 102, pp. 51-58, 2004.

- [33] H. P. Neves, G. A. Orban, M. Koudelka-Hep, T. Stieglitz, and P. Ruther, "Development of Modular Multifunctional Probe Arrays for Cerebral Applications," *Proc 3rd Int IEEE Conf on Neural Eng*, pp. 104-109, 2007.
- [34] P. Ruther, A. Aarts, O. Frey, S. Herwik, S. Kisban, K. Seidl, S. Spieth, A. Schumacher, M. Koudelka-Hep, O. Paul, T. Stieglitz, R. Zengerle, and H. P. Neves, "The NeuroProbes Project—Multifunctional Probe Arrays for Neural Recording and Stimulation," *Proc 13th Conf IFEES*, vol. 53, pp. 238-240, 2008.
- [35] S. Kisban, S. Herwik, K. Seidl, B. Rubehn, A. Jezzini, M. A. Umiltà, L. Fogassi, T. Stieglitz, O. Paul, and P. Ruther, "Microprobe array with low impedance electrodes and highly flexible polyimide cables for acute neural recording," *Intl Conf IEEE/EMBS*, vol. 2007, pp. 175-8, 2007.
- [36] S. Spieth, A. Schumacher, K. Seidl, K. Hiltmann, S. Haeberle, R. McNamara, J. W. Dalley, S. A. Edgley, P. Ruther, and R. Zengerle, "Robust microprobe systems for simultaneous neural recording and drug delivery," *4th Europ Conf IFMBS*, vol. 22, pp. 2426-30, 2008.
- [37] O. Frey, P. van der Wal, N. de Rooij, and M. Koudelka-Hep, "Development and characterization of choline and L-glutamate biosensor integrated on silicon microprobes for in-vivo monitoring," *Conf Proc IEEE Eng Med Biol Soc*, vol. 2007, pp. 6040-3, 2007.
- [38] A. A. A. Aarts, H. P. Neves, I. Ulbert, L. Wittner, L. Grand, M. B. A. Fontes, S. Herwik, S. Kisban, O. Paul, P. Ruther, R. P. Puers, and C. Van Hoof, "A 3D slim-base probe array for in vivo recorded neuron activity," *Conf IEEE/EMBS*, pp. 5798-5801, 2008.
- [39] S. Herwik, S. Kisban, A. A. A. Aarts, K. Seidl, G. Girardeau, K. Benchenane, M. B. Zugaro, S. I. Wiener, O. Paul, H. P. Neves, and P. Ruther, "Fabrication technology for silicon-based microprobe arrays used in acute and sub-chronic neural recording," *J Micromech Microeng*, vol. 19, 2009.
- [40] Y. Y. Chen, H. Y. Lai, S. H. Lin, C. W. Cho, W. H. Chao, C. H. Liao, S. Tsang, Y. F. Chen, and S. Y. Lin, "Design and fabrication of a polyimide-based microelectrode array: application in neural recording and repeatable electrolytic lesion in rat brain," *J Neurosci Methods*, vol. 182, pp. 6-16, Aug 30 2009.
- [41] T. Stieglitz and M. Gross, "Flexible BIOMEMS with electrode arrangements on front and back side as key component in neural prostheses and biohybrid systems" *SENSORS ACTUAT B-CHEM*, vol. 83, pp. 8-14, 2002.
- [42] D. Pellinen, T. Moon, R. Vetter, R. Miriani, and D. Kipke, "Multifunctional flexible parylene-based intracortical microelectrodes," *Conf Proc IEEE Eng Med Biol Soc*, vol. 5, pp. 5272-5275, 2005.
- [43] C. W. Lin, Y. T. Lee, C. W. Chang, W. L. Hsu, Y. C. Chang, and W. Fang, "Novel glass microprobe arrays for neural recording," *Biosens Bioelectron*, vol. 25, pp. 475-81, Oct 15 2009.
- [44] J. J. Burmeister, K. Moxon, and G. A. Gerhardt, "Ceramic-based multisite microelectrodes for electrochemical recordings," *Anal Chem*, vol. 72, pp. 187-192, 2000.
- [45] K. A. Moxon, N. M. Kalkhoran, M. Markert, M. A. Sambito, J. L. McKenzie, and J. T. Webster, "Nanostructured surface modification of ceramic-based microelectrodes to enhance biocompatibility for a direct brain-machine interface," *IEEE Trans Biomed Eng*, vol. 51, pp. 881-9, Jun 2004.
- [46] G. Battistig, L. Grand, G. Karmos, K. Payer, A. Pongrácz, I. Ulbert, and É. Vázsonyi, "Eljárás CMOS technológiába integrálható, egykristályos Si alapú, nedves kémiai marással készített, párhuzamos oldalfalakkal és lekerekített élekkel

- határolt extracelluláris elektródok előállítására," *Hungarian patent application (Nr. P0900774)*, 10 December, 2009.
- [47] E. Vazsonyi, Z. Vertesy, A. Toth, and J. Szlufcik, "Anisotropic etching of silicon in a two-component alkaline solution," *J. Micromech Microeng*, vol. 13, pp. 165-169, 2003.
- [48] Y. Terasawa, A. Uehara, H. Kanda, H. Tashiro, and M. Ozawa, "A method of surface-area enhancement of platinum bulk electrode with electrochemical etching," *SFN Abstracts (Chicago)*, p. 5048/CC43, 17-21 October, 2009.
- [49] M. Steriade, A. Nunez, and F. Amzica, "A novel slow (< 1 Hz) oscillation of neocortical neurons in vivo: depolarizing and hyperpolarizing components," *J Neurosci*, vol. 13, pp. 3252-65, Aug 1993.
- [50] E. W. Keefer, B. R. Botterman, M. I. Romero, A. F. Rossi, and G. W. Gross, "Carbon nanotube coating improves neuronal recordings," *Nat Nanotechnol*, vol. 3, pp. 434-9, Jul 2008.
- [51] K. Najafi, J. Ji, and K. D. Wise, "Scaling limitations of silicon multichannel recording probes," vol. 37, pp. 1-11, 1990.
- [52] R. A. Normann, P. K. Campbell, and W. P. Li, "Silicon based microstructures suitable for intracortical electrical stimulation (visual prosthesis application)," *Conf Proc IEEE/EMBS*, pp. 714-715, 1988.
- [53] S. J. Oh, J. K. Song, and S. J. Kim, "Neural interface with a silicon neural probe in the advancement of microtechnology," *Biotechnol Bioprocess Eng*, vol. 8, pp. 252-256, 2003.
- [54] A. B. Schwartz, "Cortical neural prosthetics," *Annu Rev Neurosci*, vol. 27, pp. 487-507, 2004.
- [55] A. A. A. Aarts, H. P. Neves, R. P. Puers, and C. Van Hoof, "An interconnect for out-of-plane assembled biomedical probe arrays," *J Micromech Microeng*, vol. 18, pp. 064004-10, 2008.
- [56] J. W. Fawcett and R. A. Asher, "The glial scar and central nervous system repair," *Brain Res Bull*, vol. 49, pp. 377-91, Aug 1999.
- [57] J. N. Turner, W. Shain, D. H. Szarowski, M. Andersen, S. Martins, M. Isaacson, and H. Craighead, "Cerebral astrocyte response to micromachined silicon implants," *Exp Neurol*, vol. 156, pp. 33-49, Mar 1999.
- [58] W. Shain, L. Spataro, J. Dilgen, K. Haverstick, S. Retterer, M. Isaacson, M. Saltzman, and J. N. Turner, "Controlling cellular reactive responses around neural prosthetic devices using peripheral and local intervention strategies," *IEEE Trans Neural Syst Rehabil Eng*, vol. 11, pp. 186-8, Jun 2003.
- [59] D. H. Szarowski, M. D. Andersen, S. Retterer, A. J. Spence, M. Isaacson, H. G. Craighead, J. N. Turner, and W. Shain, "Brain responses to micro-machined silicon devices," *Brain Res*, vol. 983, pp. 23-35, Sep 5 2003.
- [60] D. J. Edell, V. V. Toi, V. M. McNeil, and L. D. Clark, "Factors influencing the biocompatibility of insertable silicon microshafts in cerebral cortex," *IEEE Trans Biomed Eng*, vol. 39, pp. 635-43, Jun 1992.
- [61] V. S. Polikov, P. A. Tresco, and W. M. Reichert, "Response of brain tissue to chronically implanted neural electrodes," *J Neurosci Methods*, vol. 148, pp. 1-18, Oct 15 2005.
- [62] D. R. Merrill, M. Bikson, and J. G. Jefferys, "Electrical stimulation of excitable tissue: design of efficacious and safe protocols," *J Neurosci Methods*, vol. 141, pp. 171-98, Feb 15 2005.

- [63] A. C. Hoogerwerf and K. D. Wise, "A three-dimensional microelectrode array for chronic neural recording," *IEEE Trans Biomed Eng*, vol. 41, pp. 1136-46, Dec 1994.
- [64] R. Biran, D. C. Martin, and P. A. Tresco, "Neuronal cell loss accompanies the brain tissue response to chronically implanted silicon microelectrode arrays," *Exp Neurol*, vol. 195, pp. 115-26, Sep 2005.
- [65] J. R. Fraser, T. C. Laurent, and U. B. Laurent, "Hyaluronan: its nature, distribution, functions and turnover," *J Intern Med*, vol. 242, pp. 27-33, Jul 1997.
- [66] T. Pouyani and G. D. Prestwich, "Functionalized derivatives of hyaluronic acid oligosaccharides: drug carriers and novel biomaterials," *Bioconjug Chem*, vol. 5, pp. 339-47, Jul-Aug 1994.
- [67] D. Pasqui, A. Atrei, and R. Barbucci, "A novel strategy to obtain a hyaluronan monolayer on solid substrates," *Biomacromolecules*, vol. 8, pp. 3531-9, Nov 2007.
- [68] C. M. Lin, J. W. Lin, Y. C. Chen, H. H. Shen, L. Wei, Y. S. Yeh, Y. H. Chiang, R. Shih, P. L. Chiu, K. S. Hung, L. Y. Yang, and W. T. Chiu, "Hyaluronic acid inhibits the glial scar formation after brain damage with tissue loss in rats," *Surg Neurol*, vol. 72, pp. 50-54, 2009.
- [69] A. S. Gallus and J. Hirsh, "Antithrombotic drugs: part II," *Drugs*, vol. 12, pp. 132-57, 1976.
- [70] P. C. Johnson and J. H. Barker, "Thrombosis and antithrombotic therapy in microvascular surgery," *Clin Plast Surg*, vol. 19, pp. 799-807, Oct 1992.
- [71] F. Abir, S. Barkhordarian, and B. E. Sumpio, "Efficacy of dextran solutions in vascular surgery," *Vasc Endovascular Surg*, vol. 38, pp. 483-91, Nov-Dec 2004.
- [72] C. I. Jones, D. A. Payne, P. D. Hayes, A. R. Naylor, P. R. Bell, M. M. Thompson, and A. H. Goodall, "The antithrombotic effect of dextran-40 in man is due to enhanced fibrinolysis in vivo," *J Vasc Surg*, vol. 48, pp. 715-22, Sep 2008.
- [73] S. P. Massia, J. Stark, and D. S. Letbetter, "Surface-immobilized dextran limits cell adhesion and spreading," *Biomaterials*, vol. 21, pp. 2253-61, Nov 2000.
- [74] L. Spataro, J. Dilgen, S. Retterer, A. J. Spence, M. Isaacson, J. N. Turner, and W. Shain, "Dexamethasone treatment reduces astroglia responses to inserted neuroprosthetic devices in rat neocortex," *Exp Neurol*, vol. 194, pp. 289-300, Aug 2005.
- [75] R. Twycross, "The risks and benefits of corticosteroids in advanced cancer," *Drug Saf*, vol. 11, pp. 163-78, Sep 1994.
- [76] P. J. Koehler, "Use of corticosteroids in neuro-oncology," *Anticancer Drugs*, vol. 6, pp. 19-33, Feb 1995.
- [77] E. C. Kaal and C. J. Vecht, "The management of brain edema in brain tumors," *Curr Opin Oncol*, vol. 16, pp. 593-600, Nov 2004.
- [78] Y. Zhong and R. V. Bellamkonda, "Dexamethasone-coated neural probes elicit attenuated inflammatory response and neuronal loss compared to uncoated neural probes," *Brain Res*, vol. 1148, pp. 15-27, May 7 2007.
- [79] Y. Zhong, G. C. McConnell, J. D. Ross, S. P. DeWeerth, and R. V. Bellamkonda, "A novel dexamethasone-releasing, anti-inflammatory coating for neural implants," in *2nd International IEEE EMBS Conference on Neural Engineering*, Arlington, Virginia, USA, 2005, pp. v-viii.
- [80] G. Paxinos and C. Watson, *The rat brain in stereotaxic coordinates*, 4th edition. Sidney: Academic Press, 1998.

- [81] G. Ledung, M. Bergkvist, A. P. Quist, U. Gelius, J. Carlsson, and S. Oscarsson, "A novel method for preparation of disulfides on silicon," *Langmuir*, vol. 17, pp. 6056-6058, 2001.
- [82] R. J. Mullen, C. R. Buck, and A. M. Smith, "NeuN, a neuronal specific nuclear protein in vertebrates," *Development*, vol. 116, pp. 201-11, Sep 1992.
- [83] E. Gould, A. J. Reeves, M. S. Graziano, and C. G. Gross, "Neurogenesis in the neocortex of adult primates," *Science*, vol. 286, pp. 548-52, Oct 15 1999.
- [84] L. F. Eng and S. J. DeArmond, "Glial fibrillary acidic (GFA) protein immunocytochemistry in development and neuropathology," *Prog Clin Biol Res*, vol. 59A, pp. 65-79, 1981.
- [85] M. Kalman and F. Hajos, "Distribution of glial fibrillary acidic protein (GFAP)-immunoreactive astrocytes in the rat brain. I. Forebrain," *Exp Brain Res*, vol. 78, pp. 147-63, 1989.
- [86] J. S. King, "A light and electron microscopic study of perineuronal glial cells and processes in the rabbit neocortex," *Anat Rec*, vol. 161, pp. 111-23, May 1968.
- [87] K. Hama, T. Arii, and T. Kosaka, "Three-dimensional organization of neuronal and glial processes: high voltage electron microscopy," *Microsc Res Tech*, vol. 29, pp. 357-67, Dec 1 1994.
- [88] W. L. Ruten, "Selective electrical interfaces with the nervous system," *Annu Rev Biomed Eng*, vol. 4, pp. 407-52, 2002.
- [89] P. Lakatos, G. Karmos, A. D. Mehta, I. Ulbert, and C. E. Schroeder, "Entrainment of neuronal oscillations as a mechanism of attentional selection," *Science*, vol. 320, pp. 110-3, Apr 4 2008.
- [90] C. J. Keller, S. S. Cash, S. Narayanan, C. Wang, R. Kuzniecky, C. Carlson, O. Devinsky, T. Thesen, W. Doyle, A. Sassaroli, D. A. Boas, I. Ulbert, and E. Halgren, "Intracranial microprobe for evaluating neuro-hemodynamic coupling in unanesthetized human neocortex," *J Neurosci Methods*, vol. 179, pp. 208-18, May 15 2009.
- [91] S. S. Cash, E. Halgren, N. Dehghani, A. O. Rossetti, T. Thesen, C. Wang, O. Devinsky, R. Kuzniecky, W. Doyle, J. R. Madsen, E. Bromfield, L. Eross, P. Halasz, G. Karmos, R. Csercsa, L. Wittner, and I. Ulbert, "The human K-complex represents an isolated cortical down-state," *Science*, vol. 324, pp. 1084-7, May 22 2009.
- [92] I. Ulbert, G. Heit, J. Madsen, G. Karmos, and E. Halgren, "Laminar analysis of human neocortical interictal spike generation and propagation: current source density and multiunit analysis in vivo," *Epilepsia*, vol. 45 Suppl 4, pp. 48-56, 2004.
- [93] C. Wang, I. Ulbert, D. L. Schomer, K. Marinkovic, and E. Halgren, "Responses of human anterior cingulate cortex microdomains to error detection, conflict monitoring, stimulus-response mapping, familiarity, and orienting," *J Neurosci*, vol. 25, pp. 604-13, Jan 19 2005.
- [94] J. C. Williams, R. L. Rennaker, and D. R. Kipke, "Long-term neural recording characteristics of wire microelectrode arrays implanted in cerebral cortex," *Brain Res Brain Res Protoc*, vol. 4, pp. 303-13, Dec 1999.
- [95] S. S. Stensaas and L. J. Stensaas, "The reaction of the cerebral cortex to chronically implanted plastic needles," *Acta Neuropathol*, vol. 35, pp. 187-203, 1976.
- [96] X. Liu, D. B. McCreery, R. R. Carter, L. A. Bullara, T. G. Yuen, and W. F. Agnew, "Stability of the interface between neural tissue and chronically

- implanted intracortical microelectrodes," *IEEE Trans Rehabil Eng*, vol. 7, pp. 315-26, Sep 1999.
- [97] T. G. Yuen and W. F. Agnew, "Histological evaluation of polyesterimide-insulated gold wires in brain," *Biomaterials*, vol. 16, pp. 951-6, Aug 1995.
- [98] E. M. Maynard, E. Fernandez, and R. A. Normann, "A technique to prevent dural adhesions to chronically implanted microelectrode arrays," *J Neurosci Methods*, vol. 97, pp. 93-101, Apr 15 2000.
- [99] A. Devor, E. M. Hillman, P. Tian, C. Waeber, I. C. Teng, L. Ruvinskaya, M. H. Shalinsky, H. Zhu, R. H. Haslinger, S. N. Narayanan, I. Ulbert, A. K. Dunn, E. H. Lo, B. R. Rosen, A. M. Dale, D. Kleinfeld, and D. A. Boas, "Stimulus-induced changes in blood flow and 2-deoxyglucose uptake dissociate in ipsilateral somatosensory cortex," *J Neurosci*, vol. 28, pp. 14347-57, Dec 31 2008.
- [100] A. Devor, P. Tian, N. Nishimura, I. C. Teng, E. M. Hillman, S. N. Narayanan, I. Ulbert, D. A. Boas, D. Kleinfeld, and A. M. Dale, "Suppressed neuronal activity and concurrent arteriolar vasoconstriction may explain negative blood oxygenation level-dependent signal," *J Neurosci*, vol. 27, pp. 4452-9, Apr 18 2007.
- [101] I. Cohen and R. Miles, "Contributions of intrinsic and synaptic activities to the generation of neuronal discharges in in vitro hippocampus," *J Physiol*, vol. 524 Pt 2, pp. 485-502, Apr 15 2000.
- [102] P. Rakic, "Neurogenesis in adult primates," *Prog Brain Res*, vol. 138, pp. 3-14, 2002.
- [103] E. Gould, "How widespread is adult neurogenesis in mammals?," *Nat Rev Neurosci*, vol. 8, pp. 481-8, Jun 2007.
- [104] W. J. Streit, S. A. Walter, and N. A. Pennell, "Reactive microgliosis," *Prog Neurobiol*, vol. 57, pp. 563-81, Apr 1999.
- [105] W. J. Streit, "The role of microglia in brain injury," *Neurotoxicology*, vol. 17, pp. 671-8, Fall-Winter 1996.
- [106] W. F. Agnew, T. G. Yuen, D. B. McCreery, and L. A. Bullara, "Histopathologic evaluation of prolonged intracortical electrical stimulation," *Exp Neurol*, vol. 92, pp. 162-85, Apr 1986.
- [107] D. B. McCreery, T. G. Yuen, W. F. Agnew, and L. A. Bullara, "A characterization of the effects on neuronal excitability due to prolonged microstimulation with chronically implanted microelectrodes," *IEEE Trans Biomed Eng*, vol. 44, pp. 931-9, Oct 1997.
- [108] R. L. Schultz and T. J. Willey, "The ultrastructure of the sheath around chronically implanted electrodes in brain," *J Neurocytol*, vol. 5, pp. 621-42, Dec 1976.
- [109] T. Roitbak and E. Sykova, "Diffusion barriers evoked in the rat cortex by reactive astrogliosis," *Glia*, vol. 28, pp. 40-8, Oct 1999.
- [110] R. Wadhwa, C. F. Lagenaur, and X. T. Cui, "Electrochemically controlled release of dexamethasone from conducting polymer polypyrrole coated electrode," *J Control Release*, vol. 110, pp. 531-41, Feb 21 2006.
- [111] G. J. Todaro and H. Green, "Quantitative studies of the growth of mouse embryo cells in culture and their development into established lines," *J Cell Biol*, vol. 17, pp. 299-313, May 1963.
- [112] M. Steriade, D. A. McCormick, and T. J. Sejnowski, "Thalamocortical oscillations in the sleeping and aroused brain," *Science*, vol. 262, pp. 679-85, 10/29 1993.

- [113] M. Steriade and I. Timofeev, "Neuronal plasticity in thalamocortical networks during sleep and waking oscillations," *Neuron*, vol. 37, pp. 563-76, 02/20 2003.
- [114] M. Steriade, I. Timofeev, and F. Grenier, "Natural waking and sleep states: a view from inside neocortical neurons," *J Neurophysiol*, vol. 85, pp. 1969-85, 2001.
- [115] M. A. Castro-Alamancos, "Role of thalamocortical sensory suppression during arousal: focusing sensory inputs in neocortex," *The Journal of neuroscience : the official journal of the Society for Neuroscience*, vol. 22, pp. 9651-5, 11/15 2002.
- [116] J. M. Edeline, G. Dutrieux, Y. Manunta, and E. Hennevin, "Diversity of receptive field changes in auditory cortex during natural sleep," *The European journal of neuroscience*, vol. 14, pp. 1865-80, 12/01 2001.
- [117] E. B. Issa and X. Wang, "Sensory responses during sleep in primate primary and secondary auditory cortex," *Journal of Neuroscience*, vol. 28, pp. 14467-80, 12/31 2008.
- [118] R. D. Hall and A. A. Borbely, "Acoustically evoked potentials in the rat during sleep and waking," *Exp Brain Res*, vol. 11, pp. 93-110, 1970.
- [119] A. Herz, "Cortical and Subcortical Auditory Evoked Potentials During Wakefulness and Sleep in the Cat," *Prog Brain Res*, vol. 18, pp. 63-9, 1965.
- [120] G. Karmos, M. Molnár, V. Csépe, I. Winkler, and Y. V. Grinchenko, "Evoked Cortical Field Potential and Unit Responses in the Wakefulness-Sleep Cycle in Cats," pp. 1-2, 07/17 1988.
- [121] D. C. Teas and N. Y. Kiang, "Evoked Responses from the Auditory Cortex," *Exp Neurol*, vol. 10, pp. 91-119, Aug 1964.
- [122] W. O. Wickelgren, "Effect of state of arousal on click-evoked responses in cats," *J Neurophysiol*, vol. 31, pp. 757-68, Sep 1968.
- [123] A. Hasenstaub, R. N. Sachdev, and D. A. McCormick, "State changes rapidly modulate cortical neuronal responsiveness," *J Neurosci*, vol. 27, pp. 9607-22, Sep 5 2007.
- [124] Volgushev, Chauvette, Mukovski, and Timofeev, "Precise long-range synchronization of activity and silence in neocortical neurons during slow-wave oscillations [corrected]," *The Journal of neuroscience : the official journal of the Society for Neuroscience*, vol. 26, pp. 5665-72, 05/24 2006.
- [125] L. R. Squire, J. R. Roberts, N. C. Spitzer, M. J. Zigmond, S. K. McConnell, and F. E. Bloom, "Fundamental Neuroscience (2nd edition)," *Academic Press*, 2003.
- [126] R. Velluti, "The auditory system in sleep (1st edition)," *Academic Press*, 2008.
- [127] A. A. Ghazanfar and M. A. Nicolelis, "Nonlinear processing of tactile information in the thalamocortical loop," *J Neurophysiol*, vol. 78, pp. 506-10, Jul 1997.
- [128] J. He, "Modulatory effects of regional cortical activation on the onset responses of the cat medial geniculate neurons," *J Neurophysiol*, vol. 77, pp. 896-908, Feb 1997.
- [129] P. C. Murphy, S. G. Duckett, and A. M. Sillito, "Feedback connections to the lateral geniculate nucleus and cortical response properties," *Science*, vol. 286, pp. 1552-4, Nov 19 1999.
- [130] A. E. Villa, E. M. Rouiller, G. M. Simm, P. Zurita, Y. de Ribaupierre, and F. de Ribaupierre, "Corticofugal modulation of the information processing in the auditory thalamus of the cat," *Exp Brain Res*, vol. 86, pp. 506-17, 1991.
- [131] J. A. Winer, D. T. Larue, and C. L. Huang, "Two systems of giant axon terminals in the cat medial geniculate body: convergence of cortical and GABAergic inputs," *J Comp Neurol*, vol. 413, pp. 181-97, Oct 18 1999.

- [132] Y. Zhang and N. Suga, "Corticofugal amplification of subcortical responses to single tone stimuli in the mustached bat," *J Neurophysiol*, vol. 78, pp. 3489-92, Dec 1997.
- [133] G. Ehret and R. Romand, "The central auditory system," *Oxford University Press*, 1997.
- [134] E. G. Jones, "The thalamus (2nd edition)," *Cambridge University Press*, 2007.
- [135] O. Creutzfeldt, F. C. Hellweg, and C. Schreiner, "Thalamocortical transformation of responses to complex auditory stimuli," *Exp Brain Res*, vol. 39, pp. 87-104, 1980.
- [136] L. M. Miller, M. A. Escabi, H. L. Read, and C. E. Schreiner, "Functional convergence of response properties in the auditory thalamocortical system," *Neuron*, vol. 32, pp. 151-60, 10/11 2001.
- [137] M. Steriade, I. Timofeev, F. Grenier, and N. Durmuller, "Role of thalamic and cortical neurons in augmenting responses and self-sustained activity: dual intracellular recordings in vivo," *J Neurosci*, vol. 18, pp. 6425-43, Aug 15 1998.
- [138] S. M. Sherman and R. W. Guillery, "Functional organization of thalamocortical relays," *J Neurophysiol*, vol. 76, pp. 1367-95, Sep 1996.
- [139] S. M. Sherman and R. W. Guillery, "On the actions that one nerve cell can have on another: distinguishing "drivers" from "modulators"," *Proc Natl Acad Sci U S A*, vol. 95, pp. 7121-6, Jun 9 1998.
- [140] E. M. Rouiller, C. Rodrigues-Dageff, G. Simm, Y. De Ribaupierre, A. Villa, and F. De Ribaupierre, "Functional organization of the medial division of the medial geniculate body of the cat: tonotopic organization, spatial distribution of response properties and cortical connections," *Hear Res*, vol. 39, pp. 127-42, May 1989.
- [141] C. C. Lee and J. A. Winer, "Connections of cat auditory cortex: III. Corticocortical system," *J Comp Neurol*, vol. 507, pp. 1920-43, Apr 20 2008.
- [142] C. C. Lee and J. A. Winer, "Connections of cat auditory cortex: I. Thalamocortical system," *J Comp Neurol*, vol. 507, pp. 1879-900, Apr 20 2008.
- [143] C. L. Huang and J. A. Winer, "Auditory thalamocortical projections in the cat: laminar and areal patterns of input," *The Journal of Comparative Neurology*, vol. 427, pp. 302-31, 11/13 2000.
- [144] J. Winer, L. M. Miller, C. Lee, and C. E. Schreiner, "Auditory thalamocortical transformation: structure and function," *Trends in neurosciences*, vol. 28, pp. 255-63, 05/01 2005.
- [145] T. L. Frigyesi, E. Rinvik, and D. Y. Melvin, "Corticothalamic projections and sensorimotor activities," *New York: Raven Press*, 1972.
- [146] J. A. Winer, J. J. Diehl, and D. T. Larue, "Projections of auditory cortex to the medial geniculate body of the cat," *J Comp Neurol*, vol. 430, pp. 27-55, Jan 29 2001.
- [147] J. A. Winer and D. T. Larue, "Patterns of reciprocity in auditory thalamocortical and corticothalamic connections: study with horseradish peroxidase and autoradiographic methods in the rat medial geniculate body," *J Comp Neurol*, vol. 257, pp. 282-315, Mar 8 1987.
- [148] A. W. Przybyszewski, "Vision: does top-down processing help us to see?," *Curr Biol*, vol. 8, pp. R135-9, Feb 12 1998.
- [149] K. M. Spangler and W. B. Warr, "The descending auditory system (In: Altshuler, R. A., Bobbin, R. P., Clopton, B. M.: Neurobiology of hearing. The central auditory system)," *Plenum Press, New York*, pp. 27-45, 1991.

- [150] J. A. Winer, D. T. Larue, J. J. Diehl, and B. J. Hefti, "Auditory cortical projections to the cat inferior colliculus," *J Comp Neurol*, vol. 400, pp. 147-74, Oct 19 1998.
- [151] B. R. Schofield and D. L. Coomes, "Auditory cortical projections to the cochlear nucleus in guinea pigs," *Hear Res*, vol. 199, pp. 89-102, Jan 2005.
- [152] W. H. Mulders and D. Robertson, "Evidence for direct cortical innervation of medial olivocochlear neurones in rats," *Hear Res*, vol. 144, pp. 65-72, Jun 2000.
- [153] G. Amato, V. La Grutta, and F. Enia, "The control exerted by the auditory cortex on the activity of the medial geniculate body and inferior colliculus," *Arch Sci Biol (Bologna)*, vol. 53, pp. 291-313, Oct-Dec 1969.
- [154] E. K. Sauerland, R. A. Velluti, and R. M. Harper, "Cortically induced changes of presynaptic excitability in higher-order auditory afferents," *Exp Neurol*, vol. 36, pp. 79-87, Jul 1972.
- [155] J. A. Winer, "The functional architecture of the medial geniculate body and the primary auditory cortex (In: Webster, D. B.: Springer Handbook of auditory research. The Mammalian Auditory Pathway: Neuroanatomy)," *Springer-Verlag*, pp. 222-409, 1992.
- [156] J. A. Winer and J. J. Prieto, "Layer V in cat primary auditory cortex (AI): cellular architecture and identification of projection neurons," *J Comp Neurol*, vol. 434, pp. 379-412, Jun 11 2001.
- [157] P. Lakatos, "Akusztikus eseményhez kötött potenciál és gamma aktivitás viselkedésfüggő változása macska hallókérgén," *Semmelweis University Neurosciences Doctoral School, Ph.D. dissertation*, 2003.
- [158] M. M. Merzenich, P. L. Knight, and G. L. Roth, "Cochleotopic organization of primary auditory cortex in the cat," *Brain Res*, vol. 63, pp. 343-6, Dec 7 1973.
- [159] M. M. Merzenich, P. L. Knight, and G. L. Roth, "Representation of cochlea within primary auditory cortex in the cat," *J Neurophysiol*, vol. 38, pp. 231-49, Mar 1975.
- [160] J. E. Rose and C. N. Woolsey, "The relations of thalamic connections, cellular structure and evocable electrical activity in the auditory region of the cat," *J Comp Neurol*, vol. 91, pp. 441-66, Dec 1949.
- [161] J. Winer and C. Lee, "The distributed auditory cortex," *Hearing Research*, vol. 229, pp. 3-13, 07/01 2007.
- [162] T. J. Imig and R. A. Reale, "Patterns of cortico-cortical connections related to tonotopic maps in cat auditory cortex," *J Comp Neurol*, vol. 192, pp. 293-332, Jul 15 1980.
- [163] M. Izumi and Y. Nakamura, "The organization of the ipsilateral corticocortical projections of the middle sylvian gyrus (AII) in the cat cerebral cortex: an anterograde and retrograde tracing study," *Brain Res Bull*, vol. 47, pp. 141-9, Sep 15 1998.
- [164] I. O. Volkov and A. V. Galazyuk, "Cochleo- and tonotopic organization of the second auditory cortical area in the cat," *Neuroscience*, vol. 82, pp. 499-509, Jan 1998.
- [165] P. Heil and D. R. Irvine, "Functional specialization in auditory cortex: responses to frequency-modulated stimuli in the cat's posterior auditory field," *J Neurophysiol*, vol. 79, pp. 3041-59, Jun 1998.
- [166] P. Heil and D. R. Irvine, "The posterior field P of cat auditory cortex: coding of envelope transients," *Cereb Cortex*, vol. 8, pp. 125-41, Mar 1998.
- [167] B. J. Everitt and T. W. Robbins, "Central cholinergic systems and cognition," *Annu Rev Psychol*, vol. 48, pp. 649-84, 1997.

- [168] M. Goard and Y. Dan, "Basal forebrain activation enhances cortical coding of natural scenes," *Nat Neurosci*, vol. 12, pp. 1444-9, Nov 2009.
- [169] B. E. Jones, "Activity, modulation and role of basal forebrain cholinergic neurons innervating the cerebral cortex," *Prog Brain Res*, vol. 145, pp. 157-69, 2004.
- [170] M. Feliciano and S. J. Potashner, "Evidence for a glutamatergic pathway from the guinea pig auditory cortex to the inferior colliculus," *J Neurochem*, vol. 65, pp. 1348-57, Sep 1995.
- [171] G. Karmos, "Intracortical Profiles of Evoked Potential Components Related to Behavioural Activation in Cats," *Cerebral Psychophysiology: Studies in Event-Related Potentials*, pp. 551-557, 1986.
- [172] G. Karmos, M. Molnár, V. Csépe, and I. Winkler, "Evoked potential components in the layers of the auditory cortex of the cat," *Acta neurobiologiae experimentalis*, vol. 46, pp. 227-36, 01/01 1986.
- [173] G. Karmos, "Motivation and the neural and neurohumoral factors in regulation of behaviour," *Akadémiai kiadó*, vol. X, 1982.
- [174] M. Molnár, G. Karmos, and V. Csépe, "Laminar analysis of intracortical auditory evoked potentials during the wakefulness-sleep cycle in the cat," *International journal of psychophysiology : official journal of the International Organization of Psychophysiology*, vol. 3, pp. 171-82, 01/01 1986.
- [175] E. R. Kandel, J. H. Schwartz, and T. M. Jessell, "Principles of Neural Science (4th edition)," *McGraw-Hill Medical*, 2000.
- [176] R. Bódizs, "Alvás, ébrenlét, bioritmusok," *Budapest: Medicina Könyvkiadó*, 2000.
- [177] P. Maquet, C. Degueldre, G. Delfiore, J. Aerts, J. M. Peters, A. Luxen, and G. Franck, "Functional neuroanatomy of human slow wave sleep," *J Neurosci*, vol. 17, pp. 2807-12, Apr 15 1997.
- [178] E. Grastyán and G. Karmos, "A study of a possible "dreaming" mechanism in the cat," *Acta Physiol Acad Sci Hung*, vol. 20, pp. 41-50, 1961.
- [179] M. Steriade, A. Nunez, and F. Amzica, "Intracellular analysis of relations between the slow (< 1 Hz) neocortical oscillation and other sleep rhythms of the electroencephalogram," *J Neurosci*, vol. 13, pp. 3266-83, Aug 1993.
- [180] A. Destexhe, D. Contreras, and M. Steriade, "Spatiotemporal analysis of local field potentials and unit discharges in cat cerebral cortex during natural wake and sleep states," *Journal of Neuroscience*, vol. 19, pp. 4595-608, 06/01 1999.
- [181] Mukovski, Chauvette, Timofeev, and Volgushev, "Detection of active and silent states in neocortical neurons from the field potential signal during slow-wave sleep," *Cerebral cortex (New York, NY : 1991)*, vol. 17, pp. 400-14, 02/01 2007.
- [182] I. Timofeev, F. Grenier, and M. Steriade, "Disfacilitation and active inhibition in the neocortex during the natural sleep-wake cycle: an intracellular study," *Proc Natl Acad Sci U S A*, vol. 98, pp. 1924-9, Feb 13 2001.
- [183] M. Steriade, "Sleep oscillations in corticothalamic neuronal networks and their development into self-sustained paroxysmal activity," *Rom J Neurol Psychiatry*, vol. 31, pp. 151-61, Jul-Dec 1993.
- [184] M. Steriade, "Modulation of information processing in thalamocortical systems: chairman's introductory remarks," *Prog Brain Res*, vol. 98, pp. 341-3, 1993.
- [185] M. Steriade, D. Contreras, R. Curro Dossi, and A. Nunez, "The slow (< 1 Hz) oscillation in reticular thalamic and thalamocortical neurons: scenario of sleep rhythm generation in interacting thalamic and neocortical networks," *J Neurosci*, vol. 13, pp. 3284-99, Aug 1993.

- [186] I. Timofeev, "Thalamocortical oscillations," *Scholarpedia* (online: http://www.scholarpedia.org/article/Thalamocortical_oscillations), 2006.
- [187] F. Amzica and M. Steriade, "Disconnection of intracortical synaptic linkages disrupts synchronization of a slow oscillation," *J Neurosci*, vol. 15, pp. 4658-77, Jun 1995.
- [188] I. Timofeev and M. Steriade, "Low-frequency rhythms in the thalamus of intact-cortex and decorticated cats," *J Neurophysiol*, vol. 76, pp. 4152-68, Dec 1996.
- [189] M. Steriade, "Synchronized activities of coupled oscillators in the cerebral cortex and thalamus at different levels of vigilance," *Cereb Cortex*, vol. 7, pp. 583-604, Sep 1997.
- [190] M. Steriade and F. Amzica, "Coalescence of sleep rhythms and their chronology in corticothalamic networks," *Sleep Res Online*, vol. 1, pp. 1-10, 1998.
- [191] M. Steriade and F. Amzica, "Slow sleep oscillation, rhythmic K-complexes, and their paroxysmal developments," *J Sleep Res*, vol. 7 Suppl 1, pp. 30-5, 1998.
- [192] D. Contreras and M. Steriade, "Cellular basis of EEG slow rhythms: a study of dynamic corticothalamic relationships," *J Neurosci*, vol. 15, pp. 604-22, Jan 1995.
- [193] P. Fatt and B. Katz, "Spontaneous sub-threshold activity at motor-nerve endings," *Journal of Physiology* pp. 109-128, 1952.
- [194] I. Timofeev, F. Grenier, M. Bazhenov, T. J. Sejnowski, and M. Steriade, "Origin of slow cortical oscillations in deafferented cortical slabs," *Cereb Cortex*, vol. 10, pp. 1185-99, Dec 2000.
- [195] A. Compte, M. V. Sanchez-Vives, D. A. McCormick, and X. J. Wang, "Cellular and network mechanisms of slow oscillatory activity (<1 Hz) and wave propagations in a cortical network model," *J Neurophysiol*, vol. 89, pp. 2707-25, May 2003.
- [196] M. V. Sanchez-Vives and D. A. McCormick, "Cellular and network mechanisms of rhythmic recurrent activity in neocortex," *Nat Neurosci*, vol. 3, pp. 1027-34, Oct 2000.
- [197] R. Csercsa, "A lassú alvási oszcillációk intrakortikális generátorainak elemzése krónikusan beépített multielektroddal epilepsziás páciensekben," *Pázmány Péter Catholic University Faculty of Information Technology, Diploma thesis*, 2007.
- [198] R. Csercsa, B. Dombóvári, D. Fabó, L. Wittner, L. Eröss, L. Entz, A. Sólyom, G. Résonyi, A. Szűcs, A. Kelemen, R. Jakus, V. Juhos, L. Grand, A. Magony, P. Halász, T. Freund, S. Csah, G. Karmos, E. Halgren, and I. Ulbert, "Laminar analysis of the slow wave activity in humans," *Submitted to Brain*.
- [199] M. Steriade and F. Amzica, "Intracortical and corticothalamic coherency of fast spontaneous oscillations," *Proc Natl Acad Sci U S A*, vol. 93, pp. 2533-8, Mar 19 1996.
- [200] Y. Isomura, A. Sirota, S. Ozen, S. Montgomery, K. Mizuseki, D. A. Henze, and G. Buzsáki, "Integration and segregation of activity in entorhinal-hippocampal subregions by neocortical slow oscillations," *Neuron*, vol. 52, pp. 871-82, Dec 7 2006.
- [201] A. Luczak, P. Bartho, S. L. Marguet, G. Buzsáki, and K. D. Harris, "Sequential structure of neocortical spontaneous activity in vivo," *Proc Natl Acad Sci U S A*, vol. 104, pp. 347-52, Jan 2 2007.
- [202] V. Crunelli and S. W. Hughes, "The slow (<1 Hz) rhythm of non-REM sleep: a dialogue between three cardinal oscillators," *Nat Neurosci*, vol. 13, pp. 9-17, Jan.

- [203] U. Mitzdorf, "Current source-density method and application in cat cerebral cortex: investigation of evoked potentials and EEG phenomena," *Physiol Rev*, vol. 65, pp. 37-100, Jan 1985.
- [204] M. Steriade, F. Amzica, and D. Contreras, "Synchronization of fast (30-40 Hz) spontaneous cortical rhythms during brain activation," *J Neurosci*, vol. 16, pp. 392-417, Jan 1996.
- [205] M. Steriade, D. Contreras, F. Amzica, and I. Timofeev, "Synchronization of fast (30-40 Hz) spontaneous oscillations in intrathalamic and thalamocortical networks," *J Neurosci*, vol. 16, pp. 2788-808, Apr 15 1996.
- [206] M. Bazhenov, I. Timofeev, M. Steriade, and T. J. Sejnowski, "Model of thalamocortical slow-wave sleep oscillations and transitions to activated States," *J Neurosci*, vol. 22, pp. 8691-704, Oct 1 2002.
- [207] R. Huber, M. F. Ghilardi, M. Massimini, and G. Tononi, "Local sleep and learning," *Nature*, vol. 430, pp. 78-81, Jul 1 2004.
- [208] L. Marshall, H. Helgadottir, M. Molle, and J. Born, "Boosting slow oscillations during sleep potentiates memory," *Nature*, vol. 444, pp. 610-3, Nov 30 2006.
- [209] V. V. Vyazovskiy, C. Cirelli, M. Pfister-Genskow, U. Faraguna, and G. Tononi, "Molecular and electrophysiological evidence for net synaptic potentiation in wake and depression in sleep," *Nat Neurosci*, vol. 11, pp. 200-8, Feb 2008.
- [210] J. Born, B. Rasch, and S. Gais, "Sleep to remember," *Neuroscientist*, vol. 12, pp. 410-24, Oct 2006.
- [211] S. Diekelmann, H. P. Landolt, O. Lahl, J. Born, and U. Wagner, "Sleep loss produces false memories," *PLoS One*, vol. 3, p. e3512, 2008.
- [212] D. R. Euston, M. Tatsuno, and B. L. McNaughton, "Fast-forward playback of recent memory sequences in prefrontal cortex during sleep," *Science*, vol. 318, pp. 1147-50, Nov 16 2007.
- [213] S. Gais, B. Lucas, and J. Born, "Sleep after learning aids memory recall," *Learn Mem*, vol. 13, pp. 259-62, May-Jun 2006.
- [214] P. Maquet, "The role of sleep in learning and memory," *Science*, vol. 294, pp. 1048-52, Nov 2 2001.
- [215] D. A. Nita, Y. Cisse, I. Timofeev, and M. Steriade, "Waking-sleep modulation of paroxysmal activities induced by partial cortical deafferentation," *Cereb Cortex*, vol. 17, pp. 272-83, Feb 2007.
- [216] S. Vanhatalo, J. M. Palva, M. D. Holmes, J. W. Miller, J. Voipio, and K. Kaila, "Infraslow oscillations modulate excitability and interictal epileptic activity in the human cortex during sleep," *Proc Natl Acad Sci U S A*, vol. 101, pp. 5053-7, Apr 6 2004.
- [217] I. Timofeev, D. Contreras, and M. Steriade, "Synaptic responsiveness of cortical and thalamic neurones during various phases of slow sleep oscillation in cat," *J Physiol*, vol. 494 (Pt 1), pp. 265-78, Jul 1 1996.
- [218] G. Karmos, J. Martin, L. Kellenyi, and M. Bauer, "Constant intensity sound stimulation with a bone conductor in the freely moving cat," *Electroencephalogr Clin Neurophysiol*, vol. 28, pp. 637-8, Jun 1970.
- [219] I. Ulbert, "Investigation of the evoked and spontaneous intracortical electrical activity with multielectrodes in humans " *Semmelweis University Neurosciences Doctoral School, Ph.D. dissertation*, 2002.
- [220] A. Delorme and S. Makeig, "EEGLAB: an open source toolbox for analysis of single-trial EEG dynamics including independent component analysis," *J Neurosci Methods*, vol. 134, pp. 9-21, Mar 15 2004.

- [221] L. Grand, "Idő és frekvencia elemzést végző szoftver fejlesztése a hallókéregben kiváltott potenciálok számítógépes vizsgálatára," *Pázmány Péter Catholic University Faculty of Information Technology, Diploma thesis*, 2006.
- [222] J. A. Freeman and C. Nicholson, "Experimental optimization of current source-density technique for anuran cerebellum," *J Neurophysiol*, vol. 38, pp. 369-82, Mar 1975.
- [223] C. Nicholson and J. A. Freeman, "Theory of current source-density analysis and determination of conductivity tensor for anuran cerebellum," *J Neurophysiol*, vol. 38, pp. 356-68, Mar 1975.
- [224] Z. Somogyvari, L. Zalanyi, I. Ulbert, and P. Erdi, "Model-based source localization of extracellular action potentials," *J Neurosci Methods*, vol. 147, pp. 126-37, Sep 30 2005.
- [225] A. B. Saleem, P. Chadderton, J. Apergis-Schoute, K. D. Harris, and S. R. Schultz, "Methods for predicting cortical UP and DOWN states from the phase of deep layer local field potentials," *J Comput Neurosci*, Mar 12 2010.
- [226] W. H. Kruskal, "A Nonparametric test for the Several Sample Problem," *Annals of Mathematical Statistics*, vol. 23, pp. 525-540, 1952.
- [227] W. H. Kruskal and W. A. Wallis, "Use of ranks in one-criterion variance analysis," *Journal of the American Statistical Association*, vol. 47, pp. 583-621, 1952.
- [228] A. M. Coenen, "Neuronal activities underlying the electroencephalogram and evoked potentials of sleeping and waking: implications for information processing," *Neurosci Biobehav Rev*, vol. 19, pp. 447-63, Fall 1995.
- [229] H. K. Meeren, A. M. van Cappellen van Walsum, E. L. van Luijckelaar, and A. M. Coenen, "Auditory evoked potentials from auditory cortex, medial geniculate nucleus, and inferior colliculus during sleep-wake states and spike-wave discharges in the WAG/Rij rat," *Brain Res*, vol. 898, pp. 321-31, Apr 20 2001.
- [230] M. Molnar, G. Karmos, V. Csepe, and I. Winkler, "Intracortical auditory evoked potentials during classical aversive conditioning in cats," *Biol Psychol*, vol. 26, pp. 339-50, Jun 1988.
- [231] R. A. Velluti, "Interactions between sleep and sensory physiology," *J Sleep Res*, vol. 6, pp. 61-77, Jun 1997.
- [232] M. Steriade, "Alertness, quiet sleep, dreaming (In: Peters, A.: Cerebral cortex)," *New York: Plenum*, pp. 279-357, 1991.
- [233] M. Steriade, "The corticothalamic system in sleep," *Frontiers in bioscience*, vol. 8, pp. d878-99, 05/01 2003.
- [234] B. E. Cairns, M. C. Fragoso, and P. J. Soja, "Activity of rostral trigeminal sensory neurons in the cat during wakefulness and sleep," *J Neurophysiol*, vol. 73, pp. 2486-98, Jun 1995.
- [235] B. E. Cairns, T. Kiang, S. A. McErlane, M. C. Fragoso, and P. J. Soja, "Eye movement-related modulation of trigeminal neuron activity during active sleep and wakefulness," *Brain Res*, vol. 975, pp. 110-9, Jun 13 2003.
- [236] P. J. Soja, W. Pang, N. Taepavarapruk, and S. A. McErlane, "Spontaneous spike activity of spinoreticular tract neurons during sleep and wakefulness," *Sleep*, vol. 24, pp. 18-25, Feb 1 2001.
- [237] B. E. Cairns, M. C. Fragoso, and P. J. Soja, "Active-sleep-related suppression of feline trigeminal sensory neurons: evidence implicating presynaptic inhibition via a process of primary afferent depolarization," *J Neurophysiol*, vol. 75, pp. 1152-62, Mar 1996.

- [238] B. E. Cairns, S. A. McErlane, M. C. Fragoso, W. G. Jia, and P. J. Soja, "Spontaneous discharge and peripherally evoked orofacial responses of trigemino-thalamic tract neurons during wakefulness and sleep," *J Neurosci*, vol. 16, pp. 8149-59, Dec 15 1996.
- [239] E. Hennevin, C. Huetz, and J. M. Edeline, "Neural representations during sleep: from sensory processing to memory traces," *Neurobiology of learning and memory*, vol. 87, pp. 416-40, 03/01 2007.
- [240] R. Galambos, O. Szabo-Salfay, E. Szatmari, N. Szilagyi, and G. Juhasz, "Sleep modifies retinal ganglion cell responses in the normal rat," *Proc Natl Acad Sci U S A*, vol. 98, pp. 2083-8, Feb 13 2001.
- [241] R. Velluti, M. Pedemonte, and E. Garcia-Austt, "Correlative changes of auditory nerve and microphonic potentials throughout sleep," *Hear Res*, vol. 39, pp. 203-8, May 1989.
- [242] M. Steriade, "Central core modulation of spontaneous oscillations and sensory transmission in thalamocortical systems," *Curr Opin Neurobiol*, vol. 3, pp. 619-25, Aug 1993.
- [243] M. Steriade, "Impact of network activities on neuronal properties in corticothalamic systems," *J Neurophysiol*, vol. 86, pp. 1-39, Jul 2001.
- [244] Livingstone and Hubel, "Effects of sleep and arousal on the processing of visual information in the cat," *Nature*, vol. 291, pp. 554-61, 06/18 1981.
- [245] L. M. Mukhametov and G. Rizzolatti, "The responses of lateral geniculate neurons to flashes of light during the sleep-waking cycle," *Arch Ital Biol*, vol. 108, pp. 348-68, Apr 1970.
- [246] M. Mariotti, A. Formenti, and M. Mancina, "Responses of VPL thalamic neurones to peripheral stimulation in wakefulness and sleep," *Neurosci Lett*, vol. 102, pp. 70-5, Jul 17 1989.
- [247] T. Satoh, K. Eguchi, K. Watabe, Y. Harada, and F. Hotta, "Attenuation during paradoxical sleep of signals from tooth pulp to thalamus," *Brain Res Bull*, vol. 5, pp. 547-51, Sep-Oct 1980.
- [248] J. M. Edeline, Y. Manunta, and E. Hennevin, "Auditory thalamus neurons during sleep: changes in frequency selectivity, threshold, and receptive field size," *J Neurophysiol*, vol. 84, pp. 934-52, Aug 2000.
- [249] A. M. Coenen and A. J. Vendrik, "Determination of the transfer ratio of cat's geniculate neurons through quasi-intracellular recordings and the relation with the level of alertness," *Exp Brain Res*, vol. 14, pp. 227-42, 1972.
- [250] O. Benoit and C. Chataignier, "Patterns of spontaneous unitary discharge in thalamic ventro-basal complex during wakefulness and sleep," *Exp Brain Res*, vol. 17, pp. 348-63, Jun 29 1973.
- [251] D. H. Hubel, "Single unit activity in lateral geniculate body and optic tract of unrestrained cats," *J Physiol*, vol. 150, pp. 91-104, Jan 1960.
- [252] R. W. McCarley, O. Benoit, and G. Barrionuevo, "Lateral geniculate nucleus unitary discharge in sleep and waking: state- and rate-specific aspects," *J Neurophysiol*, vol. 50, pp. 798-818, Oct 1983.
- [253] R. Krahe and F. Gabbiani, "Burst firing in sensory systems," *Nat Rev Neurosci*, vol. 5, pp. 13-23, Jan 2004.
- [254] R. R. Llinas and M. Steriade, "Bursting of thalamic neurons and states of vigilance," *J Neurophysiol*, vol. 95, pp. 3297-308, Jun 2006.
- [255] M. Steriade, "To burst, or rather, not to burst," *Nat Neurosci*, vol. 4, p. 671, Jul 2001.

- [256] A. Massaux, G. Dutrieux, N. Cotillon-Williams, Y. Manunta, and J. M. Edeline, "Auditory thalamus bursts in anesthetized and non-anesthetized states: contribution to functional properties," *J Neurophysiol*, vol. 91, pp. 2117-34, May 2004.
- [257] H. A. Swadlow and A. G. Gusev, "The impact of 'bursting' thalamic impulses at a neocortical synapse," *Nat Neurosci*, vol. 4, pp. 402-8, Apr 2001.
- [258] H. A. Swadlow and A. G. Gusev, "Receptive-field construction in cortical inhibitory interneurons," *Nat Neurosci*, vol. 5, pp. 403-4, May 2002.
- [259] M. Steriade and R. W. McCarley, "Brainstem control of wakefulness and sleep," *New York: Plenum Press*, 1990.
- [260] R. Desimone and J. Duncan, "Neural mechanisms of selective visual attention," *Annu Rev Neurosci*, vol. 18, pp. 193-222, 1995.
- [261] W. Plihal, S. Weaver, M. Molle, H. L. Fehm, and J. Born, "Sensory processing during early and late nocturnal sleep," *Electroencephalogr Clin Neurophysiol*, vol. 99, pp. 247-56, Sep 1996.
- [262] K. Murata and K. Kameda, "The Activity of Single Cortical Neurones of Unrestrained Cats During Sleep and Wakefulness," *Arch Ital Biol*, vol. 101, pp. 306-31, Jun 15 1963.
- [263] J. L. Pena, L. Perez-Perera, M. Bouvier, and R. A. Velluti, "Sleep and wakefulness modulation of the neuronal firing in the auditory cortex of the guinea pig," *Brain Res*, vol. 816, pp. 463-70, Jan 23 1999.
- [264] E. V. Evarts, "Photically evoked responses in visual cortex units during sleep and waking," *Journal of neurophysiology*, vol. 26, 1963.
- [265] R. W. Guillery and S. M. Sherman, "Thalamic relay functions and their role in corticocortical communication: generalizations from the visual system," *Neuron*, vol. 33, pp. 163-75, Jan 17 2002.
- [266] S. LeVay and C. D. Gilbert, "Laminar patterns of geniculocortical projection in the cat," *Brain Res*, vol. 113, pp. 1-19, Aug 20 1976.
- [267] E. L. White, "Identified neurons in mouse Sm1 cortex which are postsynaptic to thalamocortical axon terminals: a combined golgi-electron microscopic and degeneration study," *Journal of comparative neurology*, pp. 627-662, 1978.
- [268] M. Rosanova and I. Timofeev, "Neuronal mechanisms mediating the variability of somatosensory evoked potentials during sleep oscillations in cats," *The Journal of Physiology*, vol. 562, pp. 569-82, 01/15 2005.
- [269] M. Massimini, M. Rosanova, and M. Mariotti, "EEG slow (approximately 1 Hz) waves are associated with nonstationarity of thalamo-cortical sensory processing in the sleeping human," *J Neurophysiol*, vol. 89, pp. 1205-13, Mar 2003.
- [270] C. Huetz and J. M. Edeline, "From the receptive field dynamics to the rate of transmitted information: some facets of the thalamo-cortical auditory system," *Neuroembryology and Aging*, vol. 3, pp. 230-238, 2006.
- [271] J. D. Victor and K. P. Purpura, "Nature and precision of temporal coding in visual cortex: a metric-space analysis," *J Neurophysiol*, vol. 76, pp. 1310-26, Aug 1996.
- [272] D. H. Loewy, K. B. Campbell, and C. Bastien, "The mismatch negativity to frequency deviant stimuli during natural sleep," *Electroencephalogr Clin Neurophysiol*, vol. 98, pp. 493-501, Jun 1996.
- [273] T. Nashida, H. Yabe, Y. Sato, T. Hiruma, T. Sutoh, N. Shinozaki, and S. Kaneko, "Automatic auditory information processing in sleep," *Sleep*, vol. 23, pp. 821-8, Sep 15 2000.

- [274] L. Nielsen-Bohlman, R. T. Knight, D. L. Woods, and K. Woodward, "Differential auditory processing continues during sleep," *Electroencephalogr Clin Neurophysiol*, vol. 79, pp. 281-90, Oct 1991.
- [275] M. Atienza, J. L. Cantero, and C. M. Gomez, "The mismatch negativity component reveals the sensory memory during REM sleep in humans," *Neurosci Lett*, vol. 237, pp. 21-4, Nov 14 1997.
- [276] M. Czisch, R. Wehrle, C. Kaufmann, T. C. Wetter, F. Holsboer, T. Pollmacher, and D. P. Auer, "Functional MRI during sleep: BOLD signal decreases and their electrophysiological correlates," *Eur J Neurosci*, vol. 20, pp. 566-74, Jul 2004.
- [277] J. M. Halperin and L. C. Iorio, "Responsivity of rats to neutral and danger-signaling stimuli during sleep," *Behavioral and Neural Biology*, vol. 33, pp. 213-219, 1981.
- [278] V. Rowland, "Differential electroencephalographic response to conditioned auditory stimuli in arousal from sleep," *Electroencephalogr Clin Neurophysiol*, vol. 9, pp. 585-94, Nov 1957.
- [279] J. Siegel and T. D. Langley, "Arousal threshold in the cat as a function of sleep phase and stimulus significance," *Experientia*, vol. 21, pp. 740-1, Dec 15 1965.
- [280] M. A. Castro-Alamancos and E. Oldford, "Cortical sensory suppression during arousal is due to the activity-dependent depression of thalamocortical synapses," *J Physiol*, vol. 541, pp. 319-31, May 15 2002.
- [281] P. M. Headley, B. A. Chizh, J. F. Herrero, and N. A. Hartell, "Electrophysiology of spinal sensory processing in the absence and presence of surgery and anesthesia (In: Lydic, R; Baghdoyan, H. A.: Handbook of behavioral state control)," *Boca Raton: CRC Press*, pp. 505-520, 1999.
- [282] N. Cotillon-Williams and J. M. Edeline, "Evoked oscillations in the thalamocortical auditory system are present in anesthetized but not in unanesthetized rats," *Journal of neurophysiology*, pp. 1968-1984, 01/01 2003.
- [283] M. J. Guitton, P. Avan, J. L. Puel, and P. Bonfils, "Medial olivocochlear efferent activity in awake guinea pigs," *Neuroreport*, vol. 15, pp. 1379-82, Jun 28 2004.
- [284] K. Kishikawa, H. Uchida, Y. Yamamori, and J. G. Collins, "Low-threshold neuronal activity of spinal dorsal horn neurons increases during REM sleep in cats: comparison with effects of anesthesia," *J Neurophysiol*, vol. 74, pp. 763-9, Aug 1995.
- [285] L. C. Populin, "Anesthetics change the excitation/inhibition balance that governs sensory processing in the cat superior colliculus," *J Neurosci*, vol. 25, pp. 5903-14, Jun 22 2005.
- [286] P. Torterolo, A. Falconi, G. Morales-Cobas, and R. A. Velluti, "Inferior colliculus unitary activity in wakefulness, sleep and under barbiturates," *Brain Res*, vol. 935, pp. 9-15, May 10 2002.